

# Tides on unstructured meshes

Dissertation

presented by

Dipl. Math. Silvia Maßmann

in fulfillment of the requirements  
for the degree of  
doctor in natural sciences (Dr.rer.nat.)  
at the Department of Physics



1.Assessor: Prof. Dr. Dirk Olbers  
2.Assessor: Prof. Dr. Jörn Behrens

Submitted on November 30, 2009

Date of the colloquium: 10.02.2010

ALFRED WEGENER INSTITUTE FOR POLAR AND MARINE RESEARCH



## Abstract

Unstructured mesh methods offer flexibility in representing variable coastlines and bathymetries in ocean circulation models. They propose other advantages allowing, for example, to define high resolution in certain regions of global mesh without invoking nesting methods.

However, already existing finite-difference structured mesh models often outperform them as their computations per mesh node are less expensive. Nevertheless, due to the big variety of discretizations possible with unstructured mesh methods - finite element or finite volume - and the freedom in mesh design, the existing setups are not necessarily optimal in terms of accuracy and numerical efficiency. The search for optimal approach presents an important direction of current research.

This thesis partly contributes in this direction. Two finite element and one finite volume method are compared with respect to their ability to faithfully simulate tides on meshes of the European Continental Shelf. Judged by computational efficiency and the absence of stabilization the preference is given to the semi-implicit models based on finite volumes after Chen *et al.* (2003) or on the non-conforming finite element method.

One of the proposed models is further validated in simulating  $M_2$  and  $K_1$  tidal constituents on a fine mesh. Its performance in balancing energy and calculating residual currents is analyzed. The influence of the open boundary condition is also discussed.

The results obtained in this analysis indicate, that the model skills are more sensitive to errors in open boundary conditions and depth representation than to changes in the spatial or temporal discretization schemes. This dictates the next step — implementing algorithms that systematically improve model parameters and open boundary forcing. It is the second major goal of this thesis.

In the thesis the adjoint model is generated by adapting automatic differentiation technique. It computes the sensitivities of a cost function, which is a measure for the misfit between observed and simulated model fields, with respect to the depth, the bottom friction coefficients and the open boundary values.

The sensitivities are compared in  $M_2$  and  $K_1$  tidal simulations and on a coarse and fine meshes. Regions of strong sensitivities for each tidal constituent are identified. It turns out that the sensitivities on the coarse and fine meshes do not match. If mesh is coarse it is missing dynamics that are tuned. In contrast, on the fine mesh the sensitivities with respect to, for example, depth identify islands missing from the mesh. This suggests to use adjoint models for mesh refinements.

Further, the adjoint model is coupled to a Broyden-Fletcher-Goldfarb-Shanno algorithm, and the parameters are optimized on the coarse mesh. The error in coastline representation and mesh resolution is partly projected on the parameter sensitivities, which leads to a tendency in less realistic values unless strong regularization is used. This shows that tuning parameters for the wrong reason is something that should be avoided. This thesis proposes to use the sensitivities first for mesh refinements and in a second step for parameter optimization.



*Everything is vague to a degree you do not realise till you have tried to make it precise.*

Bertrand Russell (1872-1970).



# Contents

<b>Introduction</b>	<b>i</b>
<b>Notations</b>	<b>vii</b>
<b>1 State of the art</b>	<b>1</b>
1.1 Unstructured grid models . . . . .	1
1.2 North Sea: Hydrological and tidal regime . . . . .	5
1.2.1 Water transport and hydrodynamics . . . . .	6
1.2.2 Tides . . . . .	7
1.3 Tidal models for the North Sea . . . . .	9
1.4 Conclusion . . . . .	13
<b>2 Unstructured mesh tidal models</b>	<b>15</b>
2.1 Model description . . . . .	15
2.1.1 FE discretization . . . . .	16
2.1.2 FV discretization . . . . .	24
2.1.3 (Open) boundary conditions . . . . .	27
2.1.4 Tidal Potential . . . . .	30
2.1.5 Energy balance . . . . .	37
2.1.6 Conclusion . . . . .	42
2.2 Simulation results . . . . .	43
2.2.1 Model intercomparison for $M_2$ tidal wave . . . . .	43
2.2.2 $M_2$ tidal simulations on the European Continental Shelf	54
2.2.3 $K_1$ tidal simulations on the European Continental Shelf	66
2.2.4 Conclusion . . . . .	68
<b>3 Adjoint Models</b>	<b>71</b>
3.1 What is an adjoint? . . . . .	71
3.2 The adjoint equations . . . . .	72
3.3 Automatic differentiation . . . . .	74
3.4 Adjoint models in oceanography . . . . .	76
3.5 Conclusion . . . . .	78
<b>4 An unstructured mesh, adjoint, tidal model</b>	<b>81</b>
4.1 Motivation and setup . . . . .	81
4.2 Cost function . . . . .	83
4.3 Mesh description . . . . .	85

4.3.1	Coarse mesh setup . . . . .	85
4.3.2	Fine mesh setup . . . . .	85
4.3.3	Model performance on the meshes . . . . .	85
4.4	Sensitivity studies for $M_2$ . . . . .	87
4.4.1	Sensitivities on coarse mesh . . . . .	90
4.4.2	Sensitivities on fine mesh . . . . .	94
4.5	Sensitivity study for $K_1$ . . . . .	97
4.5.1	Sensitivity on coarse mesh . . . . .	97
4.5.2	Sensitivity on fine mesh . . . . .	98
4.6	Optimization . . . . .	103
4.6.1	Setup . . . . .	103
4.6.2	Results . . . . .	105
4.7	Conclusion . . . . .	112
 <b>Summary</b>		 <b>119</b>
 <b>Outlook</b>		 <b>123</b>
 <b>Appendix</b>		 <b>125</b>

# Introduction

The prediction of storm surges, such as the flooding triggered by hurricane Katrina, is just one example, where operational models including tides are important for coastal management.

Although ocean tides are well understood, their numerical modeling in coastal seas still presents challenges due to the diversity of involved processes (wetting & drying, river inflow, sea ice, wind, general ocean circulation) and the complexity of the coastlines and the topography. Generated by the non-linear frictional dissipation and advection of momentum compound tides and overtides significantly deform the dominant tidal waves (Parker, 1991). Hydrodynamic tidal models exist in global setups (e.g., Zahel, 1995; Lyard *et al.*, 2006) and for specific regions on the continental shelves, for example in the Irish Sea (Heaps & Jones, 1981) or for estuaries (Uncles & Stephens, 1989).

The contribution of baroclinic (internal) tides to the surface elevation is relatively small compared to the barotropic tides, therefore the prediction of tidal elevation is considerably well represented by barotropic shallow water models. However, there are numerous aspects of ocean dynamics where three dimensionality and baroclinicity are important players. One aspect is the prediction of sediment transport, where the bottom boundary layer has to be resolved and the vertical velocity field has to be described (Pandoe & Edge, 2003). Further examples come from modeling fresh-water ecosystems which may be influenced by saline water discharges propagating up the rivers.

On a more global scale, internal baroclinic tides are generated by quasi-barotropic tidal motion over steep topography (Kantha & Clayson, 2000). Their breaking is a source of cross-isopycnal mixing and the generation of deep sea internal waves. There are indications that baroclinic tides and winds contribute to the same order to the maintenance of the abyssal stratification, making them important components of the thermohaline circulation (Munk & Wunsch, 1998). However, tidal dissipation is strongest in coastal regions and a major contributor to mixing. The reconstruction and quantification of tidal dissipation is an important research subject of paleoscience. The identification of intensified regions over the past billion years remains unresolved due to lack of measurements.

Studying these aspects presents many challenges. Even within the barotro-

pic dynamics a faithful prediction of elevation, currents and residual circulation is far from being a simple problem given the intricacy of coastlines, bottom topography, and frictional forces.

The geometrical complexity of coastlines and the feasibility of variable resolution make tidal models formulated on unstructured grids more appealing than those based on regular grids. The unstructured grid modeling is an area of ongoing research, involving challenges such as accuracy and numerical efficiency. The long term goal of the unstructured grid ocean modeling community is to establish fast, high precision ocean models based on unstructured grids and coupled to atmospheric models in operational use. To achieve this goal many unsolved questions and problems need to be tackled.

Generally computer codes working on unstructured meshes are considerably slower per grid node than the ones designed for regular meshes. The numerical efficiency of unstructured mesh codes has seldom been addressed in literature, even though this becomes a decisive aspect when questions of realistic size are solved.

Some aspects of accuracy of particular discretizations were addressed recently using elementary test cases (Le Roux *et al.*, 2007, 2009). However, the precision of tidal simulations in real-world applications is a more delicate task, and involves, in addition to the purely numerical aspect, the knowledge of topography, parameterization of bottom friction, reliable description of wetting and drying and open boundary conditions. There are multiple sources of model error (Bennett & McIntosh, 1982, 1984). Increasing the order of the spatial or temporal discretization scheme or refining the mesh only reduces some part of the model error. Reaching realism in representing the tides requires tuning of the models with respect to bathymetry, bottom friction and open boundary values.

Coastal, barotropic tidal models are based on the 2D shallow water equations. Parameters such as the bottom friction coefficient substantially influence energy dissipation. Though it is known that the bottom friction parameter is not constant, measurements or reliable estimates are rare. Further, the bathymetric data is sometimes a combined product of different sources with different errors. Some features are smoothed, while they can be resolved with the unstructured mesh. Additionally the bottom topography may change in time due to sediment transport. It is therefore a fairly challenging task to determine from ocean elevation observations the underlying bathymetry.

Unstructured grids consist of nodes and edges defining, for example, triangles or rectangles of variable size. Usually the variables are attributed to the nodes. Since the number of unknown parameters is of the order of the number of nodes, and changing them one after another comparing the influence on the error, tuning of the parameters is time consuming. The

implementation of the adjoint model helps to facilitate the adjustment. For this purpose a cost function measures the misfit between observation and model result. An adjoint model gives the derivative of the cost function with respect to the parameters and therefore, knowledge about the error sensitivity to changes of the parameters. This can be used to adjust all parameters at once. Hand-coded or manually differentiated (MD) adjoint tidal models are used for the adjustment of open boundary conditions, bottom friction or depth for example by Bennett & McIntosh (1982), Verlaan *et al.* (1996) or Heemink *et al.* (2002). The main disadvantage of MD codes is that changes in the forward code have to be translated into the reverse code. Automatic differentiation (AD) is a tool to generate discrete adjoint models with less effort. Additionally once the forward model has been prepared for it, the adjoint generation is easily repeated if changes in the forward code are made. Although AD tools are available for many years, they have been rarely used for adjoint coastal ocean models. Recent studies (e.g. Elizondo *et al.*, 2002) suggest that AD adjoint models are more accurate than MD adjoint models. But differences in computational performance and accuracy compared with their MD counterparts have not been evaluated for tidal unstructured ocean models yet.

This thesis contributes to the development of tidal models on unstructured meshes in two important directions. The first goal is to explore accuracy and numerical efficiency of the forward code, and the second goal is to facilitate the tuning of models.

For the first goal I identify optimal discretization techniques with respect to realism in representing tides and with good numerical efficiency. The intercomparison between finite element and finite volume methods applied to solve the shallow water equations on realistic unstructured meshes gives preference to particular algorithms.

During this thesis several codes are developed. In particular the semi-implicit and the Adams-Bashforth non-conforming finite element branch are implemented, the configurations are made for tidal simulations, test meshes are generated and the codes are tested. Furthermore, I configure several models with different discretization for particular areas of application, analyze and compare the results. Various types of open boundary conditions are tested, too.

Two finite element (FE) and one finite volume (FV) technique are tested in an intercomparison study on a North Sea unstructured grid with GEBCO bathymetry. The major motivation for choosing the North Sea is the availability of tidal gauge data on multiple stations which allows testing the models against observations. Tidal maps of the major tidal modes (Defant, 1961) as well as charts and measurements of the tidal streams (see, e.g., Sager &

Sammler, 1968; Dick *et al.*, 1992) show that the North Sea is sufficiently well known to validate new tidal models. Operational models coupled with current meteorological data (like the BSHcmod, Dick *et al.*, 2001) have been tuned to fit observation for years predicting storm surge heights and the magnitude and direction of tidal streams.

The second goal is to provide methods that systematically help optimize the parameters. An adjoint model is implemented and used for sensitivity studies with respect to open boundary conditions, bathymetry and the bottom friction coefficient. In order to have flexibility in changing the forward code and to facilitate obtaining adjoints of the non-linear terms and time-dependent variables, an automatic differentiation procedure is applied to construct the adjoint model. Here I adapt the model structure to the requirements of the AD program and find an appropriate cost function including regularizations for the subsequent minimization. In this thesis the sensitivity patterns are analyzed and the configurations for the optimization routines are set. The optimization shows effective reduction of the misfit between model results and observations.

Chapter 1 summarizes common unstructured mesh approaches. The state of the art of unstructured mesh models with special focus on tidal applications in the North Sea is presented. It also deals with the particular features of the North Sea tidal dynamics and points out some open questions and current research objectives.

Chapter 2 presents the finite element (FE) and finite volume (FV) models developed for this study. New aspects for the implementation of a stable advection scheme of the non-conforming FE models are given. Furthermore, it revisits the treatment of open boundary conditions. In order to compare FE and FV models in terms of accuracy and computational cost, three different spatial discretizations are implemented. They consist of one FV setup and two FEs discretizations and use four different temporal discretizations, namely leapfrog, Adam-Bashforth, Runge-Kutta and Euler semi-implicit. Not all combinations are implemented. FV exists in three time stepping methods, the non-conforming FE method has also three methods, and the continuous FE method uses only the semi-implicit method. The performance of the seven models to simulate the  $M_2$  tide in the North Sea is tested and compared against satellite and tide gauge tidal observations. Recommendations about what kind of models are fast and accurate are drawn from this intercomparison.

Suggested by the intercomparison, one model is tested on a high resolution North and Baltic Sea grid in simulating the major tidal constituents. It is validated by comparing the tidal energy transformations and the residual currents and demonstrates the power of unstructured grid modeling.

Chapter 3 explains the concepts of adjoint models and automatic differentiation, pointing out different ways an adjoint model can be implemented. During this thesis the appropriate automatic differentiation tool is found and the code is prepared for its differentiation. Furthermore, the code is tested and applied to realistic settings with moderate size.

Chapter 4 shows how the cost function is influenced by changes in depth, bottom friction parameters and open boundary values. These sensitivities are compared on a coarse and fine mesh and with the  $M_2$  or the  $K_1$  tide. In order to improve results in one area I identify regions, that influence the result more than others.

The author provides interfaces to use the differentiated code together with optimization routines. The adjoint model and an BFGS algorithm minimize the misfit between model results and observations and generates optimized bottom friction coefficients, depths and open boundary values.

Finally, conclusions are drawn and an outlook for future research is given.



# Notations

$S$  is the unit sphere

$\partial S$  is the surface of the unit sphere

$\Omega$  is a domain on the Earth

$\Omega_e$  is a triangular part of  $\Omega$

$\partial\Omega_e$  is the boundary of  $\Omega_e$

$\Gamma_1$  be the coastal boundary of  $\Omega$

$\Gamma_2$  of the open (wet) boundary of  $\Omega$

$\partial\Omega$  is total boundary of  $\Omega$ , e.g.  $\partial\Omega = \Gamma_1 \cup \Gamma_2$

$g$  is the gravitational acceleration

$f$  is the Coriolis parameter

$r$  the bottom friction coefficient

$\rho$  is the mean density of sea water

$\rho_e$  is the mean density of the solid Earth

$P_1$  linear “hat” functions, defined on nodes

$P_1^{NC}$  linear functions defined on edges

2D = two dimensional

3D = three dimensional

AD = automatic differentiation

FD = Finite Difference

FV = Finite Volume

FE = Finite Element

WCE = wave continuity equation

rhs = right hand side

rms = root mean square

GW = Giga Watt

AB = Adams-Bashforth

AM = Adams-Moulthon

RK = Runge-Kutta

Sv = Sverdrup ( $=10^6 m^3/s$ )

psu = practical salinity units

BFGS = Broyden-Fletcher-Goldfarb-Shanno (a Quasi-Newton method)



# 1 State of the art

In this chapter I give a brief review of existing literature on unstructured grid modeling for 2D shallow water flow, summarize the general features of tides in the North Sea and list some widely used models. Section 1.1 highlights some stages in the development and history of unstructured grid modeling techniques for the shallow water equations. Since literature about this topic is enormous, only a limited view with chosen references can be given. Section 1.2 is about the tides in the North Sea and summarizes, what is known about their origin and appearance. Although this region has been investigated for centuries some open questions still remain. Afterwards, Section 1.3 gives an overview of the already existing structured and unstructured tidal models for the North Sea region. Since this area is well-studied, the list will always be incomplete.

## 1.1 Unstructured grid models

Unstructured grid models suggest a number of advantages compared to structured finite difference (FD) models. One example is the representation of the complex shoreline and controlling the mesh density according to the varying topography. The mesh information is stored by the geographical coordinates of the nodes and a list containing the node numbers of each element. Elements can be any polygon, but I choose triangles as they are commonly used. Over the last several decades many models working on unstructured grids have been proposed for the 2D shallow water equations.

For the spatial computation, amongst others, finite element (FE), finite volume (FV) and spectral methods are very famous. FV methods build upon the discrete points certain volumes and assign them to the variables. Spectral methods transform the variables into spectral space and solve them there. FE methods use polynomial functions defined by values placed somewhere on the grid. Usually these functions are defined by values of the nodes, but one can also use mid edge values for example. The higher order polynomials may add additional points on the grid or span over some elements (where elements refer to the grid cells). The sum of all functions suppose to approximate the continuous solution. I will later demonstrate that the stability is affected by the choice of these functions. These functions have to be appropriate for the equations and the desired order of approximation.

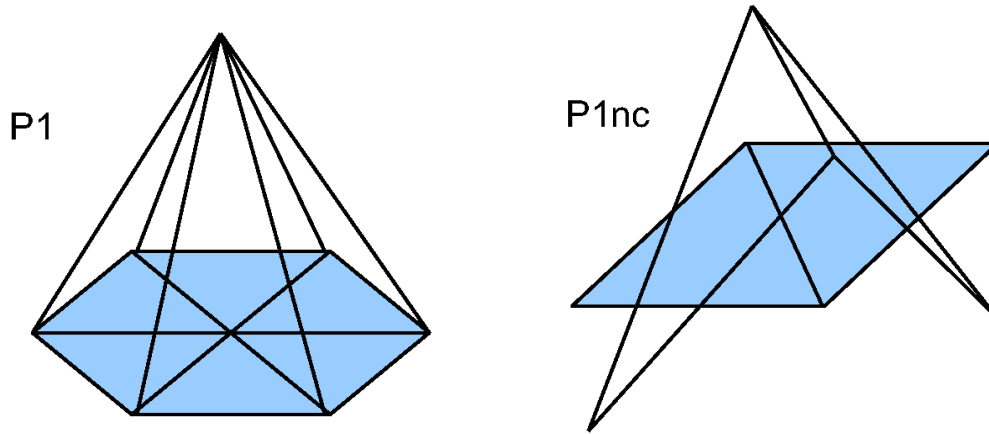


Figure 1.1: Finite element test functions: left  $P_1$ , right  $P_1^{NC}$ . The blue triangles represent the mesh triangles.

FE methods divide into continuous and discontinuous. For continuous methods the nodal values are common on each neighboring element, while for discontinuous the values of the nodes are independent on each element. A third kind of discretization, the non conforming elements, are in-between. Their value is continuous on the mid edges, but discontinuous everywhere else.

The linear, continuous - so called  $P_1$  - and the linear, non-conforming - so called  $P_1^{NC}$  - functions on triangular grids are often used.  $P_1$  functions are one on the node with linear decrease to zero on the neighboring nodes.  $P_1^{NC}$  equal one on the edge and decrease linearly to minus one on the opposing nodes. They are shown in Fig. 1.1.

Although high-order FE promise higher accuracy they tend to be considerably more expensive numerically. For this reason current practice in ocean modeling is to use low-order computationally less expensive elements. But certain low order schemes also exhibit numerical difficulties, which will be explained in the following.

When for example  $P_1$  functions are used for velocity and elevation, spurious modes can be excited from the non empty nullspace of the discrete pressure gradient operator (see, e.g., Walters & Carey, 1983). A well-known solution procedure is to express velocity from the discrete equations and to substitute it in the continuity equation. As a result the nullspace of the gradient operator may be excited if the system becomes quasi stationary (the nullspace is not necessarily excited, when the temporal change is non zero). The discrete divergence operator can have a nullspace, too, and allow for spurious velocity modes. But these modes are less dangerous since the viscous term damps them sufficiently in general. Le Roux *et al.* (1998) analyse FE methods in their performance to solve the linear shallow water equations. Important is the ratio between degrees of freedom of velocity and

elevation. If they are different, then nullspaces exist. The mathematically strict criterion for the absence of pressure modes is the LBB condition (Ladyzhenskaya, 1969; Babuska, 1971; Brezzi, 1974), which is an error bound and, for instance, infinity if pressure modes are possible. Le Roux (2005) identified the  $P_1^{NC} - P_1$  finite element pair - e.g.  $P_1$  functions for elevation and  $P_1^{NC}$  functions for the velocities in x and y direction - to properly model the dispersion of the inertia-gravity wave. This pair does not support pressure modes. Other pairs like the  $P_1 - P_1$  elements - e.g.  $P_1$  functions for elevation and also for the velocities in x and y direction - suffer from pressure modes and need stabilization.

Increasing the viscosity is one way to reduce the computational velocity modes. The common approach for pressure modes is to replace the continuity equation by a wave continuity equation (WCE) before applying the discretization. One of the first WCE was proposed by Lynch & Gray (1979) and mixes continuity and momentum equation. It has the following form (for simplicity without advection and viscosity; see Appendix for its derivation):

$$\frac{\partial^2 \eta}{\partial t^2} + \tau \frac{\partial \eta}{\partial t} - \nabla \cdot \left( H f \mathbf{k} \times \mathbf{u} + H g \nabla \eta - \mathbf{u} \frac{\partial \eta}{\partial t} \right) - H \mathbf{u} \cdot \nabla \tau = 0. \quad (1.1)$$

$\tau$  denotes the linearized bottom friction coefficient,  $\eta$  the sea surface elevation,  $H = \eta + H_0$  the total fluid depth,  $\mathbf{u}$  the velocity vector in south-north and west-east direction,  $g$  the gravitational acceleration,  $f$  the Coriolis parameter and  $\mathbf{k}$  is the upward unit vector.

Kinnmark & Gray (1985) report that the WCE is able to propagate the node-to-node oscillations away. Kinnmark (1986) gives a clear preference for WCE instead of the primitive continuity equation.

A similar WCE is the so called generalized wave continuity equation (GWCE). Models such as QUODDY (Lynch *et al.*, 1996), ADCIRC (Westerink *et al.*, 1992) and MOG2D (Carrère & Lyard, 2003) successfully exploit the GWCE with a long record of applications ranging from local wind surge to global tide predictions. The equation is derived in the appendix. In general, it is obtained by using  $\partial \chi / \partial t + \tau_0^{-1} \chi = 0$  (here  $\tau_0$  is some arbitrary parameter) and replacing  $\chi$  with the left hand side of the continuity equation. Then the momentum equation is used to eliminate the time derivative of the velocity. Without viscosity and advection the following form is obtained

$$\frac{\partial^2 \eta}{\partial t^2} + \tau_0^{-1} \left( \frac{\partial \eta}{\partial t} + \nabla \cdot (\eta + H_0) \mathbf{u} \right) - \nabla \cdot \left( H f \mathbf{k} \times \mathbf{u} + H g \nabla \eta + H \tau \mathbf{u} - \mathbf{u} \frac{\partial \eta}{\partial t} \right) = 0$$

The trick of the WCE is that it contains a diffusion-type operator applied to the elevation. Its discretization has different properties and filters out the pressure modes. Therefore, the WCE gives better stability.

The price of the WCE is that the exact local mass conservation is lost (see, e.g., Massey & Blain, 2006). As it can see in Eqn.(1.1), the continuity con-

straint is weakend and needs not to be satisfied exactly any more. Therefore, the GWCE uses the additional term  $\tau_0^{-1}\chi$  to better preserve local mass conservation (Dupont, 2001).

Next to the GWCE or WCE a natural way to prohibit pressure modes is to increase the degrees of freedom for velocity. Since  $P_1^{NC}$  is defined on edges, whose number is approximately three times the number of nodes, the  $P_1^{NC} - P_1$  element pair (Hua & Thomasset, 1984) has this desired property. Recently Hanert *et al.* (2004) and Hanert *et al.* (2005) proposed new promising methods for the treatment of advection and diffusion for  $P_1^{NC} - P_1$ . The difficulty is to compute correct fluxes at the element boundaries. I will discuss this topic in more details in Section 2.1.1.

Another advantage of  $P_1^{NC} - P_1$  is that the velocity mass matrix (e.g. the matrix  $\int_{\Omega} \Psi_i \Psi_j d\omega$ , where  $\Psi_i$  is the non-conforming test function on edge  $i$  and  $\int_{\Omega} d\omega$  is the integral over the domain) is diagonal and, therefore, easy to invert without lumping, e.g. diagonalizing the matrix by summing up the off diagonal entries and adding it to the diagonal. On irregular meshes mass matrix lumping has some implication on accuracy and should therefore be treated with caution (see Hughes, 2000; Walters *et al.*, 2009) for a brief review and an intercomparison study).

Next to the FE methods introduced above, FV methods are used to solve equations on unstructured meshes. FV methods assign certain volumes to the variables. One widely used approach utilizes a mixture of FV and FD methods and can be interpreted as a triangular analogue of C-grid discretization on quadrilateral grids (Casulli & Walters, 2000). The elevation is constant on each element and the normal velocity is given on the edges, which makes the computation of the Coriolis force more difficult. The Coriolis term shall be treated such that skew symmetry is maintained (Perot, 2000; Ham *et al.*, 2007; Kleptsova *et al.*, 2009). The method is able to use a mixture of triangles and quadrilaterals, but the mesh has to be orthogonal. In this context a mesh is orthogonal, if every element has a point called "center", such that the element edge is orthogonal to the segment joining the center and the neighboring center. "Centers" are for example the circumcenters, and the mesh has to be constructed in such a way, that the circumcenters lie within the elements. Designing such an orthogonal mesh is less straightforward and, therefore, another recent FV method became very popular. It is employed by FVCOM (Chen *et al.*, 2003) and assigns the velocity to the barycenters by using the element volume. The elevation is given on the nodes with a volume constructed by edge mid points and barycenters. I will employ this approach, as it can use the same triangular meshes as the FE methods presented above. More details about this method are given in Section 2.1.2.

An FE analogue to C-grid method, utilizing  $RT_0$  element, is gaining in popularity, too (Walters & Casulli, 1998; Hanert *et al.*, 2009). The elevation is discretized by constant functions on each element. The velocity is spanned by vector basis functions with expansion coefficient being normal component of velocity at edges. The functions are

$$\vec{\Psi}_i = \frac{\vec{x} - \vec{x}_i}{h_i},$$

where  $\vec{x}_i$  is the radius vector of the node opposite to edge  $i$  and  $h_i$  is the distance from the node to the edge. Like  $P_1^{NC} - P_1$  they are free of spurious elevation modes and its spurious velocity modes are naturally filtered out by viscosity (Hanert *et al.*, 2003). Furthermore, even with mass matrix lumping, the dispersive properties are well preserved (Le Roux *et al.*, 2009). Hanert *et al.* (2009) suggest that  $RT_0$  might be better suited than  $P_1^{NC} - P_1$  in the case of hydrological simulations with tracers, but in the case of purely hydrodynamical models  $P_1^{NC} - P_1$  should perform better than  $RT_0$ . Since the tides are mainly hydrodynamical, I will later solely use  $P_1^{NC} - P_1$  in the intercomparison study.

Many other approaches have been discussed in literature and used to formulate models. In particular, on the side of FE method, there is growing interest in discontinuous Galerkin (DG) methods. They provide higher numerical accuracy but also impose a larger computational burden as the number of degrees of freedom per element also increases. For example, there is currently an extension of ADCIRC (ADvanced CIRCulation Model for Shelves, Coasts, and Estuaries) to DG in development (Kubatko *et al.*, 2006, 2007). For further readings see e.g. Bernard (2008), who investigated the possibilities of DG methods in the SLIM (Second-generation Louvain-la-Neuve Ice-ocean Model) project, or Cotter *et al.* (2009), who proposes a mixed discontinuous/continuous FE method for the ICOM (Imperial College Ocean Model). It would be interesting to compare those new methods in tidal applications with the already existing methods in future studies.

## 1.2 North Sea: Hydrological and tidal regime

This section gives some information about the geographical domain which I will use to test the unstructured mesh models. The North Sea (shown in Fig.1.2) has been chosen, as it is a region of well-observed tidal dynamics and therefore able to validate model performance. In terms of later usability of the model this region is of interest with respect to the prediction of climate change and its consequences.

## 1.2.1 Water transport and hydrodynamics

The North Sea is a shelf sea covering an area of about 575,000 km<sup>2</sup>. Its water mass of approximately 54,000 km<sup>3</sup> exchanges mainly with the North Atlantic and, to a very limited extent, with the Baltic Sea.

Due to the small water depths (in average about 94 m) the circulation in the North Sea is strongly influenced by atmospheric forcing on synoptic scales and susceptible to long period climate variability. Temperature and salinity vary on seasonal, inter-annual and decadal time scales correlated to the NAO-Index. During winter the North Sea is vertically well mixed, except for some regions such as the Norwegian trench, where a haline stratification exist all year. The water gets less haline near estuaries and the outflow region of the Baltic Sea. Evaporation and precipitation result in a net fresh water input. A complete fresh water budget can be found in Damm (1997). The increased atmospheric heating during summer results in thermal stratification in the central and northern North Sea. Thermocline separate bottom and surface water, leading to oxygen reduction in the bottom water. Strong tidal currents in shallow water regions (depth less than 25 m) bring turbulent mixing and prohibit oxygen shortage (Müller, 2008).

A cyclonic circulation is driven amongst others by the North Atlantic current, the density distribution and winds. It transports water into the domain through the Fair Isle passage and a region east of the Shetland Islands, while water leaves the domain in the north eastern part of the North Sea. These transports vary seasonally around 0.4 Sv in the in- and outflow part and almost level each other during most of the time (Loewe, 2009). The mean flushing time of the North Sea water is approximately 167 days (Lenhart & Pohlmann, 1997).

Another arm of the North Atlantic current enters through the Strait of Dover with a yearly net mean transport of approximately 0.04 Sv (model estimate from BSHcmod). Measurements show significantly higher transport rates than suggested in most of the models (Pohlmann, 2003). Therefore, there is a need for further studies to explain the differences. The transport through Strait of Dover is also highly dependend on the wind stress. It reaches up to 1 Sv of in- or outflow during storm conditions. The Baltic Sea outflow into the North Sea mainly takes place in winter with about 0.013 Sv. During certain events North Sea water masses massively enter the Baltic Sea and supply the deeper layers with oxygen. Otherwise the Baltic Sea could shift to anaerobe conditions. Steep density gradients occur between the North and the Baltic Sea. In the Kattegat water from the Skagerrak with about 33 psu mixes with water from the Baltic sea with about 8 psu (Blanz *et al.*, 2005). This mixing is temporally variable. The water exchange between the two seas takes place during special events occurring irregularly (Meier *et al.*, 2006). A review of the interactions between the North and Baltic Sea can be found in Gustafsson (1997).

The flow dynamics of the North Sea are characterized by a transition/ interaction zone of geostrophic and ageostrophic components. Friction and topographic features lead to strong ageostrophic contributions, while some patterns still represent the unchanged oceanic circulation. It should be noted that the geostrophic contribution is relatively unimportant. Estimates of the baroclinic geostrophic currents (Pohlmann, 2003) suggest an anticyclonic contribution of the order of only 10% to the total circulation. Also the tidal residual current only plays a negligible role for the general, total circulation compared to contribution of wind and density currents (according to Pohlmann (2003)). Locally, for example around islands, there can be strong tidal residual currents and wind induces up- and downwelling.

Changes in the heat content are influenced by wind and thermal forcing. Strong winds during summer result in deepening of the thermocline and an enhanced heat storage. In the mid eighties the heat balance of the North Sea changed to a system with significantly higher overall heat content and stronger inter-annual variations (Pohlmann, 1996). This affected the composition of the ecosystem. The long term effects of the climate change in the North Sea are currently under investigation in many projects.

### 1.2.2 Tides

Tidal waves enter the North Sea between Scotland and Norway, as well as through the Strait of Dover. The elevation due to the tidal potential contributes only negligibly to the tidal waves. This is due to the relatively small water depth and the fact that the spatial scale of the basin is small compared to the spatial scale of the potential force.

The southwards propagating wave travels as Kelvin wave along the east coast of the United Kingdom and then turns anticlockwise along the Dutch, German and Danish coast. On its way it loses much of its energy and only a small portion enters the Baltic sea or leaves the region along the Norwegian coast. The bottom topography and the basin shape enforce the generation of Poincare waves and the appearance of amphidromic points. The three amphidromic points lie between England and the Netherlands, in the German bight and near the Norwegian coast (see Fig. 1.3). The obtained structure results from the interference of co-oscillating and external tides and, in some place, also the occurrence of free oscillations plays a role (Defant, 1961).

Flather (1976) computed the tidal energy fluxes through the open boundaries and its dissipation by bottom friction for the  $M_2$  tidal wave over the European Continental Shelf. Although the dissipation is underestimated and the bottom friction coefficient constant, the distribution among the basins seems to be reasonable. He estimated that the major part of the tidal energy enters the shelf between Ireland and the Bretagne. Here, only about 20% enters the North Sea through the Strait of Dover and the rest is dissipated



Figure 1.2: Geographical names used in the thesis

already on the shelf, in the Irish Sea or in the English Channel. Although the northern opening of the North Sea is bigger than the Strait of Dover and its incoming wave is the dominant forcing for the tides in the North Sea, the net energy input is smaller than through the Strait of Dover according to Flather (1976).

The European Continental Shelf contributes to the total tidal dissipation for all shallow seas with about 10% (Flather, 1976) and is therefore quite important for the energy budget of the global ocean.

By harmonic analysis the tidal signal can be decomposed into several constituents. The major diurnal constituents are  $K_1$  and  $O_1$  and the most important semi-diurnal ones are  $M_2$  and  $S_2$ , with the semi-diurnal signal dominating. The European shelf has very strong shallow water constituents, which are due to the non-linearities of e.g. bottom friction and advection. The highest amplitudes of the shallow water constituents have the over-tides  $M_4$  and  $M_6$  and the compound tides  $MNS_2$ ,  $MN_4$  and  $MS_4$  according to Andersen (1999). The amplitudes of  $M_4$  is in some places larger than the ones of the diurnal constituents. Double high and low waters are generated by  $M_4$  along the Dutch and British coast in the English Channel. Double high water means that high water persists several hours longer leading to strong currents during a few hours of ebb stream. For example Andersen (1999) present charts of  $M_4$  obtained from model calculations and TOPEX/POSEIDON estimates.

Cotidal maps show the spatial structure of amplitude and phase of the level oscillations of a single harmonic. The most important constituent in the North Sea is  $M_2$ . The cotidal maps give information about the propagation of the tidal wave with a corresponding period. The tidal chart of  $M_2$ -wave presented in Fig. 1.3 was obtained with the NCLF model, while the other models presented in Section 2.1 give approximately the same result. It is consistent with cotidal charts found in Sinha & Pingree (1997) and Howarth & Pugh (1983).

More recent sources of harmonic constituents in the North Sea are often combined model and altimeter products, for example FES04 (Lyard *et al.*, 2006), EOT08 (Savcenko & Bosch, 2008) or OTIS (Egbert & Erofeeva, 2002). They give estimates with a high accuracy in the open ocean. But for coastal tidal elevations the shape of the coastline and wetting and drying processes become important and regional models or tide gauge data sets are useful.

### 1.3 Tidal models for the North Sea

Before numerical tidal models for the North Sea were developed the description of tides had two major drawbacks. First, observations of tidal height were mostly confined to the coast, and second, the coverage of tidal current

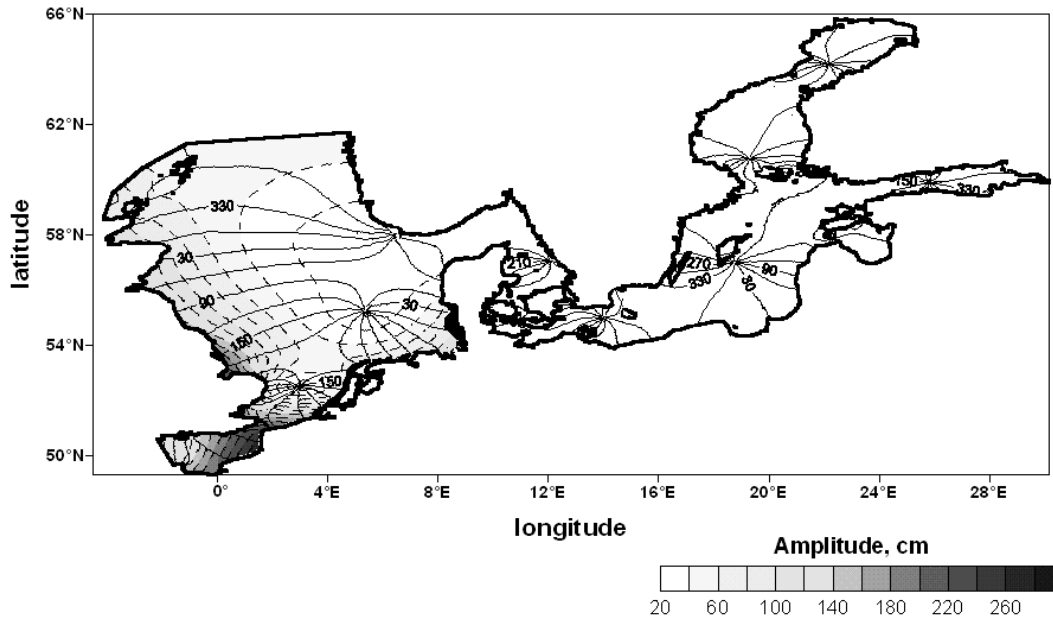


Figure 1.3:  $M_2$  Tidal chart: amplitude in cm, phase in degree (obtained with model NCLF on a mesh covering the North and Baltic Sea)

measurements were fragmentary. Extra- and interpolation of data made the information error-prone in many regions. In answer to the fatal storm surge of 1953, the interest in hydrodynamical modeling of storm surges in the North Sea and consequently the simulation of tides were reinforced.

Some of the earliest FD models of the North Sea were from Hansen in the 1950ties (Hansen, 1952). Although the models were coarse, they could reproduce the main amphidromic points of  $M_2$ . Tidal elevations and currents could be validated by observations (Brettschneider, 1967a,b). But to calculate satisfactory surge profiles more advanced FD tidal models, which accounted for non-linearities and the interaction between surges and tides, had to be developed (Heaps, 1969; Flather, 1976). One difficulty they encountered was the formation of spurious eddies, which were mainly due to the poor resolution of the bottom topography. Finer resolving (Maier-Reimer, 1977; Pingree & Griffiths, 1978) and three dimensional models (Backhaus, 1979) were soon developed and gave more detailed simulation results.

The list of FD models can be extended easily, e.g., by Runday (1973), Marchuk *et al.* (1973), Runday (1975), Davies (1976), Prandle (1978), Davies & Furnes (1980), Davies (1986), Davies *et al.* (1997a) and Davies *et al.* (1997b) to mention just a few of them. Major improvements in realism of the computations were done by including density as diagnostic variable to compute baroclinic components of the current (Backhaus, 1985) and by incorporating time dependend wind fields (Hainbucher *et al.*, 1986). In terms of numerical methods, the introduction of the staggered grid approach (Arakawa C-grid) avoided artificial short waves (Westerink & Gray, 1991). These FD

models were and are still used in numerous studies, for example in Sinha & Pingree (1997). In order to better resolve the coastline with manageable computational loads, the structured grid models have to use nesting techniques. Coarser models on wider domains provide fine resolution, local models with open boundary conditions. For example, the BSHcmod (Dick *et al.*, 2001) is an operational tidal, storm surge model with nested domains.

To realize varying grid solution the unstructured grid methods are very promising. Their development is contiguous to the development of computers in the early sixties and seventies. Early FE models (such as Brebbia & Partridge (1976) and Grotkop (1973)) of the North Sea were plagued with spurious or numerical noise. They had to use excessive damping mechanisms, which made results inaccurate (Gray, 1982; Gray & Kinnmark, 1983).

With the replacement of the continuity equation by the wave continuity equation (WCE, see Section 1.1) developed by Lynch & Gray (1979), the node-to-node oscillations were significantly reduced. Gray (1989) and Kinnmark & Gray (1984) employed the WCE to compute tides in the North Sea. They used very coarse grids in the southern North Sea and English channel and compared their results with elevation at some stations.

MOG2D (2D Gravity Waves Model, Carrère & Lyard (2003)) is another WCE model formulated in spherical coordinates and discretized with  $P_1 - P_1$  finite elements. It was tested by Kliem *et al.* (2006) in the North and Baltic Sea, but did not prove to be better than existing FD models. Although FE should be superior the model showed to be even worse in shallow, complex coastlines than existing FD models.

As the GWCE promises to better fulfill the continuity equation than the WCE more models are based on GWCE or existing models are reformulated. For example the successor of the MOG2D is the T-UGOm, which uses the GWCE.

One GWCE model is ADCIRC (ADvanced CIRCulation Model for Shelves, Coasts, and Estuaries) developed amongst others by Luettich *et al.* (1992) and Westerink *et al.* (1992). It includes all constituents and also the equilibrium tidal potential (Luettich & Westerink, 2004). In the scope of the Tidal Flow Forum in 1984, the former ADCIRC-2DDI was tested against station data at 11 harbors in the southern North Sea and the English Channel (Blain & Rogers, 1998). Compared to the models of Walters (1987) or of Werner & Lynch (1989), the rms error was smaller on the same grid and data set. Walters (1987) had the approach to project time dependency on the frequency domain. By inserting the momentum into the continuity equation a Helmholtz type equation resulted. It was solved together with the momentum equation iteratively with FE methods. A review of the general outcome of the Tidal Flow Forum was published by Werner (1995). The models showed better results in simulating the singular partial tides than the total tide, which indicates that they insufficiently described the complete

non-linear dynamics. This demonstrates the importance of correctly modeling the non-linear interaction between the tides and the bottom topography. QUODDY is a 3-D, nonlinear finite element coastal ocean model with advanced turbulence closure (Lynch *et al.*, 1996, 1997), but it also has a 2D version using the GWCE. Hall & Davies (2005) used QUODDY in the Irish Sea and compared the baroclinic, internal tide results with a well tuned finite difference model. The fine resolution finite element simulations reproduced more accurately the generation and propagation of the internal tide, but some unphysically spurious waves had to be damped by additional dissipation along steep slopes. One conclusion was that rapid mesh refinement should be avoided in order to inhibit increasing energy at small scales.

Obviously, the list of two and three dimensional GWCE models can be extended easily, but because of mass conservation deficiency I will only give some examples of models, which do not solve the equations in the form of a GWCE. One example is the 2D finite element model TELEMAC-2D (Hervouet & Van Haren, 1994), which solves the shallow water equations in conservative form. It uses  $P_1$  and quasi-bubble elements. Hervouet (2007) constructs the latter by adding a fourth node into the triangle (usually the center of gravity) and defining piecewise linear functions on each node. To treat the hyperbolic and parabolic part of the equation separately the operator-splitting method is applied. The solution is first obtained for the advection term and then for the propagation, diffusion and source terms (Fernandes *et al.*, 2002). For example the POL (Proudman Oceanographic Laboratory, UK) use TELEMAC to simulate the tides in the Irish Sea and the BAW (Bundesanstalt für Wasserbau, Germany) make simulations in the North- and Baltic Sea with it (see Plüß, 2002, for simulation results).

Other tidal simulation on an unstructured grid in the North Sea were made by the SLIM (Second-generation Louvain-la-Neuve Ice-ocean Model, see the website <http://sites.uclouvain.be/slim> and the publications mentioned therein). In the North Sea, they focused on the Scheldt estuary and simulation of contaminant transport. The model is coupled to a 1D river model. It uses NCEP Reanalysis wind and pressure fields and includes two wetting and drying schemes. In contrast to the FE models above they use linear DG methods. There are several other unstructured grid models simulating tides in the North Sea, e.g., by the Delfin model (Ham, 2006), which is a hybrid FV/FE model, or UnTRIM by Casulli & Walters (2000) using orthogonal meshes. UnTrim has been applied to the Jade-Weser estuary, but the orthogonality is a limitation on the usability of grids and requires special routines for mesh generation.

## 1.4 Conclusion

Unstructured grid models have the advantage in being more flexible with respect to the underlying mesh, as well as offering much more freedom in the choice of the numerical method. Although this thesis only deals with the two dimensional flow equations, already there are on this level many different FV and FE methods and it is not clear which one is best suited for ocean models. Some of them may generate numerical modes, others are computationally too expensive. I narrow the methods, that I want to investigate, to two FE -  $P_1^{NC} - P_1$  and  $P_1 - P_1$  - and one FV method by Chen *et al.* (2003).  $P_1 - P_1$  is widely used and commonly in combination with GWCE to suppress pressure modes. Instead of GWCE, I will use a different kind of stabilization.  $P_1^{NC} - P_1$  prohibits pressure modes naturally due to the bigger number of unknowns for the velocity. The FV method from Chen *et al.* (2003) is chosen, as it is not restricted to orthogonal meshes in contrary to, for example, the FV method of Casulli & Walters (2000) implemented in UnTRIM.

As velocity and elevation are treated differently, these three spatial discretization methods do not have the same number of unknowns on the same grid. To investigate the performance of models, the time stepping scheme is also important and, therefore, explicit as well as semi-implicit methods will be implemented. Often numerical models are compared theoretically on grid basis or in idealized test cases. But obviously, model simulations of problems with a realistic size and geometry reveal additional insight into the processes that may not be fully tested with simple test cases. Sometimes realistic applications show problems, that did not appear formerly. Intercomparisons between models on realistic meshes are therefore very rare.

Tides are prominent in oceanic processes on many scales ranging from global to coastal. Unstructured grid models already proved to be very powerful in resolving the small features, e.g. of coastal bays and inlets. To compare and validate hydrodynamical ocean models in coastal applications, the tides are a realistic test case. Of course there are many more oceanic processes than just the tides and further testing is still required. The influence of tides on mixing and the thermohaline stratification makes them even a good test setup for future three dimensional model testing, although this is left for future studies for the moment.

The study area under consideration is the North Sea and its neighboring seas. The North Sea itself has a long history of observations and model applications and is, therefore, best suited for model validation and comparison. The main tidal signal is barotropic and therefore a two dimensional model is sufficient in most cases. Over- and compound tides are generated by non-linear effects and become in some areas as big as diurnal tides, which means that a faithful representation of bathymetry, coastline and the non-linear terms in the momentum and continuity equation are needed. The numerical treatment of the non-linear terms, especially the advection, is some-

times not straightforward. Also the bottom friction term has influence on the elevation and velocity of the tidal wave, but its coefficient is largely unconstrained by measurements.

Tuning of a model to fit to observation often means to optimize parameters. Although unstructured grid models represent the coastal shape better than structured ones, there is still a need for tuning these models. Almost all already existing tidal, unstructured grid models in the North Sea do not have systematic procedures like an adjoint model to tune parameters (the only exception is TELEMAC-2D). The codes are often too complex or the models are still in the development stage, such that coding of the adjoint model will always lag behind the forward code or may simply be impossible at all. Therefore, the models used in this thesis do not make use of already existing code from other unstructured grid tidal models. They have to be coded in a specific way such that automatic differentiation are able to generate the adjoint model. This thesis starts with the most simple setup, namely the two dimensional shallow water equations without solving for temperature and salinity. As mentioned in the section about the North Sea, there are many more processes in the ocean that cannot be taken into account with such a simple model. The way to obtain an adjoint model is therefore very important. If automatic differentiation shows to be useful for unstructured grid models, it can be used parallelly with the further development of the model.

## 2 Unstructured mesh tidal models

Section 2.1 describes the FE and FV unstructured grid models under consideration in the thesis. They are used for model intercomparison and validation, as well as the generation of an adjoint model. These models are allowed in applications, where the shallow water equations are permissible. First, I discuss the FE discretization in Section 2.1.1 and the FV discretization in Section 2.1.2. Then the models are set up for tidal simulations and I summarize this setup in Section 2.1.3 and 2.1.4. To compute energy balance some discrete representation has to be found. This is done in Section 2.1.5.

Section 2.2 is the second part of this chapter and addresses the model simulation results. I compare the performance of seven models on a North and Baltic Sea grid in Section 2.2.1. The models differ in the spatial and/or temporal discretization. The models are compared by computing the error with respect to elevation observations and the CPU run times for the model integration. After this intercomparison I want to give a more detailed discussion of the model's ability to represent the tidal regime. Extending the mesh to the European Continental Shelf in Section 2.2.2 weakens the influence of the spurious open boundary reflections. I use this new mesh with one of the models, which was performing good in the model intercomparison, to discuss the tidal simulations in terms of energy balance, residual currents and current ellipses.

### 2.1 Model description

The basic principle of the following considerations is based on the conservation of fluid momentum and mass. The resulting equations are the Navier-Stokes equations (see, e.g., Anderson, 1995). The ocean additionally conserves salt and heat content (see, e.g., Cushman-Roisin, 1994). To simplify the system of equations, the effect of compressibility is mainly retained in the equation of state and neglected in the momentum balance except for the contribution through the gravitational acceleration. This approach is called Boussinesq approximation (see, e.g., Cushman-Roisin, 1994). Further information on the consequences of the Boussinesq approximation on hydrodynamical ocean simulations are presented by Losch *et al.* (2004). For the

Boussinesq approximation it is assumed that the density changes are small compared to a constant mean density. So mass conservation transforms to volume conservation.

Tides in shelf seas have characteristic orders of velocities and spatial lengths. They are used to further simplify the Reynolds-averaged Navier-Stokes equations. If I consider  $U$  resp.  $W$  to be the order of horizontal resp. vertical velocity,  $D$  being the order of the depth and  $L$  the typical order of horizontal dimensions, then the aspect ratio  $WD/UL$  is supposed to be very much smaller than one. This justifies the use of the hydrostatic approximation. Since tidal pressure variations are mostly due to elevation, the horizontal pressure gradients and hence the horizontal velocity are independent of the vertical coordinates (see, e.g., Pedlosky, 1987). By vertically integrating the equations of horizontal momentum and continuity the 2-dimensional shallow water equations are obtained.

The momentum equation in non-conserving form is used in the FE codes (NCLF, NCAB, NCSI, P1P1),

$$\frac{\partial \mathbf{u}}{\partial t} + f\mathbf{k} \times \mathbf{u} + g\nabla\eta + (\mathbf{u} \cdot \nabla)\mathbf{u} = \nabla(A\nabla\mathbf{u}) - rH^{-1}|\mathbf{u}|\mathbf{u}, \quad (2.1)$$

For the FV codes (FVAB, FVRK and FVSI) the conserving, flux form is applied,

$$\frac{\partial \mathbf{U}}{\partial t} + f\mathbf{k} \times \mathbf{U} + gH\nabla\eta + \nabla \cdot (\mathbf{U}\mathbf{u}) = H\nabla(A\nabla\mathbf{u}) - r|\mathbf{u}|\mathbf{u}. \quad (2.2)$$

Here  $\mathbf{u} = (u, v)$  is the horizontal velocity,  $\mathbf{U} = H\mathbf{u}$  is the transport and  $H = \eta + H_0$  the total fluid depth with  $H_0$  being the unperturbed water depth and  $\eta$  its deviation. Further,  $f$  is the Coriolis parameter,  $\mathbf{k}$  the upward unit vector,  $r$  the bottom friction coefficient,  $g$  the gravitational acceleration and  $A$  the viscosity coefficient, which is either taken either as constant ( $A = 10 \frac{m^2}{s}$ ) or depending on mesh and time step size.

To make the set of equations complete, I mention the continuity equation, too. It also follows from the considerations mentioned above, being

$$\frac{\partial \eta}{\partial t} + \nabla \cdot \mathbf{U} = 0. \quad (2.3)$$

for the FV codes or, equivalently,

$$\frac{\partial \eta}{\partial t} + \nabla \cdot (\eta + H_0)\mathbf{u} = 0. \quad (2.4)$$

for the FE codes (NCLF, NCAB, NCSI, P1P1).

### 2.1.1 FE discretization

In order to solve the Eqns.(2.1) and (2.4) with the FE method, the equations are reformulated in the variational sense. This means that they are

multiplied by functions - the so called test functions - and integrated over the domain. The solution and the testfunctions are elements of a suitable subspace  $\tilde{H}$  of the Sobolev space  $H^1(\Omega)$ , where  $\Omega$  is our domain on the Earth surface. Here,  $H^1(\Omega)$  is the function space of square-integrable functions  $L^2(\Omega)$ , whose first derivatives also belong to  $L^2(\Omega)$  (for a more detailed description about FE methods, see, e.g., Braess, 2007). This subspace has to be chosen decently such that  $(\mathbf{u}, \eta) \in \tilde{H}_1 \times \tilde{H}_1 \times \tilde{H}_2$  guarantees the existence and uniqueness of the weak solution. For this purpose suitable conditions for elevation and velocity have to be set and the boundary  $\delta\Omega$  has to be divided into coastal  $\Gamma_1$  and open/wet boundary  $\Gamma_2$  part. At the closed boundary  $\Gamma_1$  I prescribe either  $\mathbf{u} = 0$  or  $\mathbf{u} \cdot \mathbf{n} = 0$  together with the requirement that tangent viscous stress be zero. For the open boundary  $\Gamma_2$  the sea surface elevation is calculated from global tidal model. Details about the open boundary conditions are in Section 2.1.3.

The next step is to subdivide the domain  $\Omega$  into a discrete space, i.e.  $\Omega = \bigcup_e \Omega_e$ , where  $\Omega_e$  are triangles. Then the solution of the variational formulation is approximated by a finite dimensional vector space of basis functions. The same is done with the test functions. This technique is known as Ritz-Galerkin method.

Here, the discrete space consists of piecewise linear functions on the triangles. For the P1P1 model, elevation and velocity are two dimensional hat functions with the value one on the node (see Fig. 1.1). NCLF, NCAB and NCSI use the same functions for elevations, but here the velocity functions are associated with edges. They are so called non-conforming  $P_1$  or short  $P_1^{NC}$  functions.

For example, Hanert *et al.* (2005) and Le Roux *et al.* (2005) investigated these type of elements. The non-conforming element pair  $P_1^{NC} - P_1$  has the advantage that it is little affected by computational modes (Le Roux *et al.*, 2005, 2007; Le Roux, 2005). The velocity modes, that can still be excited, are suppressed by viscosity.

I follow Hanert *et al.* (2004) for the discretization of the advection term, but had to give a new type of advection scheme for numerical reasons. It is described below.

Further, for the temporal discretization usually FD methods are employed. The time-stepping schemes Leap-frog (NCLF), Adam-Bashforth (NCAB) and semi-implicit (NCSI) are described in the following sections.

## NCSI

For the semi-implicit code I use the simple upwind scheme for the temporal discretization and derive from Eqn.(2.1) and (2.4) the following equations for

velocity  $\mathbf{u}^n = (u^n, v^n)$  and sea surface elevation  $\eta^n$  at time  $t_n$ :

$$\begin{aligned} & \frac{\mathbf{u}^{n+1}}{\delta t} + \beta f \times \mathbf{u}^{n+1} + \theta g \nabla \eta^{n+1} \\ &= \frac{\mathbf{u}^n}{\delta t} - (1 - \beta) f \times \mathbf{u}^n - (1 - \theta) g \nabla \eta^n - (\mathbf{u}^n \cdot \nabla) \mathbf{u}^n \\ & \quad - \frac{r}{H_0 + \eta^n} |\mathbf{u}^n| \mathbf{u}^n + \nabla (A \nabla \mathbf{u}^n) \end{aligned} \quad (2.5)$$

$$\frac{\eta^{n+1} - \eta^n}{\delta t} + \nabla (H_0 + \eta^n) (\alpha \mathbf{u}^{n+1} + (1 - \alpha) \mathbf{u}^n) = 0, \quad (2.6)$$

where the default value for parameters  $\beta$ ,  $\theta$  and  $\alpha$  is 0.5. The values of the implicitness parameters  $\theta$  and  $\alpha$  should be between 0.5 and 1 for stability reasons (Casulli & Cattani, 1994), so I used 0.55 in most of the simulations. To discretize the equations spatially I multiply Eqn.(2.6) with a test function in  $P_1$  and Eqn.(2.5) with a test function in  $P_1^{NC}$ . Then I replace  $\mathbf{u}^n = (u^n, v^n)$  resp.  $\eta^n$  by their spatial approximation in  $P_1^{NC}$  resp.  $P_1$ .

This leads to the following linear system

$$\begin{aligned} \mathbf{M}_u \mathbf{u}^{n+1} = & \mathbf{M}_u \mathbf{u}^n - \delta t \mathbf{M}_f (\beta \mathbf{u}^{n+1} + (1 - \beta) \mathbf{u}^n) \\ & - \delta t \mathbf{G}_u (\theta \eta^{n+1} + (1 - \theta) \eta^n) \\ & - \delta t B(\mathbf{u}^n) \mathbf{u}^n - \delta t \mathbf{D} \mathbf{u}^n + \delta t \mathbf{C}(\mathbf{u}^n, \mathbf{u}^n), \end{aligned} \quad (2.7)$$

$$\mathbf{M}_\eta \eta^{n+1} = \mathbf{M}_\eta \eta^n - \delta t \mathbf{G}_\eta (H_0) (\alpha \mathbf{u}^{n+1} + (1 - \alpha) \mathbf{u}^n) - \delta t \mathbf{G}_\eta (\eta^n) \mathbf{u}^n \quad (2.8)$$

where  $\mathbf{M}_u$  and  $\mathbf{M}_\eta$  are the velocity and elevation mass matrices,  $\mathbf{M}_f$  is the matrix of the Coriolis operator,  $\mathbf{G}_u$  and  $\mathbf{G}_\eta$  are the gradient and divergence operators,  $B$  is the quadratic bottom drag operator,  $\mathbf{D}$  is the viscosity matrix and  $\mathbf{C}$  denotes the advection operator. For more details about the treatment of the non-linear terms see, e.g., Danilov *et al.* (2008).

Due to the orthogonality of the velocity basis functions the mass matrix on  $\mathbf{u}^n$  is diagonal and is therefore easily inverted.

$$\begin{aligned} \mathbf{u}^{n+1} = & (\mathbf{M}_u + \delta t \mathbf{M}_f \beta)^{-1} (\mathbf{M}_u \mathbf{u}^n - \delta t \mathbf{M}_f (1 - \beta) \mathbf{u}^n - \delta t \mathbf{G}_u (1 - \theta) \eta^n \\ & - \delta t B(\mathbf{u}^n) \mathbf{u}^n - \delta t \mathbf{D} \mathbf{u}^n + \delta t \mathbf{C}(\mathbf{u}^n, \mathbf{u}^n)) - (\mathbf{M}_u + \delta t \mathbf{M}_f \beta)^{-1} \delta t \mathbf{G}_u \theta \eta^{n+1}. \end{aligned}$$

The expression of  $\mathbf{u}^{n+1}$  in terms of  $\eta^{n+1}$  is then substituted into the continuity equation and one gets a linear system for  $\eta_{n+1}$  with a time independent stiffness matrix. This results in a sparse and -if the time step is small enough- diagonal dominant matrix equation.

$$\begin{aligned} & (\mathbf{M}_\eta - \delta t \mathbf{G}_\eta (H_0) \alpha (\mathbf{M}_u + \delta t \mathbf{M}_f \beta)^{-1} \delta t \mathbf{G}_u \theta) \eta^{n+1} = \\ & \mathbf{M}_\eta \eta^n - \delta t \mathbf{G}_\eta (H_0) (1 - \alpha) \mathbf{u}^n - \delta t \mathbf{G}_\eta (\eta^n) \mathbf{u}^n - \delta t \mathbf{G}_\eta (H_0) \alpha \mathbf{R}, \end{aligned}$$

where  $\mathbf{R} = (\mathbf{M}_u + \delta t \mathbf{M}_f \beta)^{-1} (\mathbf{M}_u \mathbf{u}^n - \delta t \mathbf{M}_f (1 - \beta) \mathbf{u}^n - \delta t \mathbf{G}_u (1 - \theta) \eta^n - \delta t B(\mathbf{u}^n) \mathbf{u}^n - \delta t \mathbf{D} \mathbf{u}^n + \delta t \mathbf{C}(\mathbf{u}^n, \mathbf{u}^n))$ . It has to be assembled and factorized only once. The PETSc solver solves this matrix equation for  $\eta_{n+1}$ . Having  $\eta^{n+1}$  found, it is used to calculate  $\mathbf{u}^{n+1}$ . This semi-implicit scheme has the advantage that the time step size  $\delta t$  can be larger compared with the explicit codes NCLF and NCAB studied here.

## NCLF

For the NCLF version a standard leapfrog time stepping with a weak filtering is applied to suppress the numerical mode. The velocity and the elevation analogously is updated as

$$\begin{aligned} \mathbf{u}^{n-1} &= \mathbf{u}^n + \chi(\mathbf{u}^{n+1} - 2\mathbf{u}^n + \mathbf{u}^{n-1}), \\ \mathbf{u}^n &= \mathbf{u}^{n+1}, \\ \mathbf{u}^{n+1} &= \mathbf{u}^{new}. \end{aligned}$$

Here,  $\chi$  is a small numerical factor. Since the mass matrix  $\mathbf{M}_\eta$  is not diagonal it is replaced in NCLF by its lumped approximation to ensure a numerically efficient code. Le Roux *et al.* (2009) showed that lumping the elevation mass matrix has a significant influence only on small scales ( $kh > \pi/2$ , where  $k$  is the wave number and  $h$  characteristic mesh spacing). In that way it remains accurate for tidal applications, where waves are generally well resolved. The advantage of NCLF is its algorithmic simplicity and absence of solver calls, which may serve as benefit in parallel setups.

## NCAB

The NCAB version uses lumping of  $\mathbf{M}_\eta$  and does not invoke solvers as well. Its implementation is analogous to the FVAB presented in Section 2.1.2. NCAB does not have the numerical modes of NCLF and is more accurate, but requires more storage.

## P1P1

The P1P1 model uses the linear, continuous functions  $P_1$  for velocity and elevation. This implies that the mass matrices are not diagonal for both variables. Additionally, this discretization is known to support pressure modes. To eliminate them without recourse to the GWCE method, an elevation correction method is used.

The time discretization of the momentum equation is as follows:

$$\mathbf{u}^{n+1} - \mathbf{u}^n + g\delta t \nabla(\theta \eta^{n+1} + (1 - \theta) \eta^n) = \delta t \mathbf{F}^{AB2} + \delta t \mathbf{F}_d^n,$$

where

$$\mathbf{F} = -f\mathbf{k} \times \mathbf{u} - (\mathbf{u} \cdot \nabla)\mathbf{u},$$

and the dissipative term is

$$\mathbf{F}_d = -rH^{-1}|\mathbf{u}|\mathbf{u} + \nabla \cdot (A\nabla\mathbf{u}).$$

The estimation of  $\mathbf{F}$  is, for stability, given by second-order Adams–Bashforth, with modified coefficients  $(3/2+\epsilon, -1/2-\epsilon)$ , e.g.,  $\mathbf{F}^{AB2} = (3/2 + \epsilon)\mathbf{F}^n - (1/2 + \epsilon)\mathbf{F}^{n-1}$ . A third-order Adams–Bashforth method could easily be used with the price of some additional storage.

The elevation equation is discretized in the standard semi-implicit way

$$\eta^{n+1} - \eta^n + \delta t \nabla \cdot (H_0(\alpha \mathbf{u}^{n+1} + (1 - \alpha)\mathbf{u}^n)) = \delta t R_\eta^{AB2},$$

where

$$R_\eta := -\nabla \cdot \eta \mathbf{u}.$$

Once again, for stability it is estimated with the Adams–Bashforth method. It is not possible to solve these equations in the way used for the NCSI because of elevation modes and non-diagonal mass matrices. The following strategy is adopted from FEOM (Wang *et al.*, 2008a,b).

First, a predictor step is done

$$\mathbf{u}^* - \mathbf{u}^n = \delta t \mathbf{F}^{AB2} + \delta t \mathbf{F}_d^n - g \delta t \nabla (\gamma \eta^n). \quad (2.9)$$

Here,  $\gamma \leq 1$  is the stabilization parameter. Second, the predictor step has to be complemented by the corrector step

$$\mathbf{u}^{n+1} - \mathbf{u}^* = -g \delta t \nabla (\theta \eta^{n+1} + (1 - \theta - \gamma)\eta^n). \quad (2.10)$$

Using  $\mathbf{u}^{n+1}$  from the last expression and substituting the result in the continuity equation (note that this is done before the spatial discretization, which is a noticeable difference compared to the NCSI case) leads to:

$$\begin{aligned} \eta^{n+1} - g \delta t^2 \alpha \theta \nabla \cdot (H_0 \nabla \eta^{n+1}) &= \eta^n + \delta t R_\eta^{AB2} - \delta t (1 - \alpha) \nabla \cdot (H_0 \mathbf{u}^n) \\ &\quad + g \delta t^2 \alpha (1 - \theta - \gamma) \nabla \cdot (H_0 \nabla \eta^n) \\ &\quad - \delta t \alpha \nabla \cdot (H_0 \mathbf{u}^*). \end{aligned} \quad (2.11)$$

The essence of this algorithm is that all three equations are discretized with the finite element method. First, one solves the FE-discretized version of Equation (2.9) to estimate the predictor velocity. Then the FE-discretized version of Equation (2.11) is solved and, finally, the corrected velocity is computed.

The numerical implementation of Eqn.(2.11) exploits PETSc with BICGStab, while Eqns.(2.9) and (2.10) use iterative algorithms to invert mass matrices occurring. Despite these additional matrix inversions the algorithm is reasonably fast and competes well with other semi-implicit codes.

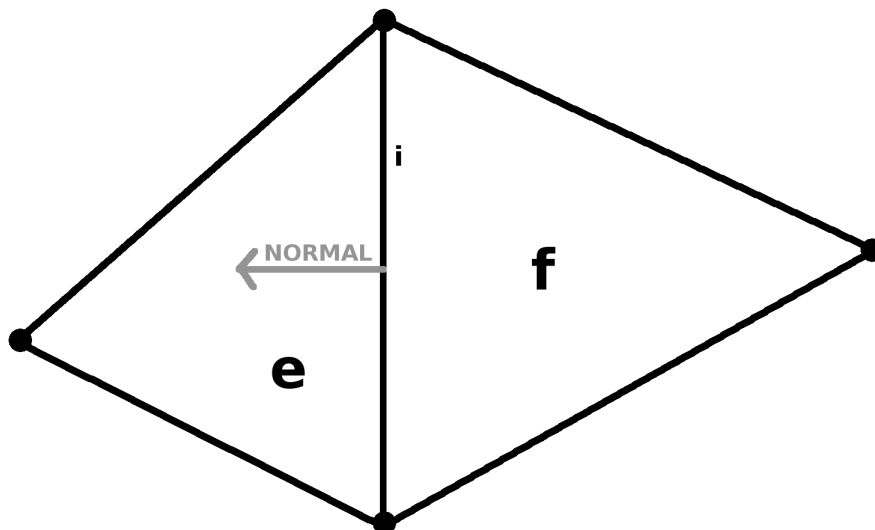


Figure 2.1: Schematic plot of edge  $i$  common to triangles  $e$  and  $f$ , outer normal is with respect to triangle  $f$

Note that the main difference to the GWCE method is that the velocity field of Eqn.(2.10) satisfies now the continuity equation if taken literally in the sense of this equation, before FE projection. The strength of stabilization is controlled by parameter  $\gamma$  which is selected as close to one as possible ( $\gamma=0.95-0.97$ ). Unfortunately, the algorithm cannot be made fully explicit.

### Advection for NC models

When velocity is discretized with  $P_1^{NC}$  functions, it is continuous only at mid edges and may be discontinuous on the rest of the edge. In the following I consider an edge  $i$  and denote by  $e$  and  $f$  the two triangles that are adjacent to it. The jump at an edge  $i$  comes from the values of the four edges belonging to the triangles  $e$  and  $f$  not being equal to the edge  $i$  (see Fig. 2.1). The weak formulation of the momentum equation means to multiply the equations with a test function (namely elements of  $P_1^{NC}$  or  $P_1$ , see Appendix for the definitions of the test functions) and to integrate over the domain. The integration over the domain is split into a sum over the integrations on the triangles. Partial integration of the advective term gives an integral over the boundary of elements, where the velocity has the jump. Hanert *et al.* (2005) propose to weakly impose continuity by a centered or upwind momentum advection scheme. I will summarize this scheme and add two new schemes, that do not use Greens formula and, therefore, do not have to evaluate boundary integrals.

### Advection after Hanert *et al.* (2005)

As it has been proposed by Hanert *et al.* (2005), the usual procedure including partial integration of the advective term yields the following weak form of the advective term

$$\sum_{e=1}^{N_e} \int_{\Omega_e} -(\nabla \cdot (\mathbf{u}\hat{\mathbf{u}})) \cdot \mathbf{u} \, d\omega + \sum_{e=1}^{N_e} \int_{\partial\Omega_e} (\mathbf{u}\mathbf{u} \cdot \mathbf{n}_e) \cdot \hat{\mathbf{u}} \, d\Gamma + \sum_{l=1}^{N_\Gamma} \int_{\Gamma_l} [\mathbf{u}] \cdot [a(\hat{\mathbf{u}})] \, d\Gamma,$$

where  $N_e$  is the number of elements and  $N_\Gamma$  the number of interelemental edges.  $\Omega_e$  resp.  $\partial\Omega_e$  are triangles resp. boundary of triangles.  $\hat{\mathbf{u}}$  is either  $(\Psi_i, 0)$  or  $(0, \Psi_i)$ , where  $\Psi_i$  is a non-conforming test function (see Appendix). In the last term I used the notation  $[\mathbf{u}] := \mathbf{u}_e - \mathbf{u}_f$ , where  $\mathbf{u}_e$  resp.  $\mathbf{u}_f$  is the velocity restricted to the triangle  $e$  resp.  $f$ . The sum over the interelemental edges is the weak continuity constraint on the velocity.  $a$  is defined as

$$a(\hat{\mathbf{u}}) = \begin{cases} +\frac{1}{2}(\mathbf{u} \cdot \mathbf{n})\hat{\mathbf{u}} & \text{on } \Omega_e \\ -\frac{1}{2}(\mathbf{u} \cdot \mathbf{n})\hat{\mathbf{u}} & \text{on } \Omega_f, \end{cases}$$

where  $\mathbf{n}$  is the normal to the edge  $l$  pointing from  $\Omega_f$  into  $\Omega_e$ .

### Heaviside $P_1^{NC}$ advection

The basis functions of  $P_1^{NC}$  may also be considered in terms of distribution theory. Using the Heaviside function  $\Theta_e$  being 1 on the triangle, 0.5 on the boundary of the triangle and 0 everywhere else, the non-conforming test function is then written as

$$\Psi_i = \Psi_{ie} + \Psi_{if},$$

where  $\Psi_{ie} := \Theta_e \psi_{e_i}$  and  $\psi_{e_i}$  is a linear function on the triangle  $\Omega_e$  with 1 on edge  $i$  and -1 on the opposing node to the edge  $i$  (see Appendix for further details).  $\psi_{e_i}$  is zero outside the triangle  $\Omega_e$ .

The Heaviside function serves to weight the function values on the triangle boundary. This will result in a natural way to constrain continuity on the edges.

Since the test/basis functions  $\Psi_i$  are well defined everywhere in our domain, they can be handled as in the continuous case, without invoking the machinery of flux penalties to get correct variational formulations with discontinuous functions.

The coordinate system transforms such that  $x$  is tangential and  $y$  is perpendicular to the edge  $i$  pointing from  $\Omega_f$  into  $\Omega_e$ . This means that I can rewrite the advection term in the following form

$$(\mathbf{u} \cdot \nabla)\mathbf{u} = \left( u_s \frac{\partial}{\partial s} + u_n \frac{\partial}{\partial n} \right) \mathbf{u}, \quad (2.12)$$

where  $u_s = \mathbf{u} \cdot \mathbf{s}$  and  $u_n = \mathbf{u} \cdot \mathbf{n}$  (i.e. the projection of  $\mathbf{u}$  in tangential resp. normal direction of edge  $i$ ). The tangential derivative is discontinuous, but does not contain singularities, as  $\mathbf{u}$  consists of linear functions. Only the second term contains singularities at the edge. I define  $\mathbf{u}_f$  resp.  $\mathbf{u}_e$  as the sum of the contributions from the non-conforming functions on element  $e$  resp.  $f$ , i.e.,

$$\begin{aligned}\mathbf{u}_f &:= \mathbf{u}_{j_1} \psi_{j_1 f} + \mathbf{u}_{j_2} \psi_{j_2 f} + \mathbf{u}_{j_3} \psi_{j_3 f}, \\ \mathbf{u}_e &:= \mathbf{u}_{i_1} \psi_{i_1 e} + \mathbf{u}_{i_2} \psi_{i_2 e} + \mathbf{u}_{i_3} \psi_{i_3 e},\end{aligned}$$

where  $j_1, j_2, j_3$  denote the edges on element  $f$  and  $i_1, i_2, i_3$  the edges on element  $e$ . In the vicinity of edge  $i$  the velocity can be written as

$$\mathbf{u} = \mathbf{u}_f + \Theta_e(y)(\mathbf{u}_e - \mathbf{u}_f),$$

where  $\Theta_e$  only depends on the coordinate  $y$  perpendicular to the edge. Placing this result into the advection term and using the fact that the Diracs delta function  $\delta$  is the normal derivative of  $\Theta_e$ , the singular part of the second term of Eqn.(2.12) is

$$(\mathbf{u}_f + \Theta_e(y)(\mathbf{u}_e - \mathbf{u}_f)) \cdot \mathbf{n} \delta(y) (\mathbf{u}_e - \mathbf{u}_f),$$

In order to obtain the weak formulation of the advective term, it is multiplied with a testfunction  $\hat{\mathbf{u}}$  and integrated over the domain. In the following I take  $\hat{\mathbf{u}}$ , as the sum over all test functions, to compute the contribution of all test functions to the value on edge  $i$ , e.g.,

$$\begin{aligned}\hat{\mathbf{u}}_f &= (\psi_{j_1 f} + \psi_{j_2 f} + \psi_{j_3 f}, 0) \text{ or } (0, \psi_{j_1 f} + \psi_{j_2 f} + \psi_{j_3 f}), \\ \hat{\mathbf{u}}_e &= (\psi_{i_1 e} + \psi_{i_2 e} + \psi_{i_3 e}, 0) \text{ or } (0, \psi_{i_1 e} + \psi_{i_2 e} + \psi_{i_3 e}),\end{aligned}$$

and

$$\int_0^1 \int_{-\epsilon}^{+\epsilon} (\hat{\mathbf{u}}_f + \Theta_e(y)(\hat{\mathbf{u}}_e - \hat{\mathbf{u}}_f)) \cdot ((\mathbf{u}_f + \Theta_e(y)(\mathbf{u}_e - \mathbf{u}_f)) \cdot \mathbf{n}) \delta(y) (\mathbf{u}_e - \mathbf{u}_f) dy dx$$

After the integration over  $y$  I get with the relationships  $\int \Theta_e(y) \delta(y) dy = 1/2$ ,  $\int \Theta_e(y) \Theta_e(y) \delta(y) dy = 1/4$  and  $\int \delta(y) dy = 1$

$$\int_0^1 \hat{\mathbf{u}}_f \cdot (\mathbf{u}_f \cdot \mathbf{n}) [\mathbf{u}] + \frac{1}{2} [\hat{\mathbf{u}}] \cdot (\mathbf{u}_f \cdot \mathbf{n}) (\mathbf{u}_e - \mathbf{u}_f) + \frac{1}{2} \hat{\mathbf{u}}_f \cdot ([\mathbf{u}] \cdot \mathbf{n}) [\mathbf{u}] + \frac{1}{4} [\hat{\mathbf{u}}] \cdot ([\mathbf{u}] \cdot \mathbf{n}) [\mathbf{u}] dx \quad (2.13)$$

To make writing easier  $\mathbf{n}$  is always the outer normal to the triangle  $f$ .  $\mathbf{n}$  constant also if it is written inside the terms  $[\ ]$  and  $\langle \rangle$ , i.e.  $[\mathbf{u}] \cdot \mathbf{n} = [\mathbf{u} \cdot \mathbf{n}]$ . After some calculations (see Appendix) I obtain

$$\int_0^1 \langle \hat{\mathbf{u}} \rangle \cdot \langle \mathbf{u} \cdot \mathbf{n} \rangle [\mathbf{u}] dx \quad (2.14)$$

With this notation the continuity constraint of Hanert is analogously derived and can be written as

$$\begin{aligned} \mathbf{u}t \cdot [a(\hat{\mathbf{u}})] &= [\mathbf{u}] \cdot \langle \mathbf{u} \cdot \mathbf{n} \hat{\mathbf{u}} \rangle \\ &= [\mathbf{u}] \cdot \langle \mathbf{u} \cdot \mathbf{n} \rangle \langle \hat{\mathbf{u}} \rangle + \frac{1}{4} [\mathbf{u}] \cdot [\mathbf{u} \cdot \mathbf{n}] [\hat{\mathbf{u}}] \end{aligned} \quad (2.15)$$

Comparing Eqn.(2.15) and the term obtained by the Heaviside calculation Eqn.(2.14) the only difference is the second term of Eqn.(2.15). This term does not contribute, as the integration over the edge is done over the product of three linear functions with zero at the half edge length.

### $P_1$ projection method for advection

To calculate the advection term in the momentum equation I first project the velocity from the  $P_1^{NC}$  to the  $P_1$  space in order to smooth it. Then the projected velocities is used in the advection term and it is proceeded as usual by multiplying this form with a  $P_1^{NC}$  basis functions and integrating over the domain. This eliminates discontinuities and thus the need to treat additional edge contributions.

### Discussion of the advection schemes

Although the Hanert and the Heaviside advection scheme are obtained in a completely different manner, the schemes are analogous and should not lead to different simulation results. Their disadvantage is the need for augmented viscosity to assure numerical stability. The projection method adds diffusion. Model simulations showed that the is more stable than the true NC treatment of momentum advection. The reason is that the velocity field projected on  $P_1$  is smooth and without discontinuities. The disadvantage is that the momentum advection becomes a bit inconsistent with true velocity. This error may become noticeable in the energy balance (see Section 2.1.5). Here the projection method is not applied in the derivation of the energy equation and therefore the residual in the energy conservation can be attributed partly to it. In most of the simulations the error and consequently the influence of the projection method stays reasonably small.

### 2.1.2 FV discretization

The FV models are based on the finite volume discretization used in FVCOM (Chen *et al.*, 2003), but has no other links to it. They exist in three variants of time stepping. Version FVAB uses AB3-AM4 time stepping as recommended by ROMS (Shchepetkin & McWilliams, 2005) and version FVRK exploits the modified fourth-order Runge-Kutta method as in FVCOM. In addition, a semi-implicit version FVSI is tested, too. The momentum equation

is written in the flux form (Eqn.(2.2)). The algorithmic differences between these versions will be briefly sketched further.

The discretized equations are obtained by integrating the elevation and velocity equations over control volumes associated to the elevation and velocity representation. The elevation is stored at nodes and velocity is stored at elements of unstructured triangular mesh. The control volumes for velocity are the triangles themselves and for the elevation they are formed by lines connecting centroids of neighboring elements to mid-points of neighboring edges (neighbors are those elements and edges which contain the given node). More details about the discretization can be found in Chen *et al.* (2003). Although these control volumes seem ugly they can easily be taken into account by storing edges, and, for every edge, pointers to their neighboring elements. As a result, the numerical efficiency is generally not worse than that of C-grid codes.

## FVAB

The model deals with fields of horizontal velocity and elevation. First, the elevation is computed by

$$\eta^{n+1} - \eta^n = -\delta t \nabla \cdot (H\mathbf{u})^{AB3}. \quad (2.16)$$

With the elevation at the new step available, the momentum equation is updated with

$$\begin{aligned} & \mathbf{u}^{n+1} H^{n+1} - \mathbf{u}^n H^n + \delta tr |\mathbf{u}^n| \mathbf{u}^{n+1} \\ & = \delta t (-H f \mathbf{k} \times \mathbf{u} - \nabla \cdot (\mathbf{U}\mathbf{u}) + \nabla \cdot (AH_0 \nabla \mathbf{u}))^{AB3} - \delta t (gH \nabla \eta)^{AM4}. \end{aligned} \quad (2.17)$$

To compute the right hand sides at the half time step the fields used here are extrapolated using the third order Adams–Bashforth method (AB3). The half-step elevation is

$$\eta^{AB3} = (3/2 + \beta)\eta^n - (1/2 + 2\beta)\eta^{n-1} + \beta\eta^{n-2}. \quad (2.18)$$

The same rule applies for velocity. In the standard AB3,  $\beta = 5/12$ , but there are other choices which ensure better stability. The extrapolated value of the elevation is used to estimate  $H$  on the right hand side (rhs) of the continuity and momentum equation with the exception of the viscous term, where  $H$  is just replaced with  $H_0$ . The estimate of  $\nabla \eta$  on the rhs of the momentum equation is done with adding information on the already available  $\eta^{n+1}$  (this is the forth order Adams-Moulton (AM4) part of the method):

$$\eta^{AM4} = \delta \eta^{n+1} + (1 - \delta - \gamma - \varepsilon)\eta^n + \gamma \eta^{n-1} + \varepsilon \eta^{n-2}. \quad (2.19)$$

The optimal choice of coefficients recommended in ROMS are  $\beta = 0.281105$ ,  $\gamma = 0.088$ ,  $\delta = 0.614$ , and  $\varepsilon = 0.013$ . The implementation of the AB3-AM4 method requires additional storage to keep three time slices of fields, and one more set to keep the AB3 interpolated values.

### FVRK

The original time stepping in Chen *et al.* (2003) is the modified fourth order Runge-Kutta (RK4). Its implementation is as follows. I denote the rhs of the elevation equation as  $RHS_\eta$ , and of the velocity equation as  $\mathbf{RHS}_u$ . Four iterations are made within each time step:

$$\begin{aligned}\tilde{\eta}^0 &= \eta^n, \\ \tilde{\eta}^k &= \eta^n + \alpha_k \delta t RHS_\eta(\tilde{\eta}^{k-1}, \tilde{\mathbf{u}}^{k-1}), \quad k = 1, 2, 3, 4 \\ \eta^{n+1} &= \tilde{\eta}^4,\end{aligned}\tag{2.20}$$

The same rules apply to velocity. Within one time step four estimates of the rhs are performed, thus RK4 only pays off if it allows a time step which is four times larger than AB3-AM4 method. This is almost always the case, thus it is difficult to say which one should be preferred. The difference in the numerical part is that the bottom drag is used explicitly in the rhs.

### FVSI

Chen *et al.* (2003) explain that they do not use semi-implicit time stepping because their numerical implementation does not preserve symmetry of the operator acting on elevation (gradient and divergence operators are not transpose of each other). This asymmetry is not a problem because the operator remains well-behaved, and the BiCGStab algorithm of PETSc tackles that easily.

One writes

$$\mathbf{U}^{n+1} - \mathbf{U}^n = -\delta t H_0 g \nabla (\theta \eta^{n+1} + (1 - \theta) \eta^n) + \delta t \mathbf{RHS}_u^{n+1/2},\tag{2.21}$$

where

$$\mathbf{RHS}_u^{n+1/2} = (-H f \mathbf{k} \times \mathbf{u} - \nabla \cdot (\mathbf{u} \mathbf{U}))|_{AB} - r |\mathbf{u}^n| \mathbf{u}^n + \nabla \cdot (A H \nabla \mathbf{u}^n).\tag{2.22}$$

Subscript AB implies AB2 estimate (shifted for stability), and dissipative terms are taken from the previous time step. They can be AB interpolated, too. Although this is not recommended, it seldom leads to difficulties. The elevation equation is discretized as

$$\frac{\eta^{n+1} - \eta^n}{\delta t} = -\alpha \nabla \cdot \mathbf{U}^{n+1} - (1 - \alpha) \nabla \cdot \mathbf{U}^n.\tag{2.23}$$

Expressing  $\mathbf{U}^{n+1}$  from the previous equation and substituting it into this equation one gets an equation for  $\eta^{n+1}$

$$\frac{\eta^{n+1}}{\delta t} - \alpha \theta g \delta t \nabla \cdot (H_0 \nabla \eta^{n+1}) = \frac{\eta^n}{\delta t} - \nabla \cdot (\mathbf{U}^n + \alpha \delta t \mathbf{RHS}_u^{n+1/2}) + \alpha (1 - \theta) g \delta t \nabla \cdot H_0 \nabla \eta^n.\tag{2.24}$$

Solving this equation and substituting the result in the momentum equation provides the velocity for the new time step.

### 2.1.3 (Open) boundary conditions

Denoting  $\partial\Omega$  the boundary of the mesh, it is split into a solid part,  $\partial\Omega_1$ , and an open part,  $\partial\Omega_2$ .  $\mathbf{n}$  is the normal to  $\partial\Omega$  and  $\mathbf{u}_n = \mathbf{u} \cdot \mathbf{n}$  is the normal velocity. For the closed boundary there are two options, either the normal velocity is zero (together with no tangent stress requirement),  $(\mathbf{u} \cdot \mathbf{n})|_{\partial\Omega_1} = 0$ , i.e. the so called free-slip condition, or the velocity is zero,  $\mathbf{u} = 0$ , i.e. also known as no-slip condition.

To find boundary conditions that guarantee well posedness and proper information exchange at the open boundaries, it is worthwhile to recall the classification of the equations into hyperbolic, parabolic or elliptic equations. The solution of hyperbolic equations (like e.g. the wave equations) have propagating features, while parabolic solutions (e.g. of a diffusion equation) are of the form that an initial disturbance is smoothed while spreading (see, e.g., Anderson, 1995). The shallow water equations are a mixture between parabolic and hyperbolic equations - they belong to the set of incompletely parabolic systems (see, e.g., Gustafsson & Sundström, 1978). For the definition of an incomplete parabolic system I need the shallow water equations (Eqn.(2.2) and Eqn.(2.3)) in the general form,

$$\frac{\partial w}{\partial t} = \sum_{j,k} B^{(jk)} \frac{\partial^2 w}{\partial x_j \partial x_k} + \sum_j A^{(j)} \frac{\partial w}{\partial x_j} + Cw + F, \quad (2.25)$$

where  $w = (u, v, \eta)^T$  is the vector containing velocities in east resp. north direction and the elevation.  $x_1 = x$ ,  $x_2 = y$  are the West-East resp. the South-North direction and the matrices are

$$B^{(11)} = B^{(22)} = \begin{pmatrix} A & 0 & 0 \\ 0 & A & 0 \\ 0 & 0 & 0 \end{pmatrix}, B^{(12)} = B^{(21)} = \begin{pmatrix} 0 & 0 & 0 \\ 0 & 0 & 0 \\ 0 & 0 & 0 \end{pmatrix}, \quad (2.26)$$

$$A^{(1)} = \begin{pmatrix} -u & 0 & -g \\ 0 & -u & 0 \\ -(\eta + H_0) & 0 & -u \end{pmatrix}, A^{(2)} = \begin{pmatrix} -v & 0 & 0 \\ 0 & -v & -g \\ 0 & -(\eta + H_0) & -v \end{pmatrix}, \quad (2.27)$$

$$C = \begin{pmatrix} -rH^{-1}|\mathbf{u}| & -f & 0 \\ f & -rH^{-1}|\mathbf{u}| & 0 \\ \eta \frac{\partial H_0}{\partial x} & \eta \frac{\partial H_0}{\partial y} & 0 \end{pmatrix}, \quad (2.28)$$

where  $A$  is the viscosity coefficient and the other variables are used as introduced at the beginning of Section 2.1. In following considerations  $F$  is zero, but could also be set to the tidal potential as it is given in Eqn.(2.37). If the  $B^{(jk)}$  are rank deficit and the transformation of  $B^{(jk)}$  into a block matrix

$$B^{(jk)} = \begin{pmatrix} B_{11}^{(jk)} & 0 \\ 0 & 0 \end{pmatrix},$$

with  $w = (w^I w^{II})$  given by a parabolic subsystem

$$\frac{\partial w^I}{\partial t} = \sum_{j,k} B_{II}^{(jk)} \frac{\partial^2 w^I}{\partial x_j \partial x_k}$$

and a strictly hyperbolic subsystem

$$\frac{\partial w^{II}}{\partial t} = \sum_j A_{22}^{(j)} \frac{\partial w^{II}}{\partial x_j},$$

then the system is incompletely parabolic (Gustafsson & Sundström, 1978). This is obviously the case for the shallow water equations. By multiplying it with  $R := Q^T Q$ , where  $Q$  is defined as

$$Q = \begin{pmatrix} \sqrt{\frac{H_0 + \eta}{g}} & 0 & 0 \\ 0 & \sqrt{\frac{H_0 + \eta}{g}} & 0 \\ 0 & 0 & 1 \end{pmatrix}, \quad (2.29)$$

Eqn.(2.25) is symmetrized.

A classical way to prove that the boundary conditions give a well-posed system, is to give an energy norm by integrating over the domain, i.e.,

$$\begin{aligned} \frac{\partial}{\partial t} \int_{\Omega} w^T Q^T Q w &= -2 \int_{\Omega} w_x^T R B^{(11)} w_x d\omega - 2 \int_{\Omega} w_y^T R B^{(22)} w_y d\omega \\ &+ \int_{\partial\Omega} 2w^T R B^{(11)} n_1 w_x + 2w^T R B^{(22)} n_2 w_y ds \\ &+ \int_{\partial\Omega} w^T R A^{(1)} n_1 w + w^T R A^{(2)} n_2 w ds \\ &+ 2 \int_{\Omega} w^T R C w d\omega, \end{aligned} \quad (2.30)$$

where  $w_x$  resp.  $w_y$  denote the derivative of  $w$  in  $x$  resp.  $y$  direction and  $n_1$  resp.  $n_2$  denote the normal in  $x$  resp.  $y$  direction.

The first two terms on the rhs are always negative. As expected, the viscosity terms are energy sinks. Well-posedness roughly means that a the system of equations has a unique solution and that the solution is bounded by some growth rate multiplied with some norm of the input data (Nordström, 1995). For a sufficiently fine mesh the growth rate will only depend on time step size and is, therefore, strongly stable. The boundary integral in Eqn.(2.30) shows that a decent choice of boundary conditions can give an upper bound for the energy and prove the well-posedness of the system. I will not go into further details of the analysis, as it has already been done by a number of publications (see, e.g., Strikwerda, 1977; Oliger & Sundström, 1978; Gustafsson & Sundström, 1978; Halpern, 1991) and will just want to point out some results.

As the viscosity terms are very small, this parabolic part of the system is

often neglected for the definition of open boundary conditions. To find them for the hyperbolic system, the method of characteristics is very useful. It ensures stability while minimizing the reflection of waves at the open boundaries. In Eqn.(2.30) the open boundary terms with  $A^{(1)}$  and  $A^{(2)}$  have to be bounded. Therefore the eigenvalues and eigenvectors of  $A^{(1)}n_1 + A^{(2)}n_2$  are computed:

$$\lambda_1 = -\mathbf{u} \cdot \mathbf{n}, \quad \lambda_2 = -(\mathbf{u} \cdot \mathbf{n} + c), \quad \lambda_3 = -(\mathbf{u} \cdot \mathbf{n} - c),$$

$$\mathbf{e}_1 = \begin{pmatrix} n_2 \\ -n_1 \\ 0 \end{pmatrix}, \quad \mathbf{e}_2 = \begin{pmatrix} n_1 \\ n_2 \\ \frac{c}{\eta+H_0} \end{pmatrix}, \quad \mathbf{e}_3 = \begin{pmatrix} n_1 \\ n_2 \\ -\frac{c}{\eta+H_0} \end{pmatrix},$$

where  $c = \sqrt{g(\eta + H_0)}$ . But since at the open boundary almost everywhere  $\eta \ll H_0$  the  $\eta$  in the eigenvectors can later be neglected and  $c$  is approximately  $\sqrt{gH_0}$ . The characteristic variables (or Riemann invariants) are then the scalar product between  $w$  and the eigenvectors, i.e.,

$$R_1 = \mathbf{u} \cdot \mathbf{t}, \quad R_2 = \mathbf{u} \cdot \mathbf{n} + \frac{c}{\eta + H_0}\eta, \quad R_3 = \mathbf{u} \cdot \mathbf{n} - \frac{c}{\eta + H_0}\eta$$

where  $\mathbf{t}$  is the tangential to the open boundary.  $R_i$  are called characteristic variables, because they are constant along the curve  $dn/dt = -\lambda_i$ ,  $d\tau/dt = 0$  ( $n$  denotes the variable in normal direction,  $\tau$  is the variable in tangential direction). This means that  $R_i$  has to have the same value inside and outside of our domain. Therefore, the direction in which the information is transported, needs to be known and boundary conditions for each incoming characteristic has to be prescribed. To distinguish between incoming and outgoing characteristic I introduce the Froude number

$$Fr = \frac{\sqrt{u^2 + v^2}}{c}.$$

It classifies the flow into subcritical  $Fr < 1$ , critical  $Fr = 1$  and supercritical  $Fr > 1$ . At the open boundaries in the North Sea there is always subcritical flow. For outflow ( $\mathbf{u} \cdot \mathbf{n} > 0$ ) it follows, that  $\lambda_1 < 0$ ,  $\lambda_2 < 0$  and  $\lambda_3 > 0$ . Accordingly I need a condition for  $R_3$  to get an upper bound for the energy norm (Eqn.(2.30)). For inflow ( $\mathbf{u} \cdot \mathbf{n} < 0$ ) I have  $\lambda_1 > 0$ ,  $\lambda_2 < 0$  and  $\lambda_3 > 0$  and, therefore, two conditions - one for  $R_1$  and one for  $R_3$  - are needed.

In practice the necessary information on the open boundary is sometimes unavailable. The velocity is often unknown or prone to error. So it is common practice to either prescribe the sea level oscillations  $\eta|_{\partial\Omega_2}$  (the so called clamped boundary condition) or to impose the radiation boundary condition  $\mathbf{u}_n = \mathbf{u} \cdot \mathbf{n} = \sqrt{\frac{g}{H_0}}\eta$ , which provides a free passage of linear waves (in the absence of Coriolis effect). The first one often brings less accurate results

(Flather, 1976), but is sometimes the only choice if no velocity data is available. Accuracy of the reduced boundary-value formulation when only the sea level is assigned at the open boundary, was considered by Androsov *et al.* (1995). Some of combinations of the characteristic variables, like for example the one resulting in  $u_n$  and  $\eta$ , give an ill-posed problem (Oliger & Sundström, 1978). Therefore  $R_3$  is prescribed at the open boundary (also known as the Flather condition (Flather, 1976)) whenever the velocity data is reliable. Otherwise the clamped boundary condition are used.

Since the viscous part is very small, most of the shallow water models take only the hyperbolic part of the open boundary condition into account. If I would use the viscosity, the systems were incompletely parabolic and I needed three conditions for inflow and two conditions for outflow. They are discussed in Gustafsson & Sundström (1978) or given in Blayo & Debreu (2005) or Androsov *et al.* (1995). I do not think, that they will bring major improvement and, therefore, leave it for later studies.

Another method is to treat the open boundary, for example, with the relaxation method (Marchesiello *et al.*, 2001). An additional term is put on the right hand side of the momentum equation. It relaxes the solution from the interior to the exterior solution and helps to avoid wave reflection, if the numerical result differs from the exterior data. A nice review of open boundary conditions has been given in Chassignet & Verron (2006).

Later in Chapter 3 and 4 I am going to introduce an adjoint model of the NCLF model and use it to optimize the open boundary conditions. In this respect the model is able to adjust the boundary values to be consistent with the interior solution.

### 2.1.4 Tidal Potential

In this section I explain, how the model is forced by the tidal potential. In Section 2.1.3 the mathematical and numerical background was given on how to simulate waves, which are entering through the open boundaries of our domain. These waves are the main contribution for tides in the North Sea and only a relative small portion comes directly from the tidal potential. This is in contrary to closed basins such as lakes or almost closed sea basins, where the effect of the entering wave is small and the tidal potential can be relatively important.

Potentials induced by gravitational forces of the Sun and the Moon are called primary tidal forces. These forces move water and Earth masses and change the gravitational potential of the Earth. The additional layers of water increase the potential by their self attraction and deform the ocean bottom. Thus, the effects are called secondary forces.

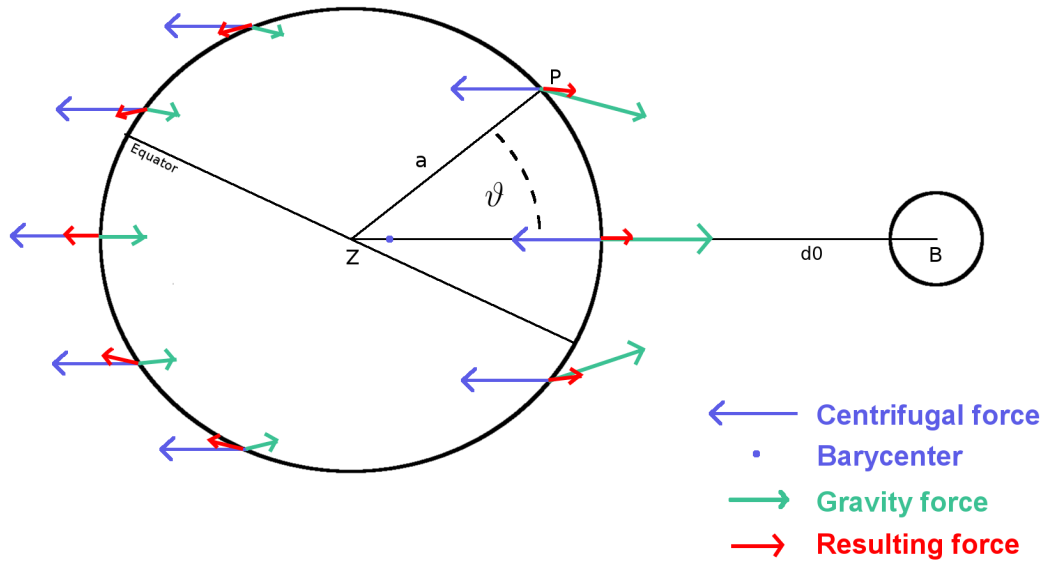


Figure 2.2: Resulting force of centrifugal and gravitational force; coordinates for the potential

### Primary tidal forces

The theoretical basis for the explanation of tidal elevations existed already in the 17th century by the theory of Newton's gravitational law and the equilibrium theory of tides (Newton, 1687). Earth and Moon (or the Sun) rotate around their barycenter. Centrifugal and gravitational force add up to a resulting force sketched in Fig. 2.2. At a point P on the surface of the Earth (see Fig. 2.2) this force can be expressed with a potential and expanded in Legendre polynomials (for details, see, e.g., Defant, 1961; Torge, 2003),

$$\Phi(\vec{a}, \vec{d}_0) = \sum_{n=2}^{\infty} \Phi^{(n)}(\vec{a}, \vec{d}_0), \quad (2.31)$$

$$\Phi^{(n)}(\vec{a}, \vec{d}_0) : = \frac{\gamma M}{d_0} \frac{a^n}{d_0^n} P_n(\cos \vartheta) \quad (2.32)$$

where  $\gamma \approx 6.67 \cdot 10^{-11} \text{ N kg}^{-2} \text{ m}^2$  is the gravitational constant,  $M$  the mass of the Moon,  $a$  the distance between P and the geographical center of the Earth. The origin of the ground fixed coordinate system is denoted by Z,  $d_0$  the distance between Z and the center of the celestial body B,  $\vartheta$  the angle between  $\vec{a}$  and  $\vec{d}_0$  (= the geocentric zenith angle) (see Fig. 2.2).

Since in ocean models the point P uses geographical coordinates in longitude and latitude  $(\lambda, \theta)$ , the tidal potential has to be written in terms of them. The following relation between the zenith angle  $\vartheta$  and the geographical co-

ordinates  $(\lambda, \theta)$  is valid (see, e.g., Bronstein *et al.*, 2001)

$$\cos \vartheta = \sin \theta \sin \delta + \cos \theta \cos \delta \cos t_M = \frac{\vec{a}}{a} \cdot \frac{\vec{d}_0}{d_0}, \quad (2.33)$$

where  $\delta$  is the declination (= latitude of the celestial body) and  $t_M$  the hour angle of the astronomical body (=  $\lambda$  minus longitude  $\tau_1$  of celestial body B). Trigonometric addition theorems give us the right equality in Eqn.(2.33). By using this last relationship I rewrite  $P_n(\cos \vartheta)$  in Eqn.(2.32) in terms of an orthonormal basis system with the help of the addition theorem for spherical harmonics (see, e.g., Freedon *et al.*, 1998). A suitable basis set are the normalized Legendre surface harmonics (see the appendix or, e.g., Moritz, 1980). Finally the following expression is obtained

$$\Phi(\vec{a}, \vec{d}_0) = \frac{\gamma M}{d_0} \sum_{n=2}^{\infty} \frac{a^n}{d_0^n} \frac{1}{2n+1} \sum_{m=0}^n \bar{P}_{nm}(\sin \theta) \bar{P}_{nm}(\sin \delta) \cos mt_M,$$

where  $\bar{P}_{nm}$  are the normalized Legendre functions (for further details, see, e.g., Wenzel, 1997).

The next step is the decomposition of the astronomical tide-generating potential into harmonic partial tides following the work of Doodson (1921). But first I start with a look at the form of the tidal potential of second degree. By introducing of the Doodson's constant

$$G(a) = \frac{3}{4} \frac{\gamma M a^2}{c^3},$$

where  $c$  is the mean lunar distance, the tidal potential of second degree has the following form

$$\begin{aligned} \Phi^{(2)}(\vec{a}, \vec{d}_0) = G(a) \frac{c^3}{d_0^3} & \left( 3 \left( \frac{1}{3} - \sin^2 \theta \right) \left( \frac{1}{3} - \sin^2 \delta \right) \right. \\ & \left. + \sin 2\theta \sin 2\delta \cos t_M + \cos^2 \theta \cos^2 \delta \cos 2t_M \right). \end{aligned}$$

The time dependency of the tidal potential is hidden in the variables  $c/d_0$ ,  $\delta$  and  $t_M$ . The first term does not depend on the hour angle  $t_M$ , so its time variation is given by the declination  $\delta$ . For the Moon the period of the declination is one month. The first term is, therefore, referred to as the long-period tide. The meridional dependency is in the hour angle  $t_M$  and since the first term does not depend on it, the long-period part has only zonal variations.

The second term has a daily period and it is called the diurnal tide. It vanishes at the equator. The last term has  $2t_M$  in the cosine and contributes therefore to the semi-diurnal tide. It is maximal at the equator and zero at the Poles. Obviously, all terms contribute to the tidal potential in the North and Baltic Sea .

For sake of practicality the time dependent variables are developed in terms of the temporally varying astronomical arguments: mean local lunar time  $\tau$ , mean lunar longitude  $s$ , mean solar longitude  $h$ , mean longitude of lunar perigee  $p$ , mean longitude of solar perigee  $p_s$  and negative mean longitude of lunar ascending node  $N'$ . Their temporal dependency is then obtained with polynomials in Julian time  $t$  referenced to a specific starting date (see, e.g., Schwiderski, 1980; Wenzel, 1997). There are several ways to make the expansion of the tidal potential. One, including  $i_{max}$  tidal modes, is given by the following general formula (Hartmann & Wenzel, 1994, 1995a)

$$\Phi(a, \theta, \lambda, t) = \sum_{n=2}^{n_{max}} \frac{a^n}{b^n} \sum_{m=0}^n \bar{P}_{nm}(\sin \theta) \sum_{i=1}^{i_{max}} (C_i^{nm}(t) \cos(\alpha_i(t)) + S_i^{nm}(t) \sin(\alpha_i(t))),$$

where  $(a, \theta, \lambda)$  are the geographical coordinates of point P and  $b$  is the major semi-axis of the Earth's mean ellipsoid. The time dependent arguments  $\alpha_i$  and coefficients  $C_i^{nm}$  and  $S_i^{nm}$  are given by:

$$\begin{aligned} \alpha_i(t) &:= m\lambda + \sum_{j=1}^6 k_{ij} \beta_j(t), \\ C_i^{nm}(t) &:= C0_i^{nm} + t \cdot C1_i^{nm}, \\ S_i^{nm}(t) &:= S0_i^{nm} + t \cdot S1_i^{nm}, \end{aligned}$$

where  $\beta = (\tau, s, h, p, N', p_s)$ . The numbers  $k_{ij}$ ,  $C_i^{nm}$  and  $S_i^{nm}$  can be found in the tidal catalogue of Hartmann & Wenzel (1995b). Alternatively Schwiderski (1980) defined the argument  $\alpha_i$  and its coefficients  $C_i^{nm}$  and  $S_i^{nm}$  in the following way.  $S_i^{nm}$  are zero and  $C_i^{nm}$  are time independent. Furthermore,

$$\alpha_i(t) := \sigma_i t + \chi_i + m\lambda,$$

with

$$\begin{aligned} \sigma_i &:= m \frac{\partial \lambda}{\partial t} + \sum_{j=1}^6 k_{ij} \frac{\partial \beta_j(t)}{\partial t}, \\ \chi_i &:= \sum_{j=1}^6 k_{ij} \beta_j(t). \end{aligned}$$

It is immediately obvious that  $\frac{\partial \lambda}{\partial t} = 15^\circ/3600s = 0.72722 \cdot 10^{-4}/s$ . The temporal changes of the astronomical arguments,  $\frac{\partial \beta_j(t)}{\partial t}$ , are approximately constant and printed in Simon *et al.* (1994). Thus, the only temporal dependency lies in  $\beta_j(t)$ , which can be developed as polynomials up to second or third degree of time. I assume here that  $\frac{a}{b} \approx 1$  and obtain constants  $K_i$  which do not depend on time and position on the Earth. Finally, the potential is divided by the gravitational acceleration  $g$  and the displacement due to the

tidal potential of second degree is obtained:

$$\frac{\Phi_i^{(2)}(\theta, \lambda, t)}{g} = K_i \cos^2 \theta \cos(\sigma_i t + \chi_i + 2\lambda) \quad (2.34)$$

$$i = 1, \dots, 4 \quad (\text{semidiurnal})$$

$$\frac{\Phi_i^{(2)}(\theta, \lambda, t)}{g} = K_i \sin 2\theta \cos(\sigma_i t + \chi_i + \lambda) \quad (2.35)$$

$$i = 4, \dots, 8 \quad (\text{diurnal})$$

$$\frac{\Phi_i^{(2)}(\theta, \lambda, t)}{g} = K_i (3 \cos^2 \theta - 2) \cos(\sigma_i t + \chi_i) \quad (2.36)$$

$$i = 9, \dots, 11 \quad (\text{long - period})$$

Both, the constants of the major tidal modes and the polynomial approximation of the astronomical arguments, are given in Schwiderski (1980). I will use this approximation with the first 11 leading modes of the tidal potential:  $M_2$  principal lunar,  $S_2$  principal solar,  $N_2$  elliptical lunar,  $K_2$  declination luni-solar,  $K_1$  declination luni-solar,  $O_1$  principal lunar,  $P_1$  principal solar,  $Q_1$  elliptical lunar,  $Mf$  fortnightly lunar,  $Mm$  monthly lunar,  $Ssa$  semiannual solar.

### Secondary tidal forces - LSA

In this section I discuss the tidal movement of the solid Earth and how the potential field changes due to the tidal load. On the one hand the displacement of masses by primary tidal forces alters the potential. On the other hand this additional load deforms the solid Earth. To correctly model these interactions a profound knowledge of the Earth density distribution and its elastic and anelastic properties would be needed. As measurements are difficult, Earth models like the Gutenberg-Bullen-Earthmodel (Farrell, 1972) or the PREM (Preliminary Reference Earth Model, Dziewonski & Anderson (1981)) compute so called Love numbers (Love, 1909; Wahr, 1981). These are factors for the spherical harmonic coefficients of the tidal potential (or, to be precise, the potential of n-th degree ( $\Phi^{(n)}$ )).

As the Earth reacts elastic on the potential forces and the bottom moves by  $h_n \Phi^{(n)}/g$ , the effective potential is equivalently reduced to  $(1 - h_n) \Phi^{(n)}$ . For  $n = 2$  this factor is  $h_2 \approx 0.612$  (Farrell, 1972). A fully unelastic Earth would mean  $h_n = 0$ . The mass is redistributed within the Earth and is responsible for an additional potential approximated by  $k_n \Phi^{(n)}$ . So the effective, total tidal potential for the n-th degree is  $(1 - h_n + k_n) \Phi^{(n)}$ . For  $n = 2$  the self-attraction number is  $k_2 \approx 0.31$  (Farrell, 1972).

In the special case of a spherical, homogeneous and incompressible Earth the following relationship between the mean elasticity of the Earth and the

Love numbers holds true (Groten, 1984):

$$k_n = \frac{3}{2n+1} h_n,$$

$$h_n = \frac{2n+1}{2(n-1)} \left/ \left( 1 + \frac{(2n^2 + 4n + 3)\mu}{n\rho_e g a} \right) \right.,$$

where  $\mu$  is the (average) modulus of rigidity,  $a$  the mean radius of the Earth and  $\rho_e$  is the mean density of the solid Earth. These numbers are only very rough approximations and more realistic Earth models (such as Farrell (1972), Dziewonski & Anderson (1981) or Wahr (1981)) give better values for the Love numbers.  $h_n$  and  $k_n$  are also called the non-loading Love numbers, since they result from the visco-elastic deformation of the Earth and depend on the whole structure of the Earth.

Now I have a look at the effects of tidal ocean mass redistribution. Considering  $H_0$  as the unperturbed water depth to our reference level and  $\eta$  as the variation of the water level to the reference level, the total depth  $H$  is given by  $H = H_0 + \eta$ . From the Earth tide the bottom moves by  $h_n \Phi^{(n)}/g$ , but the total water depth  $H_0$  is maintained and the whole water column is raised or lowered. But  $\eta$  changes according to the tidal potential. The tidal water bulge also deforms the ocean bottom. If  $\eta$  is positive, the bottom is lowered due to the water mass weight. I assume that  $\eta$  (depending on latitude and longitude  $(\theta, \lambda)$ ) is given on a unit sphere (zero on land). By developing it with Legendre surface harmonics (see Appendix for a definition of these functions) the following is obtained

$$\eta(\theta, \lambda) = \sum_{k=0}^{\infty} \eta_k(\theta, \lambda)$$

with

$$\eta_k(\theta, \lambda) = \sum_{l=0}^k \frac{2k+1}{\kappa_{kl}} \int_{\partial S} \eta(\theta', \lambda') P_{kl}(\sin \theta) P_{kl}(\sin \theta') \cos l(\lambda' - \lambda) d\theta' d\lambda'.$$

If one considers the additional layer of water on a homogeneous, spherical Earth, the following expression for its potential has been obtain by Zahel (1978) or Smirnow (1982)

$$\tilde{\Phi}(\theta, \lambda) = g \sum_{k=0}^{\infty} \alpha_k \eta_k(\theta, \lambda) \quad \text{with} \quad \alpha_k := \frac{3}{2k+1} \frac{\rho}{\rho_e},$$

where  $\rho$  is the mean density of sea water. Again the bottom movement is proportional to the potential of the additional water mass. The tidal potential will change by  $g h'_k \alpha_k \eta_k$ , where  $h'_k$  is negative because the bottom is lowered. On response of the bottom deformation the mass redistribution within the Earth gives a change in the potential of  $g k'_k \alpha_k \eta_k$ , where  $k'_k$  is again negative.

$h'_k$  and  $k'_k$  denote the loading Love-numbers. Thus, the vertical displacement of the sea-bottom  $\delta$  and the total potential are given by

$$\delta = \frac{h_n \Phi^{(n)}}{g} + \sum_{k=0}^{\infty} h'_k \alpha_k \eta_k,$$

$$\Phi_{LSA}^{(n)} : = (1 + k_n) \Phi^{(n)} + \sum_{k=0}^{\infty} g(1 + k'_k) \alpha_k \eta_k.$$

Hence the complete tidal potential of n-th degree is given by the following elevation (Zahel, 1978)

$$\frac{\Phi_{LSA}^{(n)}}{g} - \delta = \frac{(1 + k_n - h_n) \Phi^{(n)}}{g} + \sum_{k=0}^{\infty} (1 + k'_k - h'_k) \alpha_k \eta_k$$

Some values for the loading Love-numbers are, for example, given in Farrell (1972).

### Tidal equations

Coming to back to the governing equations Eqn.(2.1) and Eqn.(2.4) the tidal potential is introduced as a force on the rhs of the momentum equations

$$\frac{\partial \mathbf{u}}{\partial t} + f \mathbf{k} \times \mathbf{u} + g \nabla \eta + (\mathbf{u} \nabla) \mathbf{u} = H^{-1} \nabla (A H \nabla \mathbf{u}) - r H^{-1} |\mathbf{u}| \mathbf{u} + g \nabla \left( \frac{\Phi_{LSA}^{(n)}}{g} - \delta \right). \quad (2.37)$$

Actually, in the current implementation only the tidal potential of second degree is used (see Schwiderski, 1980). The influence of the Earth tide is implemented straight forward by multiplying the term for the tidal potential (Eqn.(2.34)-(2.36)) by  $1 + k_2 - h_2$ , where  $k_2$  and  $h_2$  have the values given in Farrell (1972). The calculation of the ocean mass distribution is not possible, as the model only has a regional domain and the computation of spherical harmonic coefficients would need a global tidal elevation. But since the influence of the Earth tide and the tidal potential in the North and Baltic Sea is already very small, I do not expect major errors in the computation of the velocity by neglecting the influence of the water masses on the tidal potential. Future work should use tidal elevations from altimetry/satellite data or global tidal models to include the loading effects.

Note that only the tidal potential on the rhs of the momentum equation (Eqn.(2.37)) includes the bottom movement  $\delta$ . The other terms of the momentum equation are not affected, since there are no feedbacks of the bottom movement on the total water depth. In the North and Baltic Sea it is sufficient to apply a constant tidal potential in a first approximation. Therefore, no pressure gradient can result, and there are also no changes in the continuity equation. So the continuity equation still writes as

$$\frac{\partial}{\partial t} \eta + \nabla(\eta + H_0) \mathbf{u} = 0.$$

### 2.1.5 Energy balance

In some model simulations the evolution of the energy during the model integration is going to be analysed. The energy input and dissipation into the system give important insights in the model performance. Additionally, these values describe energy fluxes from the open ocean to the continental shelf. Further, the energy equilibrium indicates, whether the transient solutions have been damped away successfully.

For this purpose the equations describing the energy fluxes are set up. Conservation of mass and momentum implies that the energy is in balance in the system and, therefore, the energy equations are indirectly maintained by the model as well.

I consider the momentum and the continuity equation in their non-conserving form (see Eqn.(2.1) and Eqn.(2.4)) with the tidal potential as additional driving force at the right hand side. Then the momentum equations are multiplied with the total depth  $H$  times velocity  $(u, v)$  resp. the continuity equation with the gravitational constant  $g$  times sea surface elevation  $\eta$ .

The viscous term is treated at the end of this section. Therefore, it is not written explicitly here, but instead they are represented by  $\text{Visc}_1, \text{Visc}_2$  resp.  $\text{Visc}$ . I obtain

$$\begin{aligned} Hu \frac{\partial u}{\partial t} - Hufv + gHu \frac{\partial \eta}{\partial x} + Hu \left( u \frac{\partial}{\partial x} + v \frac{\partial}{\partial y} \right) u - \text{Visc}_1 + ru|\mathbf{u}|u &= Hgu \frac{\partial \eta_p}{\partial x}, \\ Hv \frac{\partial v}{\partial t} + Hvf u + gHv \frac{\partial \eta}{\partial y} + Hv \left( u \frac{\partial}{\partial x} + v \frac{\partial}{\partial y} \right) v - \text{Visc}_2 + rv|\mathbf{u}|v &= Hgv \frac{\partial \eta_p}{\partial y}, \\ g\eta \frac{\partial \eta}{\partial t} + g\eta \frac{\partial Hu}{\partial x} + g\eta \frac{\partial Hv}{\partial y} &= 0, \end{aligned}$$

Summing the two momentum equations (notice that the Coriolis terms cancel out) and integrating over the domain leads to

$$\begin{aligned} \int_{\Omega} \left( Hu \frac{\partial u}{\partial t} + Hv \frac{\partial v}{\partial t} + gH(\mathbf{u} \cdot \nabla)\eta + Hu(\mathbf{u} \cdot \nabla)u + Hv(\mathbf{u} \cdot \nabla)v - \text{Visc} \right. \\ \left. + ru|\mathbf{u}|u + rv|\mathbf{u}|v \right) d\omega = \int_{\Omega} Hg(\mathbf{u} \cdot \nabla)\eta_p d\omega. \end{aligned} \quad (2.38)$$

Analogously the continuity equation gives the following

$$\int_{\Omega} \left( g\eta \frac{\partial \eta}{\partial t} - H(\mathbf{u} \cdot \nabla)g\eta + \nabla \cdot (H\mathbf{u}g\eta) \right) d\omega = 0. \quad (2.39)$$

The fourth and the fifth integrand in Eqn.(2.38) are part of the advective term of the equations and can be rewritten as

$$Hu(\mathbf{u} \cdot \nabla)u + Hv(\mathbf{u} \cdot \nabla)v = \frac{u^2 + v^2}{2} \frac{\partial \eta}{\partial t} + \nabla \cdot \left( \mathbf{u} H \frac{u^2 + v^2}{2} \right) \quad (2.40)$$

Summing up Eqn.(2.38) and Eqn.(2.39) and using Eqn.(2.40) the following equation is obtained:

$$\begin{aligned} & \int_{\Omega} \frac{\partial}{\partial t} \frac{g\eta^2}{2} d\omega && \text{temporal change potential energy} \\ & + \int_{\Omega} \frac{\partial}{\partial t} H \frac{u^2 + v^2}{2} d\omega && \text{temporal change kinetic energy} \\ & + \int_{\Omega} \nabla \cdot (H\mathbf{u}g\eta) d\omega && \text{transport potential energy} \\ & + \int_{\Omega} \nabla \cdot \left( \mathbf{u} H \frac{u^2 + v^2}{2} \right) d\omega && \text{transport kinetic energy} \\ & + \int_{\Omega} r(u|\mathbf{u}|u + v|\mathbf{u}|v) d\omega && \text{energy sink bottom friction} \\ & - \int_{\Omega} \text{Visc} d\omega && \text{viscous energy sink} \\ & = \int_{\Omega} Hg(\mathbf{u} \cdot \nabla)\eta_p d\omega && \text{energy source potential} \end{aligned}$$

The first two terms describe the temporal rate of change of potential resp. kinetic energy, when they are multiplied by the density of sea water. The third and the fourth term can be replaced by boundary integrals. As the normal part of the velocity is zero at closed boundaries, only the contribution of the open boundary remains describing the energy fluxes of potential and kinetic energy into or out of the domain. The fifth and the sixth term are the energy dissipation terms. On the rhs of the equation is the tidal potential as a forcing term.

The energy equation above result from the continuous governing equations. The question is how to translate them into the discrete spaces. Elevation is given each time step by a sum of test functions (as explained in Section 2.1.1), i.e.  $\eta = \sum_k \eta_k \Phi_k$ , and the velocities  $u, v$  are presented analogously. As velocity and elevation are temporally discrete, the energy equation is rewritten to account for it.

I illustrate here the procedure for semi-implicit time stepping, which solve Eqn.(2.5) and Eqn.(2.6). In the current implementation partial integration is applied to the second term of the continuity equation and therefore I also do this after the multiplication with  $g\bar{\eta}$ , where  $\bar{\eta} := \theta\eta^{n+1} + (1 - \theta)\eta^n$  and  $\bar{\mathbf{u}} := \alpha\mathbf{u}^{n+1} + (1 - \alpha)\mathbf{u}^n$ . I obtain

$$\int_{\Omega} \left( g\bar{\eta} \frac{\eta^{n+1} - \eta^n}{\delta t} - gH_0\bar{\mathbf{u}} \cdot \nabla\bar{\eta} - g\eta^n\mathbf{u}^n \cdot \nabla\bar{\eta} + \nabla \cdot (g\bar{\eta}(H_0\bar{\mathbf{u}} + \eta^n\mathbf{u}^n)) \right) d\omega = 0$$

The forth term accounts for the transfer of potential energy through the open

boundary. The equation can analogously be rewritten as

$$\int_{\Omega} \left( g\bar{\eta} \frac{(\eta^{n+1} - \eta^n)}{\delta t} - H^n (\bar{\mathbf{u}} \cdot \nabla) g\bar{\eta} + \alpha g \eta^n (\mathbf{u}^{n+1} - \mathbf{u}^n) \cdot \nabla \bar{\eta} + \nabla \cdot (g\bar{\eta} (H_0 \bar{\mathbf{u}} + \eta^n \mathbf{u}^n)) \right) d\omega = 0$$

The momentum equations are multiplied by  $H^n \bar{u}$  resp.  $H^n \bar{v}$  and summed. Strictly speaking the Coriolis term only vanishes, if  $\alpha$  is equal to  $\beta$ . This needs not to be the case, but will not lead to major error. The momentum equations give

$$\int_{\Omega} \left( H^n \bar{u} \frac{u^{n+1} - u^n}{\delta t} + H^n \bar{v} \frac{v^{n+1} - v^n}{\delta t} + g H^n (\bar{\mathbf{u}} \cdot \nabla) \bar{\eta} + H^n \bar{u} (\mathbf{u}^n \cdot \nabla) u^n + H^n \bar{v} (\mathbf{u}^n \cdot \nabla) v^n - \text{Visc} + r\bar{u} |\mathbf{u}^n| u^n + r\bar{v} |\mathbf{u}^n| v^n \right) d\omega = \int_{\Omega} H^n g (\bar{\mathbf{u}} \cdot \nabla) \eta_p^n d\omega.$$

Because of the time discretization the advection takes the following form

$$\begin{aligned} & H^n \bar{u} (\mathbf{u}^n \cdot \nabla) u^n + H^n \bar{v} (\mathbf{u}^n \cdot \nabla) v^n \\ &= H^n (\mathbf{u}^n \cdot \nabla) \left( \frac{\bar{u} u^n}{2} + \frac{\bar{v} v^n}{2} \right) + \frac{1}{2} H^n (\mathbf{u}^n \cdot (\bar{u} \nabla u^n + \bar{v} \nabla v^n - u^n \nabla \bar{u} - v^n \nabla \bar{v})) \\ &= \nabla \cdot \left( \mathbf{u}^n H^n \left( \frac{\bar{u} u^n}{2} + \frac{\bar{v} v^n}{2} \right) \right) - \left( \frac{\bar{u} u^n}{2} + \frac{\bar{v} v^n}{2} \right) \nabla \cdot \mathbf{u}^n H^n \\ &\quad + \frac{1}{2} H^n \alpha (\mathbf{u}^n \cdot (u^{n+1} \nabla u^n - u^n \nabla u^{n+1} + v^{n+1} \nabla v^n - v^n \nabla v^{n+1})) \\ &= \nabla \cdot \left( \mathbf{u}^n H^n \left( \frac{\bar{u} u^n}{2} + \frac{\bar{v} v^n}{2} \right) \right) \\ &\quad - \left( \frac{\bar{u} u^n}{2} + \frac{\bar{v} v^n}{2} \right) \left( -\frac{(\eta^{n+1} - \eta^n)}{\delta t} - \alpha \nabla \cdot (H_0 \mathbf{u}^{n+1} - H_0 \mathbf{u}^n) \right) \\ &\quad + \frac{1}{2} H^n \alpha (\mathbf{u}^n \cdot (u^{n+1} \nabla u^n - u^n \nabla u^{n+1} + v^{n+1} \nabla v^n - v^n \nabla v^{n+1})), \end{aligned}$$

where the discrete continuity equation is used for the last equality. Combining this result with the expressions obtained from the discrete continuity and momentum equation, the following energy sources, sinks and transfers can

be written down analogously to the continuous case:

$$\begin{aligned}
& \int_{\Omega} g\bar{\eta} \frac{\eta^{n+1} - \eta^n}{\delta t} d\omega \\
& + \int_{\Omega} \left( H^n \bar{u} \frac{u^{n+1} - u^n}{\delta t} + H^n \bar{v} \frac{v^{n+1} - v^n}{\delta t} + \left( \frac{\bar{u}u^n}{2} + \frac{\bar{v}v^n}{2} \right) \frac{\eta^{n+1} - \eta^n}{\delta t} \right) d\omega \\
& + \int_{\Omega} \nabla \cdot (g\bar{\eta}(H_0\bar{\mathbf{u}} + \eta^n\mathbf{u}^n)) d\omega \\
& + \int_{\Omega} \nabla \cdot \left( \mathbf{u}^n H^n \left( \frac{\bar{u}u^n}{2} + \frac{\bar{v}v^n}{2} \right) \right) d\omega \\
& + \int_{\Omega} r\bar{u}|\mathbf{u}^n|u^n + r\bar{v}|\mathbf{u}^n|v^n d\omega \\
& - \int_{\Omega} \text{Visc} d\omega \\
& + \int_{\Omega} \alpha g \eta^n (\mathbf{u}^{n+1} - \mathbf{u}^n) \cdot \nabla \bar{\eta} d\omega \\
& + \int_{\Omega} \left( \frac{\bar{u}u^n}{2} + \frac{\bar{v}v^n}{2} \right) \alpha \nabla \cdot (H_0\mathbf{u}^{n+1} - H_0\mathbf{u}^n) d\omega \\
& + \int_{\Omega} \frac{1}{2} H^n \alpha \left( \mathbf{u}^n \cdot (u^{n+1} \nabla u^n - u^n \nabla u^{n+1} + v^{n+1} \nabla v^n - v^n \nabla v^{n+1}) \right) d\omega \\
& = \int_{\Omega} H^n g (\bar{\mathbf{u}} \cdot \nabla) \eta_p^n d\omega.
\end{aligned} \tag{2.41}$$

Again the first two terms are the temporal change of potential and kinetic energy. The third and the fourth refer to the transport of kinetic and potential energy through the boundaries.

Dissipation by bottom friction is given by the fifth equation. The seventh to ninth term are contributions from the temporal discretization and the definition of the kinetic energy (flux). I called them unknown1 to unknown3 in the model implementation. They disappear when the scheme becomes fully implicit. unknown1 contributes to the exchange between potential and kinetic energy. unknown2 and unknown3 may be added to the kinetic energy (flux), as they come from the advection. All unknown terms are relatively small compared with the transport, the bottom friction and the temporal change of potential and kinetic energy. But they are of comparable size compared to the viscosity term.

I am now going to evaluate the viscosity term called  $\text{Visc}$  in the upper equations. Multiplying the momentum equation with  $H^n \bar{u}$  resp.  $H^n \bar{v}$  and addition gives for the viscosity

$$\begin{aligned}
& - \int_{\Omega} \text{Visc} d\omega \\
& = - \int_{\Omega} H^n \bar{u} A (\nabla \cdot \nabla) u^n + H^n \bar{v} A (\nabla \cdot \nabla) v^n d\omega \\
& = A \int_{\Omega} \nabla (H^n \bar{u}) \cdot \nabla u^n + \nabla (H^n \bar{v}) \cdot \nabla v^n d\omega \\
& \quad - A \int_{\Omega} \nabla \cdot (H^n \bar{u} \nabla u^n) + \nabla \cdot (H^n \bar{v} \nabla v^n) d\omega \\
& = A \int_{\Omega} \nabla (H^n \bar{u}) \cdot \nabla u^n + \nabla (H^n \bar{v}) \cdot \nabla v^n d\omega \\
& \quad - A \int_{\partial\Omega} H^n \bar{u} (\nabla u^n \cdot \mathbf{n}) + H^n \bar{v} (\nabla v^n \cdot \mathbf{n}) d\omega,
\end{aligned}$$

where the last equality is obtained by Green's formula. The first integral refers to the energy sink in the domain by viscosity. The boundary integral represents the viscous transport through the open boundary. As already mentioned in Section 2.1.3 an additional boundary condition is needed for the elliptical part of the equations. As proposed, for example, by Blayo & Debreu (2005) one possibility is to set the normal projection of the velocity gradient to zero (no tangent viscous stress). Then the open boundary term of the viscous transport would vanish. In the models under consideration the viscous energy flux is kept in the energy computation.

Finally to obtain the change of energy the terms have to be multiplied by the density of sea water.

Further, it should be noticed that the spatial approximation in terms of functions  $\Phi_k$  and  $\Psi_k$  results in the computation of integrals with up to three test functions multiplied with each other. Thus some elementwise approximations have to be made. Fortunately, the depth can be averaged over the elements in many terms.

Another complication in the discrete formulation are the non-conforming functions. The velocity value at an open boundary edge has contributions from all edge values of the boundary element. This results in a contribution from inner edge values on the open boundary flux. For example, for the transport of the potential energy through the open boundaries these terms contribute. They are not implemented for keeping the energy budget subroutine fast.

In summary there are four inconsistencies leading to some residual in the energy budget:

- Use of the fully NC advection in the energy budget, but P1 projection advection in the model
- Averaging of depth or elevation over the element
- Neglecting inner velocity values for the normal transport at the open boundaries

- Coriolis contribution

Later the residual is referred to as error. It is not an error in model, but an error in the energy computation. Neglecting the Coriolis contribution it brings mainly inaccuracy in the kinetic energy (flux and temporal change) and potential energy flux.

### 2.1.6 Conclusion

In this section the seven unstructured grid models for the following model simulations have been introduced. They are based on one of the following three different spatial discretizations:  $P_1^{NC} - P_1$  (called NC),  $P_1 - P_1$  (called P1P1) and FV after Chen *et al.* (2003) (called FV). NC naturally filters out pressure modes, while P1P1 has to use a certain stabilization. Therefore, P1P1 is only implemented with semi-implicit time- stepping, while the NC has the choices Adam-Bashforth (NCAB), Leap-frog (NCLF) or semi-implicit (NCSI) and FV has Runge-Kutta (FVRK), Adam-Bashforth (FVAB) and semi-implicit (FVSI). As the models differ with respect to the number of unknowns per triangle, the operations per time step and the order of approximation, the performance with respect to CPU time, time step size and error has to be compared.

The implementation of advection for NC models is tricky as the basis function of the velocity is discontinuous. Three possible solutions were discussed. One solution bases on the scheme proposed by Hanert *et al.* (2005). Another one is set up with the theory of distributions. The last one projects the discontinuous velocity on the continuous  $P_1$  functions before computing the advection. Advective processes are very important and these schemes have to be tested against each other.

The tidal solution in coastal shelf seas is mainly driven by an incoming wave. Solutions to the shallow water equations should be given by a well-posed system. Otherwise the solution may not exist in case of overdetermination of the boundary conditions or may not be unique, if too few conditions are prescribed. Since the tidal solution in the interior largely depends on the applied forcing at the open boundary, I classified the equations and derived boundary conditions in terms of characteristics for the hyperbolic part of the equations. Problems arise when the available data is insufficient to serve as boundary values. The practice is that several boundary conditions are implemented in the models and may be chosen according the available open boundary data.

Since tides originate from the tidal potential the mathematical and physical background known from literature has been repeated. As the tidal poten-

tial has only marginal influence on the tidal dynamics in the North Sea, a rather computationally cheap way for its computation proposed by Schwiderski (1980) has been used in this thesis. I have included it for completeness. More difficult is the computation of secondary tidal forces, the loading and self-attraction (LSA) by Earth and water masses. Here estimates in terms of Love-numbers are usually used. In terms of Earth masses the Love-numbers proposed by Farrell (1972) are implemented in the model. Although some local approaches exist the majority of schemes calculating the LSA of tidal water masses known in literature, need the tidal wave over the whole Earth. As the model domain is not global, the LSA effects by the tidal water bulge are not taken into account.

Tidal simulations are not only made to estimate current velocities and tidal high and low water, but also for energy transfers. Since unstructured mesh methods potentially resolve better than FD models and use certain function spaces, their models may on the one hand contribute to a better approximation of energy fluxes and on the other hand have to be validated more thoroughly than FD methods. More attention has to be given to the influence of numerical effects. I derived the energy equations and implemented them for one of the models. The results of changes in kinetic and potential energy, the flux of energy through the boundaries and its dissipation by bottom friction and viscosity has to be analyzed and compared with already existing FD models.

## 2.2 Simulation results

In this section I present simulation results on realistic settings. First the model intercomparison in Section 2.2.1 serves to highlight the influence of the spatial and temporal discretization in terms of different unstructured grid methods and to select the models with the best computational performance. Afterwards in the following sections one of the models run on a finer mesh spanning over the northern European Continental Shelf. The aim is to identify possible model deficiencies and give further model improvement to represent tidal dynamics.

### 2.2.1 Model intercomparison for $M_2$ tidal wave

#### Model Setup

The seven models (NCLF, NCAB, NCSI, P1P1, FVAB, FVRK and FVSI) run for 24 tidal  $M_2$  cycles before the tidal analysis starts. This is done to sufficiently damp transient solution parts. One last cycle is used for the analysis of tidal amplitude and phase. Since a wetting & drying scheme is not

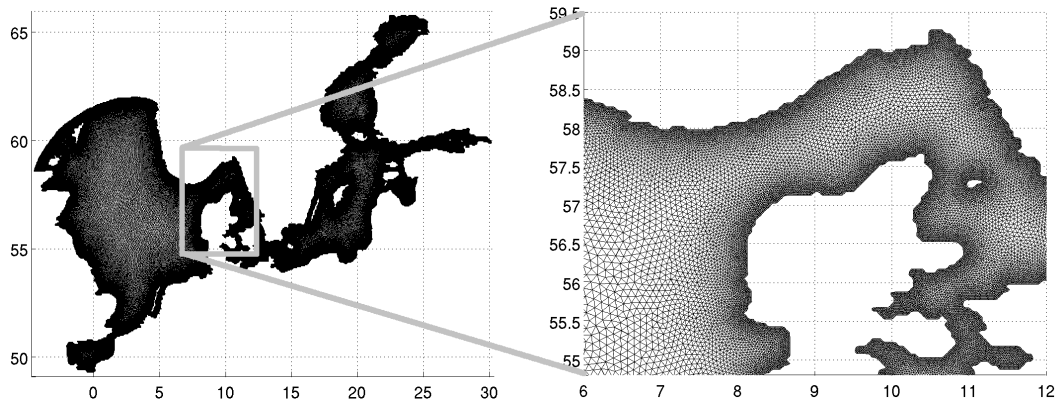


Figure 2.3: Mesh of the North and Baltic Sea formed by 121699 nodes in 233872 elements; minimal (maximal) edge length is 796 (3014) m; horizontal resp. vertical axis are longitude resp. latitude in degree.

implemented in all models, a minimal depth of 5 meters has been set. Furthermore, the standard choice of the bottom friction coefficient of 0.0026 and horizontal diffusion coefficient of  $A = 10 \frac{m^2}{s}$  is taken. The time step size is chosen individually for each model and summarized in Fig. 2.10. The tidal potential has been turned off.

The grid covers North and Baltic Sea with approximately 234000 triangular elements. They have an edge resolution varying between 800m and 3km (see Fig. 2.3). This mesh is not supposed to demonstrate all the advantages of unstructured grids in terms of resolving the coastal boundary. But it is reasonably smooth to prevent numerical instabilities and has a moderate size to facilitate the comparison between the different discretizations. Simulations on much more detailed meshes (with more favorable location of the open boundaries and better representation of the coastal zone) will be done later.

The mesh contains two open boundaries. One is located near the shelf break, i.e., between Scotland and Norway at the northern end of the North Sea and the other is in the western side of the British Channel. The models are forced by the elevation prescribed at the open boundaries. For the northern open boundary the  $M_2$  tidal data at the open boundaries are extracted from the OTPS model solution TPXO6.2 of oceanic tides. This is a global tidal model, which assimilates altimetric data (Egbert *et al.*, 1994; Egbert & Erofeeva, 2002). At the open boundary in the English Channel I prescribe the elevation by station data located in the vicinity.

The bathymetry from GEBCO morphometry dataset in one minute resolution is employed ([http://www.bodc.ac.uk/data/online\\_delivery/gebco/](http://www.bodc.ac.uk/data/online_delivery/gebco/)).

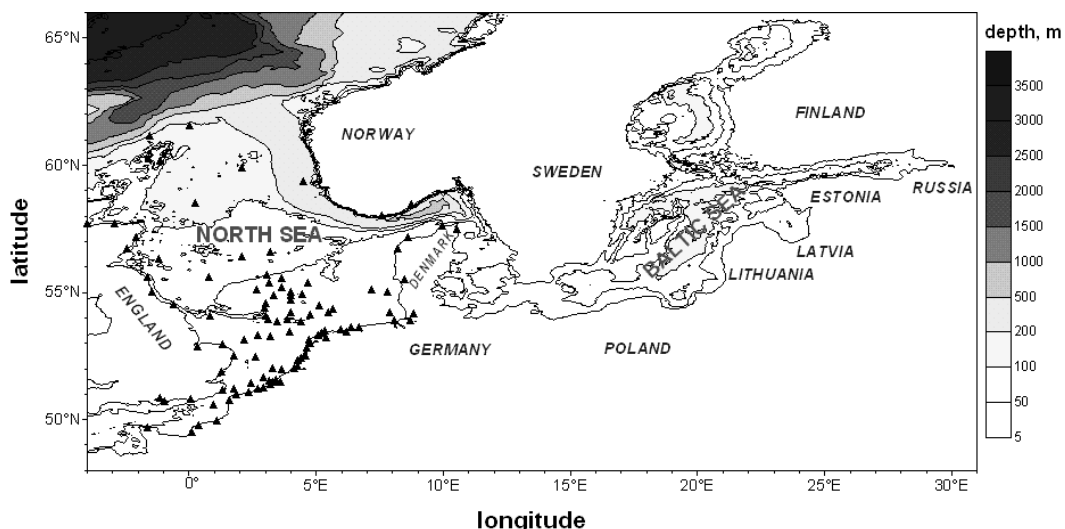


Figure 2.4: Geographical location of the North Sea and Baltic Sea. The triangles indicate the station locations.

### Comparison with tide gauges

In general, all models reproduce the tidal chart known from literature (Defant, 1961; Sinha & Pingree, 1997) fairly well. Fig. 2.4 shows the domain and the location of the tide gauges used in the comparison of amplitude and phase. The tidal harmonics of 112 stations are kindly provided by Andersen (2008).

The observation points are mainly located near the coast or clustered in some area of the North Sea (see Fig. 2.4). Note that this intercomparison aims at comparing different time and space discretizations and thus, it is not intended to achieve high accuracy of the dedicated models in terms of the simulation results. There are several sources of possible errors. First, I made an assumption of five meter minimal depth instead of including wetting and drying. Second, no attempts have been made to tune the bottom topography and bottom friction coefficients were taken constant over the whole domain. Several studies like, for example, Lu & Zhang (2006), show the importance of varying bottom friction in 2D shallow water model. But for the comparing the different models the current setup is sufficient.

Fig. 2.5 shows for the semi-implicit models NCSI, P1P1 and FVSI the observed amplitudes and phases against the computed ones. I only display the results of the semi-implicit simulations, as differences between model runs with identical spatial but different temporal discretizations can hardly be seen. The analysis illustrates a high level of reliability of the computed results for all tested schemes. Except for the P1P1 code, all models have a tendency to underestimate the amplitude. But, as the stations do not uni-

formly cover the domain and are distributed mainly along the coast, the error is obviously biased.

Considering models with the same spatial discretization it is difficult to give preference to any of them. The order of time discretization proves to be sufficient (given the order of their spatial discretization) to provide the same overall accuracy. In this case the choice of the optimal scheme (for the same spatial discretization) will be determined only by its computational cost.

### **Comparison with EOT data**

The next step is to determine the location of largest errors and trace their sources. For this reason I took the EOT08 data (Savcenko & Bosch, 2008), which is available in most of the domain except for the shallow coastal parts, and computed the differences between them and our model results. Figures 2.6, 2.7 and 2.8 show the spatial structure of the errors in amplitude and phase for all tested schemes. They all place the maximal error in phase and amplitude in the British channel and the region adjacent to it. Such a systematic error can be explained by insufficiently good bathymetry data (or its resolution by the mesh), and also with errors in the open boundary conditions near to British channel. The fact, that FV codes give slightly worse results in this area and that the momentum equation is written in the flux form, hints at errors in the depth representation.

In Fig. 2.7 the phase errors in the NC and FV schemes are similar and stronger in the German Bight and near the amphidromic points.

It is also noticeable that the same spatial discretization yields the same pattern of error. The NC models have larger differences near the northern open boundary and compared with the FV models underestimate the amplitude more along the British coast. When I compare the forcing data TPXO6.2 and station against EOT08 data (not shown here), one would see that the overestimation at the open boundary in the NC codes is very similar to that in the TPXO6.2 solution used as forcing. Consequently the NC solutions are closer to the forcing than the FV solutions. If the forcing were more consistent with the station data, the NC codes would provide better agreement with the observational data.

The P1P1 code shows the same difficulty at the open boundary. Additionally the rigid boundaries seem to be problematic for it, as the amplitude is overestimated over most of the region adjacent to the coast. It has to be mentioned that the FE discretizations used here differ at the boundaries. In the non-conforming implementations the velocity is given at edges while in the P1P1 model it shares the same location with the elevation. Together with stabilization in P1P1 code, this can have an impact on the behavior in the vicinity of boundaries.

In general I observe similar patterns of errors in all simulations. The struc-

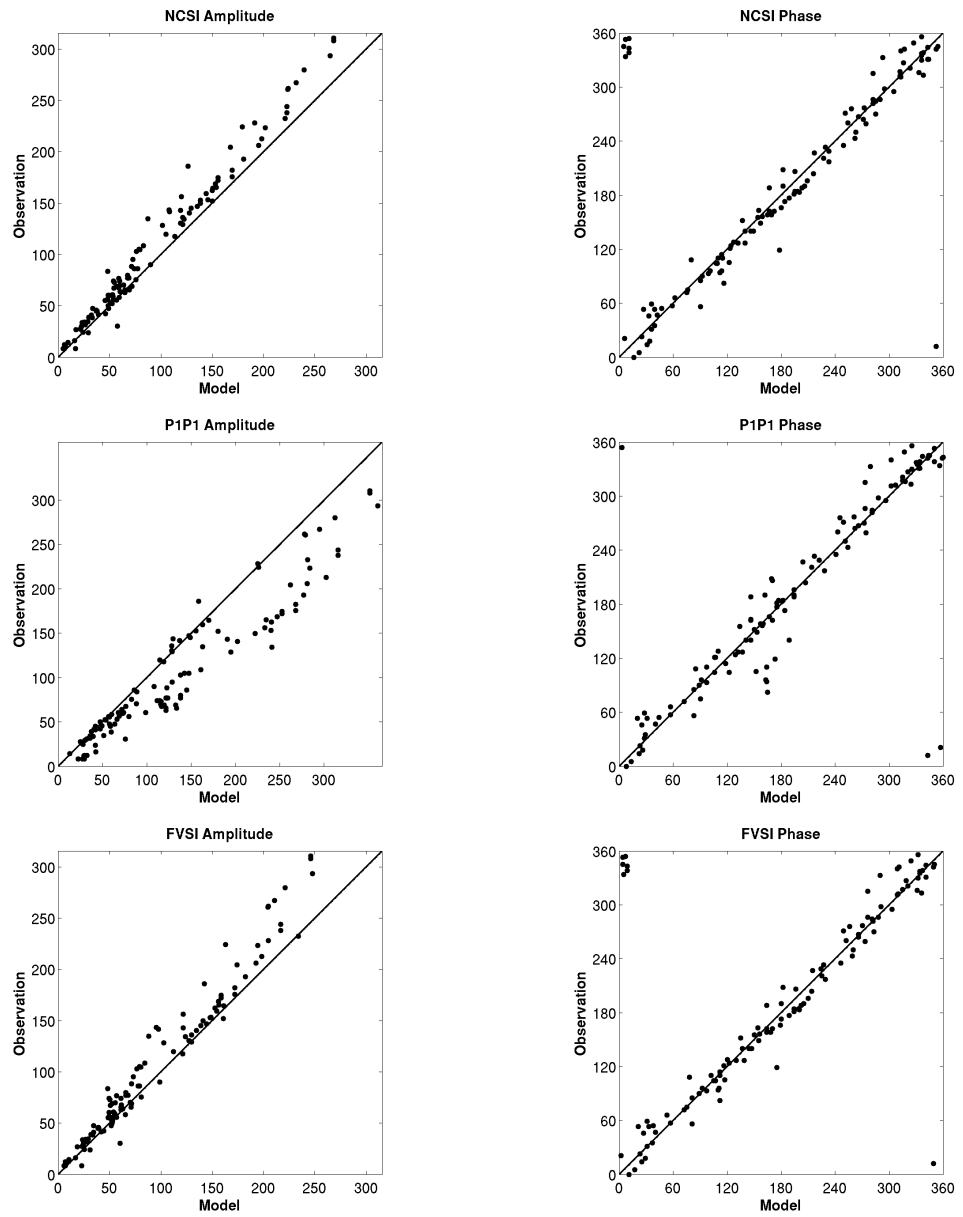


Figure 2.5: Computed over observed amplitude (left side) in cm and phase (right side) in degree for (from top to bottom) NCSI, P1P1, FVSI

ture of error in the German Bight and near the Danish coast is quite similar for the NC and FV codes. This suggests that the major source of error is common to all models and is not linked to numerical properties (absence of wetting & drying, constant bottom friction coefficient and error at open boundary are most likely to be the reason).

### Error measures

The accuracy of calculations is frequently expressed through the vector error given by the formula

$$\mu = \frac{1}{N} \sum_{n=1}^N \sqrt{[(A_* \cos \varphi_* - A \cos \varphi)^2 + (A_* \sin \varphi_* - A \sin \varphi)^2]_n}, \quad (2.42)$$

where  $(A_*, \varphi_*)$  and  $(A, \varphi)$  are the observed and calculated values of amplitudes (in centimeters) and phases, at the stations 1 to  $N$ . The total vector error (Fig. 2.9) does not exceed 34 cm for all 112 stations for six from seven tested schemes, where only P1P1 gives a larger value of about 46 cm. Similar results are obtained by computing correlation between modeled and observed level oscillation for one tidal period of  $M_2$ . The correlation is expressed by

$$R = (N\sigma_*\sigma)^{-1} \sum_{n=1}^N [\eta'_* \eta'_n], \quad (2.43)$$

where  $\eta'_n := \eta_n - \frac{1}{N} \sum_{n=1}^N \eta_n$ , and  $\sigma = \sqrt{\frac{1}{N} \sum_{n=1}^N (\eta'_n)^2}$ . For six from seven tested schemes the correlation coefficient is of the order of 0.94 (see Fig. 2.9). For P1P1 it is smaller, but still high enough to confirm similarity.

To distinguish the influence of the time and space discretization on the phase and amplitude I use the relative error  $r_A$  in amplitude and the hour error in phase for the different schemes. The averaged relative amplitude error is given by the following expression

$$r_a = \delta_A / |\bar{A}|, \quad (2.44)$$

where  $\delta_A = \frac{1}{N} \sum_{n=1}^N |A_* - A|_n$ ,  $|\bar{A}| = \frac{1}{N} \sum_{n=1}^N |A|_n$ . A measure for the phase error is obtained, when the phase differences given in degree are mapped on hourly differences and averaged. It is called hour error and for the  $M_2$  with half cycle length of 6.21h given by

$$\frac{1}{N} \sum_{n=1}^N |p(\varphi_* - \varphi) / 180^\circ|_n \cdot 6.21, \quad (2.45)$$

where

$$p(x) = \begin{cases} x - 360^\circ, & x > 180^\circ \\ 360^\circ + x, & x < -180^\circ \end{cases} \quad (2.46)$$

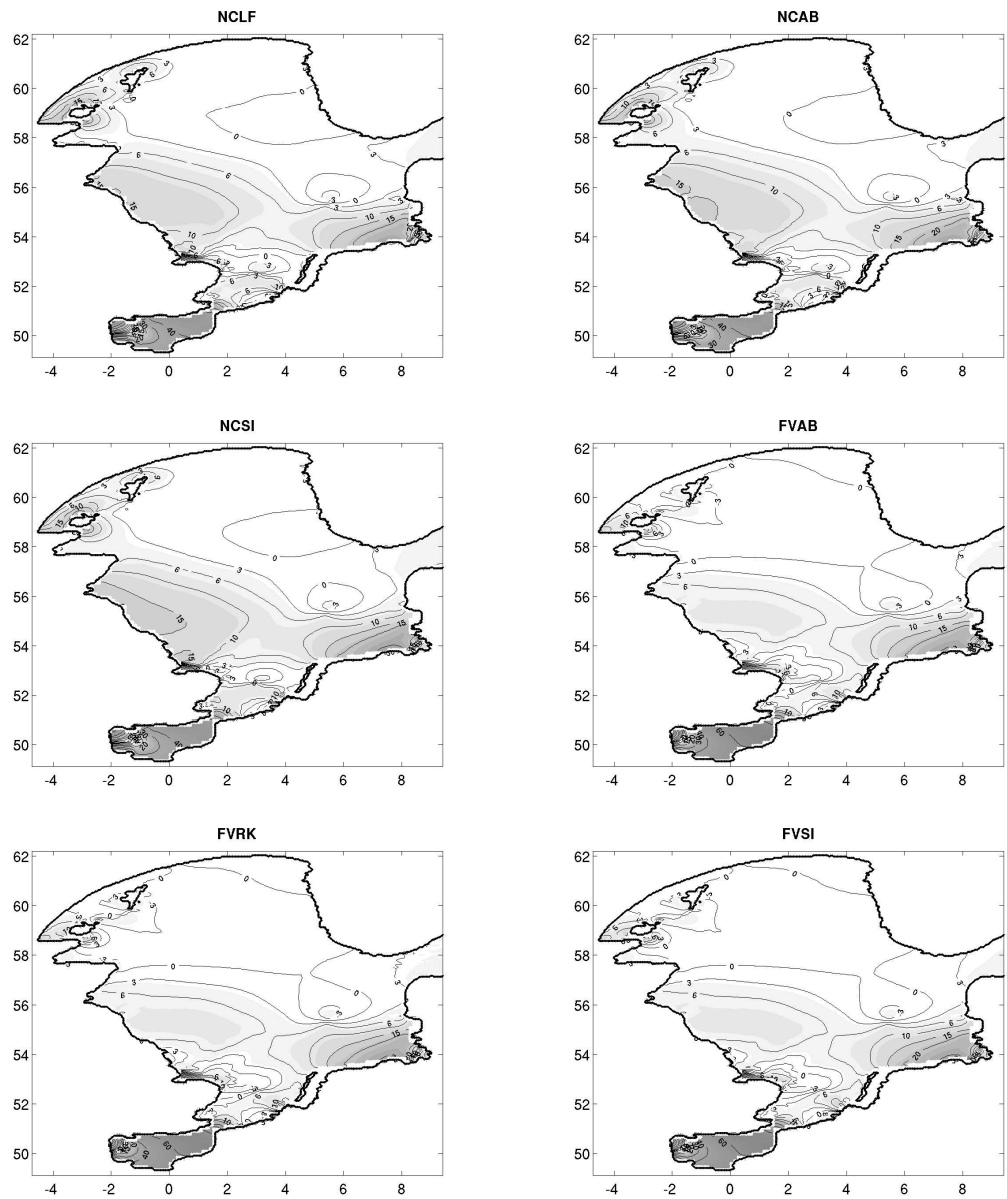


Figure 2.6: Observed minus calculated amplitude in cm (contour line difference is 5cm). Horizontal resp. vertical axis are eastern, western longitude resp. northern latitude in degree.

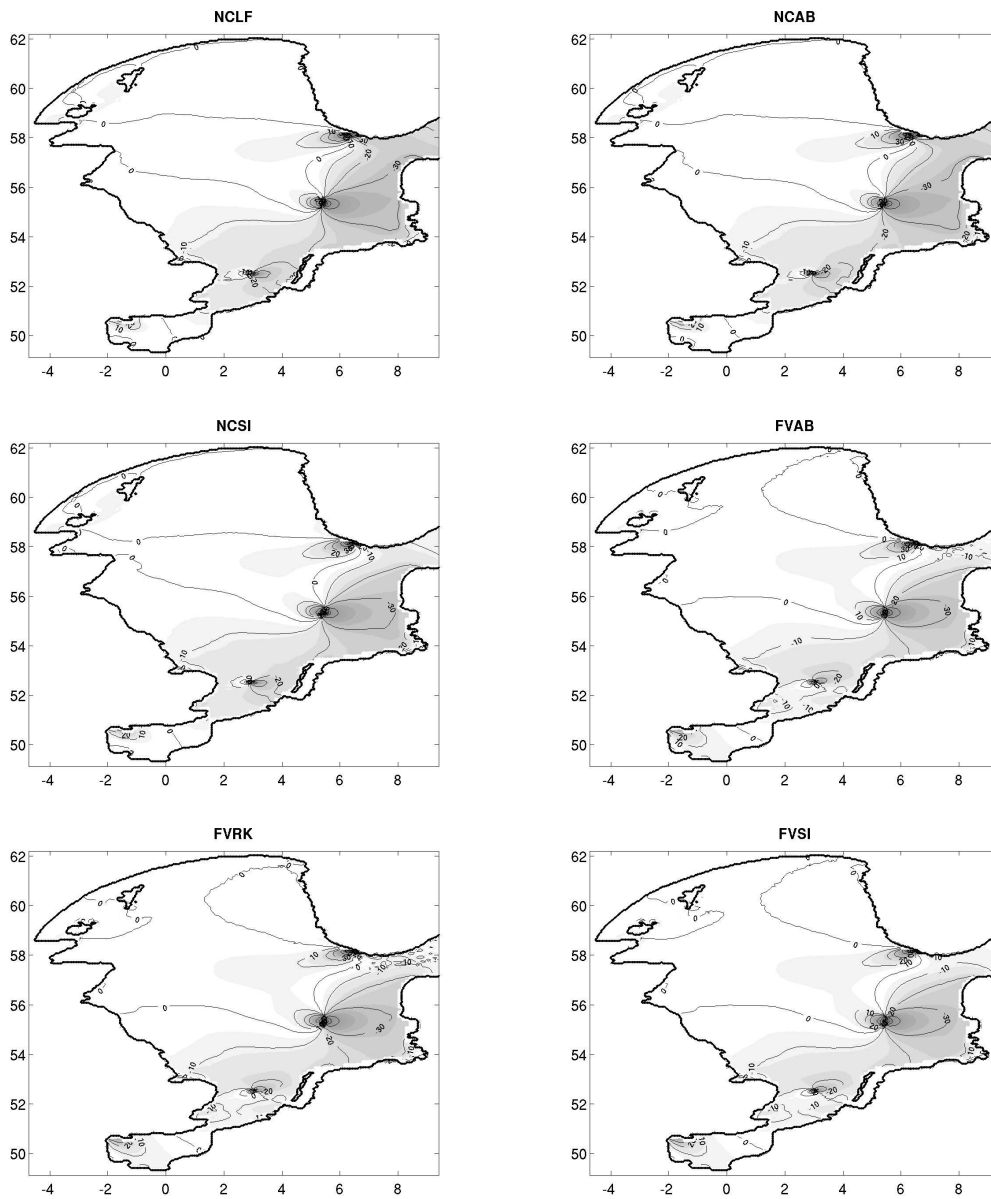


Figure 2.7: Observed minus calculated phase in degree (contour line difference is  $10^\circ$ ). Horizontal resp. vertical axis are eastern, western longitude resp. northern latitude in degree.

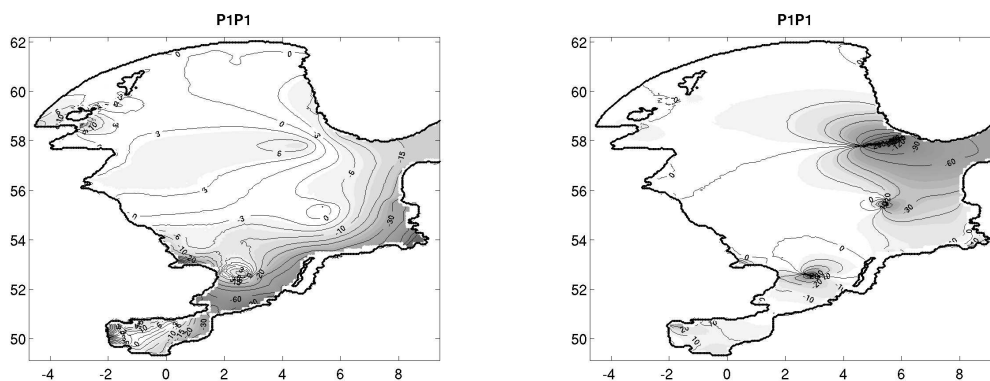


Figure 2.8: Left: Observed minus calculated amplitude in cm for P1P1 (contour line difference is 5cm). Right: Observed minus calculated phase in degree for P1P1 (contour line difference is  $10^\circ$ ). Horizontal resp. vertical axis are eastern, western longitude resp. northern latitude in degree.

The results are displayed in Fig. 2.9 and show that the hour and relative amplitude errors do not differ between the different time stepping schemes for the FV models. NCSI is also very close to the results of the FV codes. In contrast to this are NCLF and NCAB, which are better in amplitude, but worse in phase. P1P1 has the amplitude and phase error considerably higher than for the others models. But note that the hour error is still comparable to the other models, even though the amphidromic point at the Norwegian coast is shifted. This is explained by the fact that the central amphidromic point (see Fig. 2.8) is better localized than for the other models. Further, there are more measurements in this area than at the Norwegian coast, where only a few stations are available (see Fig. 2.4).

Note that the relative error is still between 13% and 23%, which is far from what can be achieved. Further improvements in mesh and bathymetry, as well as the implementation of wetting & drying will considerably reduce the error.

### Computational cost

The computational efficiency is examined by comparing the CPU time needed to calculate one tidal cycle on our North- and Baltic Sea grid with about 234000 elements. Each of the models is run in a serial mode (on a single processor) and repeating the runs show little variation in CPU time. Fig. 2.10 illustrates the total CPU time necessary for one tidal period, as well as its distribution between the calculation of momentum and the continuity equation. The time step size (shown in the upper right panel in Fig. 2.10) has been optimized for each model. Only NCSI is able to use even larger

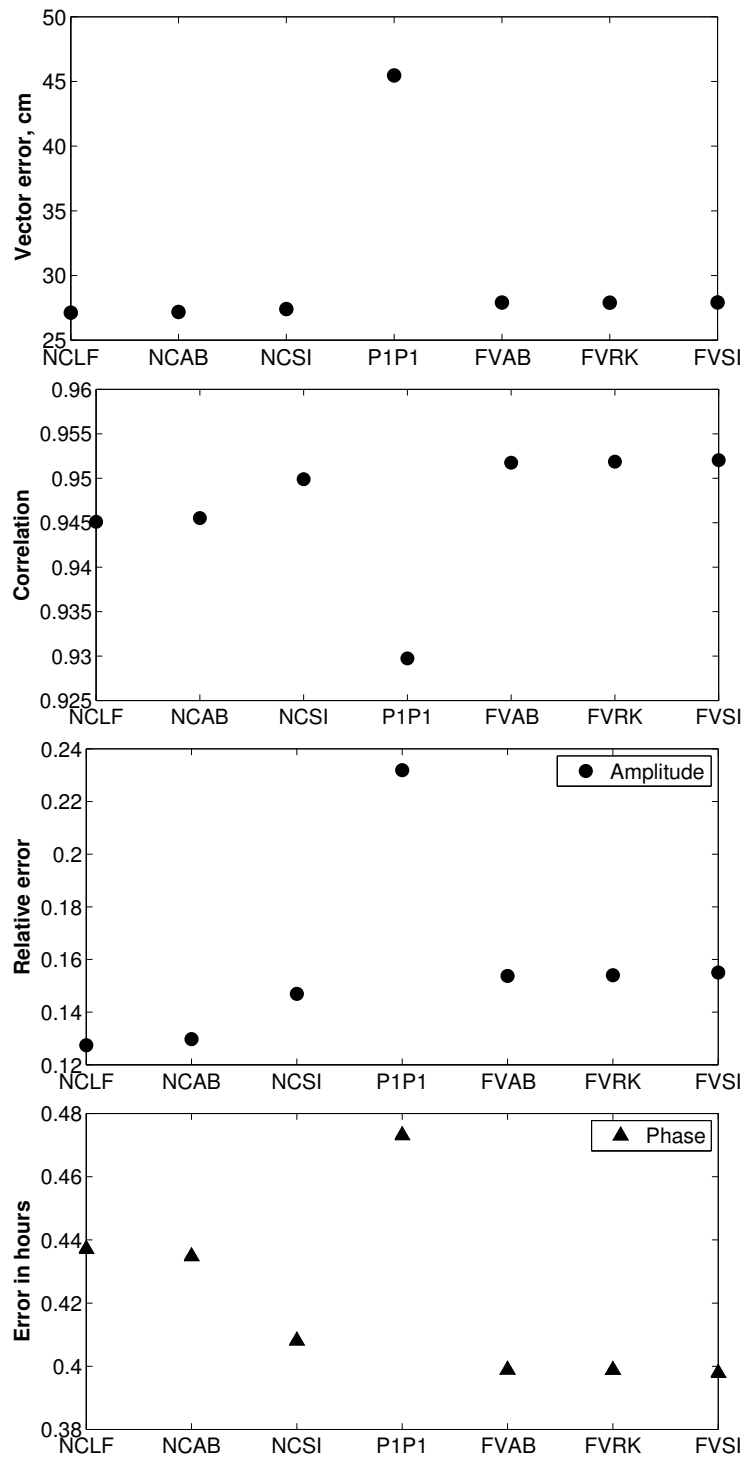


Figure 2.9: From top to bottom: vector error, correlation, relative amplitude error and hour error.

time steps than plotted here. The time step in the semi-implicit codes is by at least a factor of two higher compared with the explicit codes. This brings immediate performance advantages as the number of iterations reduces. Thus, the semi-implicit codes need much less than half of the time used by respective explicit codes.

NCAB and FVAB have the same time step size. Since there are about 1.5 times more edges than elements (so the loops in NCAB are longer), FVAB needs nearly half of the time taken by NCAB. Comparing FVAB and FVRK concerning time step size and total CPU time, I observe that although FVRK takes double time step size, its total CPU time is higher. The reason for this lies in the fact that Runge-Kutta time stepping is of fourth order and the rhs of the continuity and momentum equations has to be computed four times. FVRK would pay off, if one used four times higher time step size than FVAB. For NCAB and NCLF the same time step size translates into their CPU time being almost the same. FVSI is not able to take as large time steps as the FE semi-implicit codes, but it is still comparable in total CPU time with NCSI and P1P1. This shows that the FV code provides a more efficient implementation in term of the number of floating point operation needed to perform a time step.

However, in the general case, in regions with stronger non-linearities, a long time step size may no longer be appropriate and the explicit codes might be faster in that case.

But actually, the influence on the results by the time step size itself is very small and I never saw significant differences. This can be explained by the fact that the CFL number based on the phase speed of gravity waves remains smaller than one (in average over the mesh), even for the semi-implicit codes. Explicit unstructured mesh models are frequently not able to use as big time steps as suggested by theoretical analysis. One reason is the low order spatial discretization (and augmented residual errors) on unstructured meshes with variable resolution.

Further, the splitting of CPU time into the time spend for continuity and momentum equation gives more insight in the performance. They are shown in the bottom left and right graphs in Fig. 2.10. The computation of the momentum equations in NCLF and NCAB need much more time than in NCSI. The efficiency of the NCSI code can directly be related to the larger time step size and is simply determined by frequency of computing the right hand side. For the continuity equation this is different. Here, NCSI needs more time to call the solver. But, the difference in the CPU time compared with NCLF and NCAB is not as pronounced as in the case of the momentum equation.

Comparing FVSI with the explicit FV codes one notices that FVSI saves time in the momentum computation because of its increased time step size, while the time spend for the continuity equation is of the order of those for FVAB and FVRK. This is once again because of calling the solver.

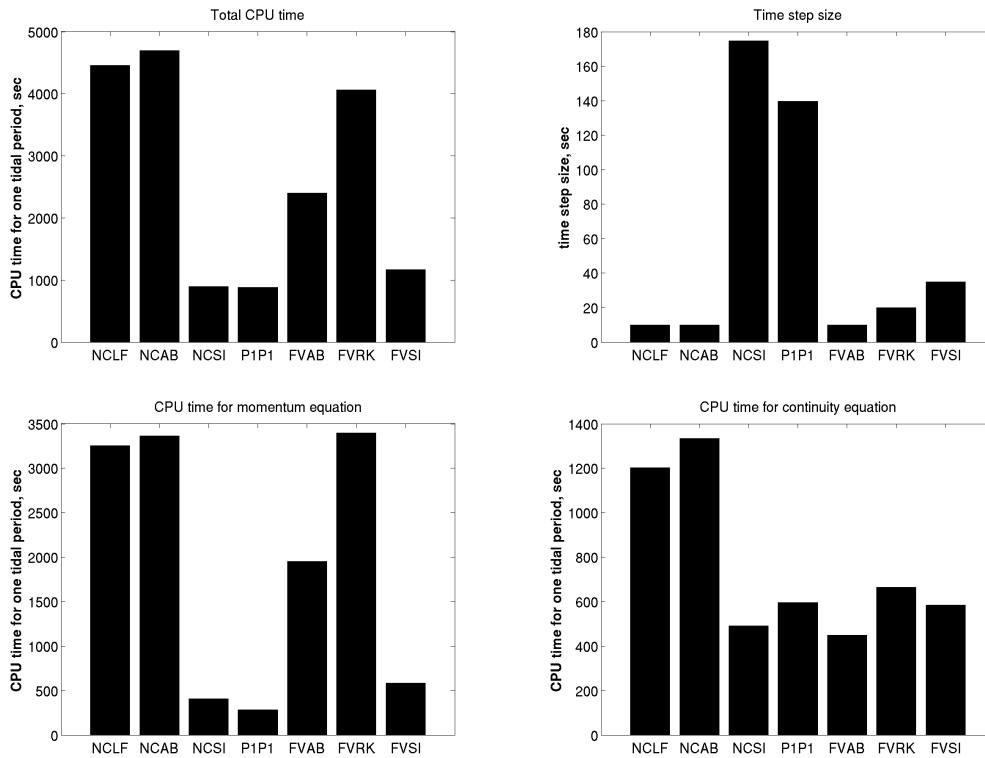


Figure 2.10: CPU time in seconds to compute one tidal cycle (upper left figure total time, bottom left for momentum equation, bottom right for continuity equation), time-step size in seconds (upper right figure).

NCSI and P1P1 are comparable in the CPU time for momentum and continuity equation. P1P1 has less degrees of freedom in the velocity than the NCSI, which results in smaller loops. However, the velocity mass matrix is not diagonal anymore and calls for an iterative procedure are relatively expensive.

## 2.2.2 $M_2$ tidal simulations on the European Continental Shelf

The NCSI model is further analyzed in this section by computing the energy balance, residual currents and current ellipses. The model intercomparison of Section 2.2.1 was done in a setup, which was feasible for all models. The mesh was smooth, the open boundary clamped and no wetting and drying was used. NCSI turned out to be one of the best models. I identified a major error component introduced by the open boundaries. To have the open boundary away from narrow or shallow regions, a new mesh was, there-

fore, generated on the whole European Continental Shelf. A description of the mesh can be found in Section 4.3.2. In the following simulation I use NCSI with clamped boundary condition at the open boundary and free slip at the closed boundary. The time step size is about 7 seconds and it was integrated over 16 tidal cycles before starting the analysis.

### Energy balance

According to Flather (1976) the north-west European shelf contributes to the total loss of tidal energy in shallow seas by about 10%. It is, therefore, a very important sink of energy.

I estimate the dissipation and the transport of energy in the domain by the equations presented in Section 2.1.5. Fig. 2.11 and Fig. 2.12 present the model result. The change of potential energy increases and decreases periodically with a period of a half tidal cycle length (red dashed line in Fig. 2.11). The same happens with the kinetic energy but in antiphase with the potential energy (dark blue in the same figure).

The potential energy transport through the open boundaries (magenta) show periodical entering and leaving of energy. But the mean flux is positive with 204.87 GW. The kinetic energy flux is about two orders of magnitude smaller with a maximal value of 3.44 GW and minimal value of -2.96 GW. In the first half of the cycle energy is injected and in the second half energy is extracted from the domain (upper plot in Fig. 2.12). The average input over one tidal cycle is only about 0.07 GW. The average of kinetic and potential energy flux over one tidal cycle is 204.94 GW, which is a bit smaller than the value proposed by Flather (1976) of 214.8 GW.

The value in my simulations is consistent with the average energy dissipation. The energy loss by bottom friction varies cyclically with an average value of -203.17 GW (dashed green line in Fig. 2.11). The viscosity dissipates energy with an average of -0.53 GW (dark blue line in the lower plot of Fig. 2.12). The difference between energy flux into the domain and dissipated energy is 1.24 GW. This means that the model is not yet in equilibrium although 25 cycles were calculated before the energy computation. It can also be seen in the plot of the kinetic plus potential energy (see lower plot in Fig. 2.13). Especially the potential energy is still increasing, while the kinetic energy is decreasing.

Averaging potential and kinetic energy change in the domain gives an increase of 0.71 GW during one tidal cycle. In average the unknown terms give another 0.11 GW of error. The residual may be explained by the advection scheme. In Eqn.(2.41) the splitting between kinetic energy change and kinetic energy flux into the domain came from the rewriting the advection terms. In the model the projection method for the advection was used, but not translated into the energy calculation as well. Consequently, the calculated energy budget need not to be fully balanced. Leaving aside the other

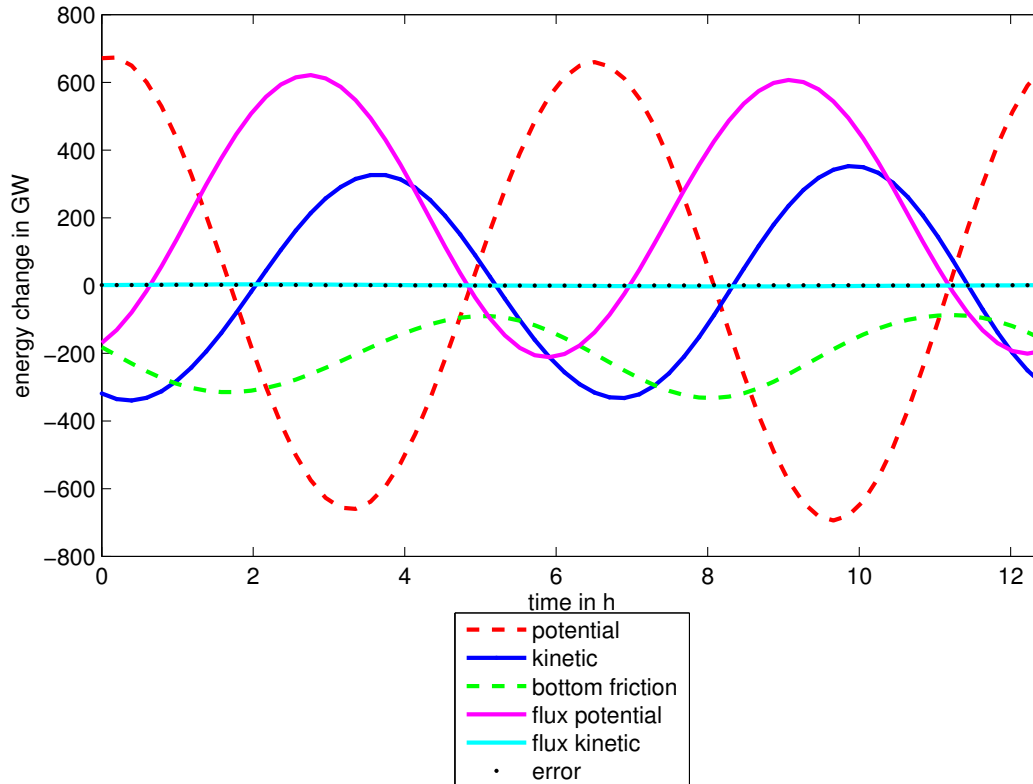


Figure 2.11: Change of energy in GW during one tidal  $M_2$  cycle: temporal change of kinetic (dark blue) and potential (red) energy, flux of kinetic (dashed light blue) and potential (dashed magenta) energy through the open boundaries, energy loss by bottom friction per second (dashed green), error or residual in the energy budget (dotted black).

inconsistencies pointed out at the end of Section 2.1.5, the residual can be used to draw some conclusions on the influence of the projection method on the simulations. The energy residual suggests, that more energy is dissipated with the projection method. As the projection method smooths the velocity and is more stable than the other methods (see Section 2.1.5), this conclusion is consistent.

To bring the system into energy equilibrium it may be advisable to calculate some more cycles. Another way to correct the imbalance is to increase the bottom friction coefficient values and therefore, add some frictional energy dissipation. The bottom friction coefficient does not have to attain the assumed constant value in reality. Further, the frictional loss depends to the power of three on the velocities. So small changes in the velocities have a big influence on the estimate.

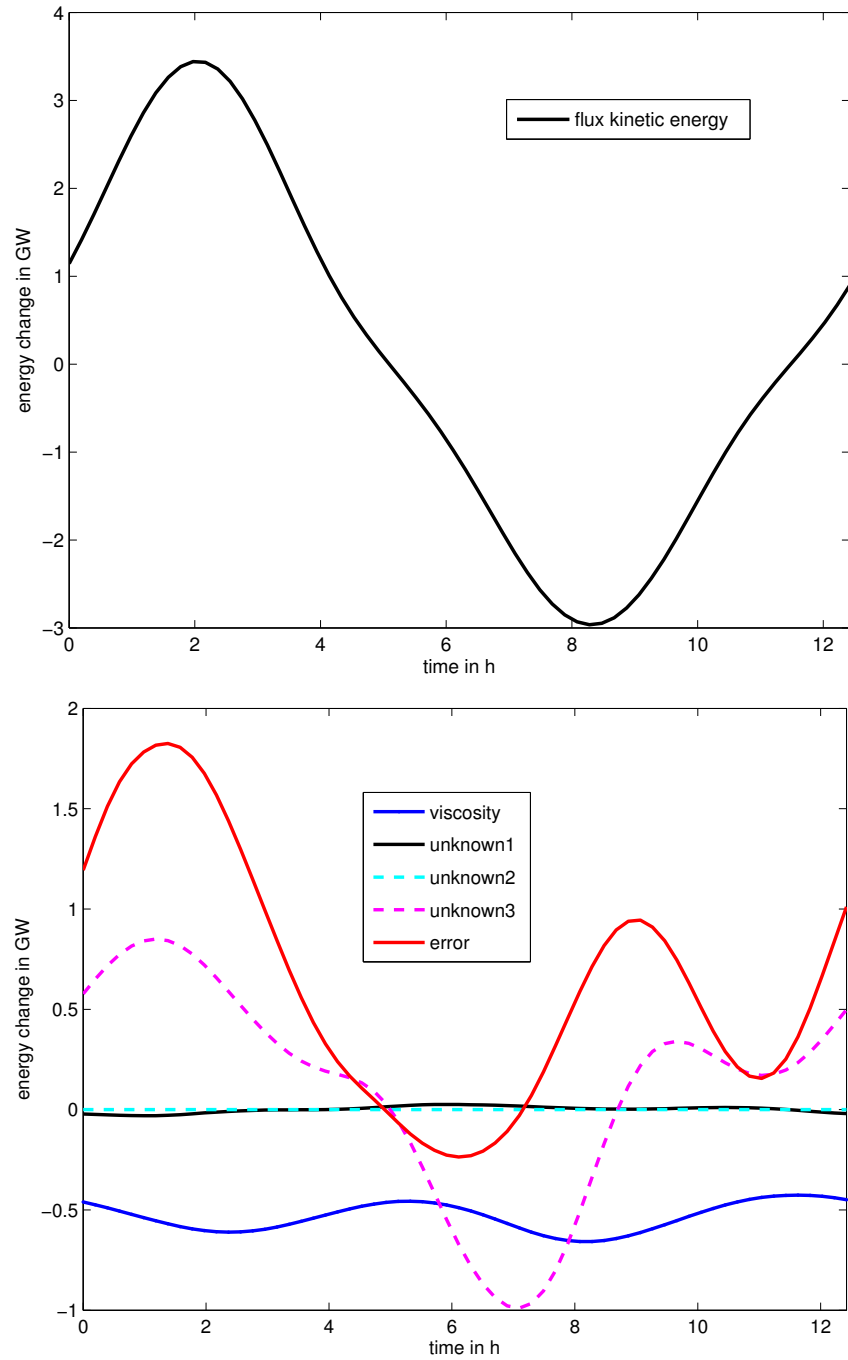


Figure 2.12: Upper graph: Change of energy in GW during one tidal  $M_2$  cycle: Kinetic energy flux; Lower graph: energy dissipation by viscosity (dark blue), unknown terms 1 to 3 (black, dashed light blue, dashed magenta), error (red).

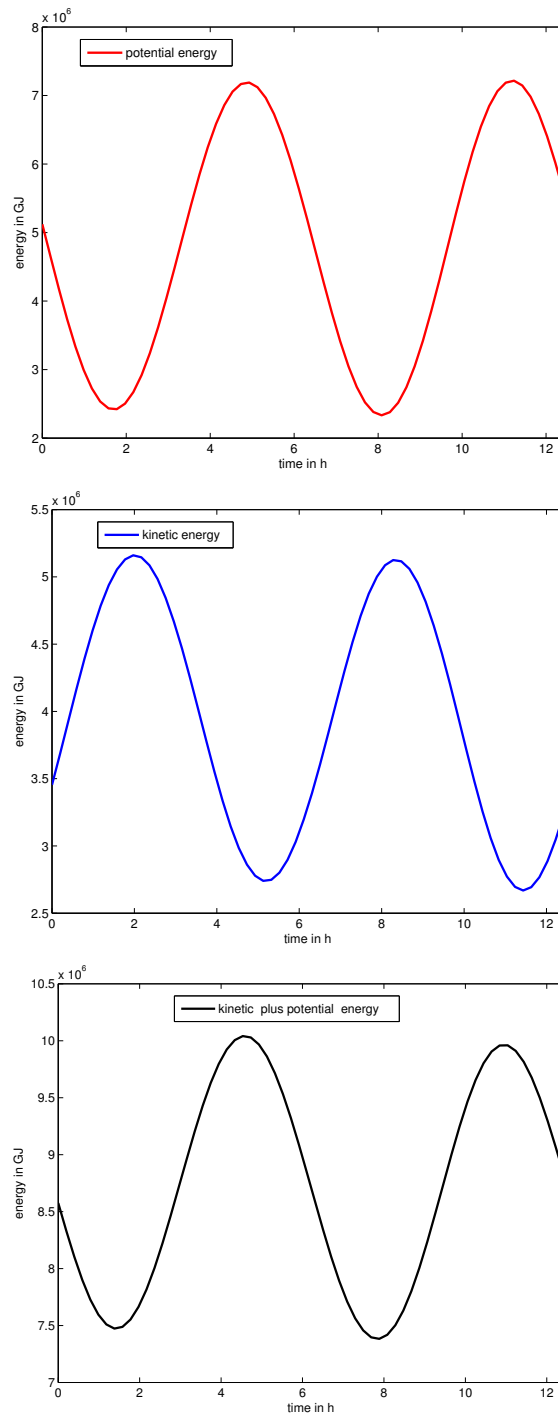


Figure 2.13: Energy in the domain over one tidal  $M_2$  cycle: Potential energy (upper graph), kinetic energy (middle graph), potential plus kinetic energy (lower graph).

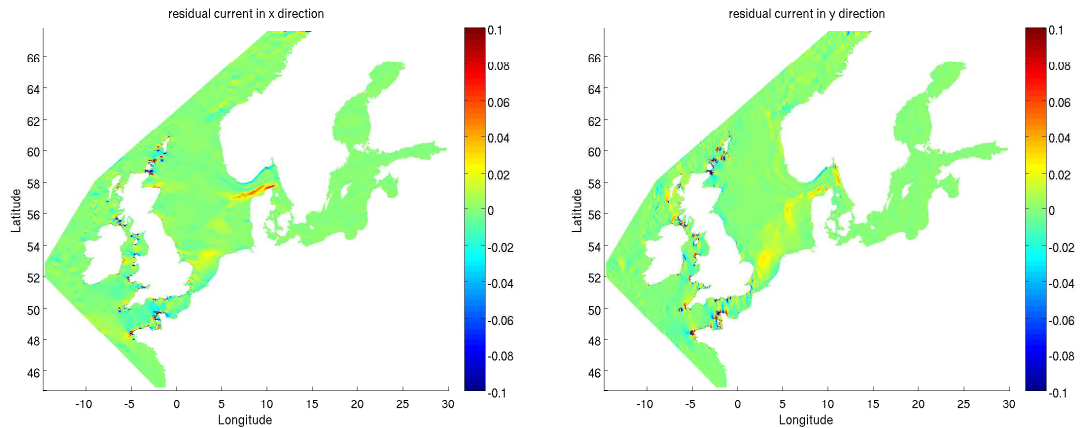


Figure 2.14:  $M_2$  tidal residual currents in m/s: in west-east direction (left figure), in south-north direction (right figure).

### Tidal residual currents

Since flooding and ebbing velocities are not perfectly symmetric, the tides generate residual currents. Further, the non-linear terms give rise to a net displacement of water particles. These residual currents have typical magnitudes of some  $\text{cm s}^{-1}$ , which is about one or two orders of magnitude smaller than the tidal currents (Kantha & Clayson, 2000). Because of the steadiness they contribute to the transport of sediments and pollutants. Further, their eddies contribute to the dispersion and mixing of particles. As they depend also on the vorticity generated by coastline features, unstructured grid models are needed for their computation.

I calculate the residual current by averaging the currents over one tidal cycle. Note that the Eulerian residual field is obtained, which is not necessarily the velocity the particles are transported with (Vreugdenhil, 1994). Their path is computed from the Lagrangian velocities. Nevertheless, the Eulerian residual field gives an approximate view of the expected transports.

In Fig. 2.14 the tidal residual currents of the  $M_2$  tidal wave show the generation of eddies at the coastline (visible by changing signs of the velocity components). These eddies are more prominent in the English Channel, along the west coast of the United Kingdom, the Irish Sea and the Shetland Islands. Probably the complexity of coastline leads to significantly different ebb and flood velocities resulting in high residual currents.

The magnitude of the residual currents are shown in Fig. 2.15. The coastline is marked with higher residual currents than the rest of the domain. Remarkably is the band of north-eastwards directed residual current between the south-west North Sea and the Skagerrak. The band meanders to the Skagerrak, where it intensifies.

Picture (a) in Fig. 2.16 shows the Skagerrak area itself. The relatively strong eastward current in the South turns northward at the Swedish coast and fol-

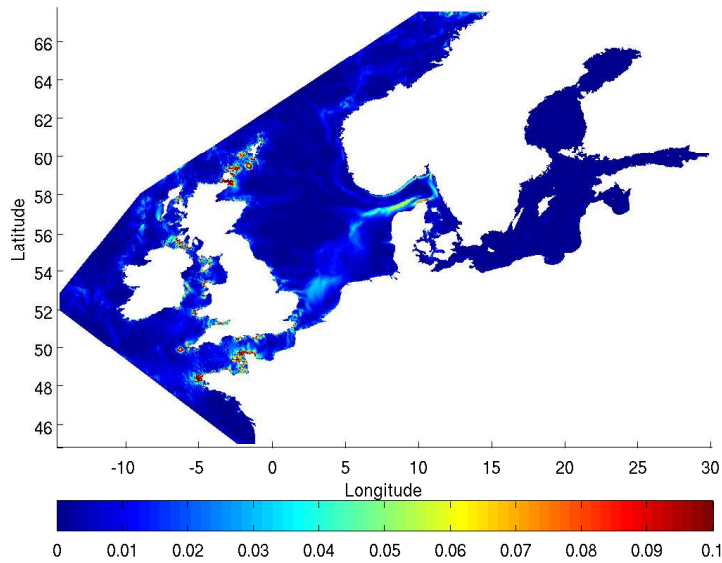


Figure 2.15: Absolute value of  $M_2$  tidal residual currents in m/s.

flows the Norwegian coast in westward direction. The westward current is not only confined close to the Scandinavia coast. The Norwegian trench shows also a westward current with a smaller magnitude due to the greater depth.

As the tidal residual current is much weaker than the basin wide residual circulation introduced by the wind, it can hardly be extracted from measurements. Model experiments are, therefore, good to distinguish between the different sources. Djenidi & Ronday (1985) compared the residual currents in tidal simulations with and without wind stress. The circulation in the Skagerrak matches the simulation results described above. Anticlockwise tidal residual circulations has also been observed in a bit different context by Yanagi & Yoshikawa (1983). They identified two generation mechanism, one related to the Coriolis force and the other one to the bottom slope. The exact source of the kind of circulation in the North Sea may also be attributed to these mechanisms.

Two of the main connections between the North- and the Baltic Sea, the Øresund near Copenhagen and the Storebælt between Langeland and Lolland, have residual currents shown in picture (b) and (c) of Fig. 2.16 and Fig. 2.17. The model resolution may be insufficient and, therefore, the computed currents have to be taken with caution. I observe an inflow in the Baltic Sea in the Øresund. In the Storbælt many eddies exist.

Djenidi & Ronday (1985) observed in their tidal residual currents an inflow into the North Sea through the Strait of Dover under negligible wind con-

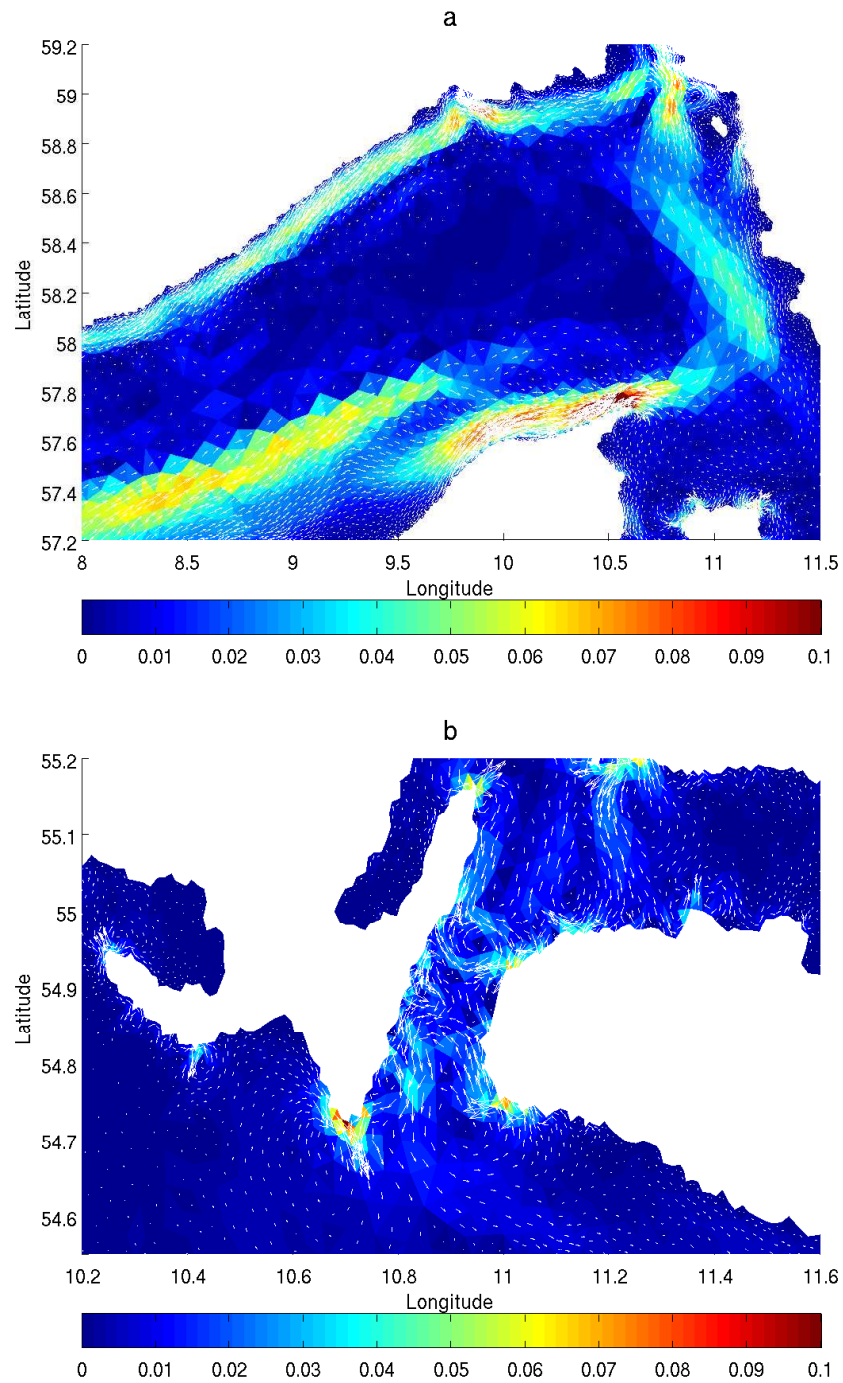


Figure 2.16:  $M_2$  tidal residual currents in m/s: a) Skagerrak, b) Storebælt between Langeland and Lolland.

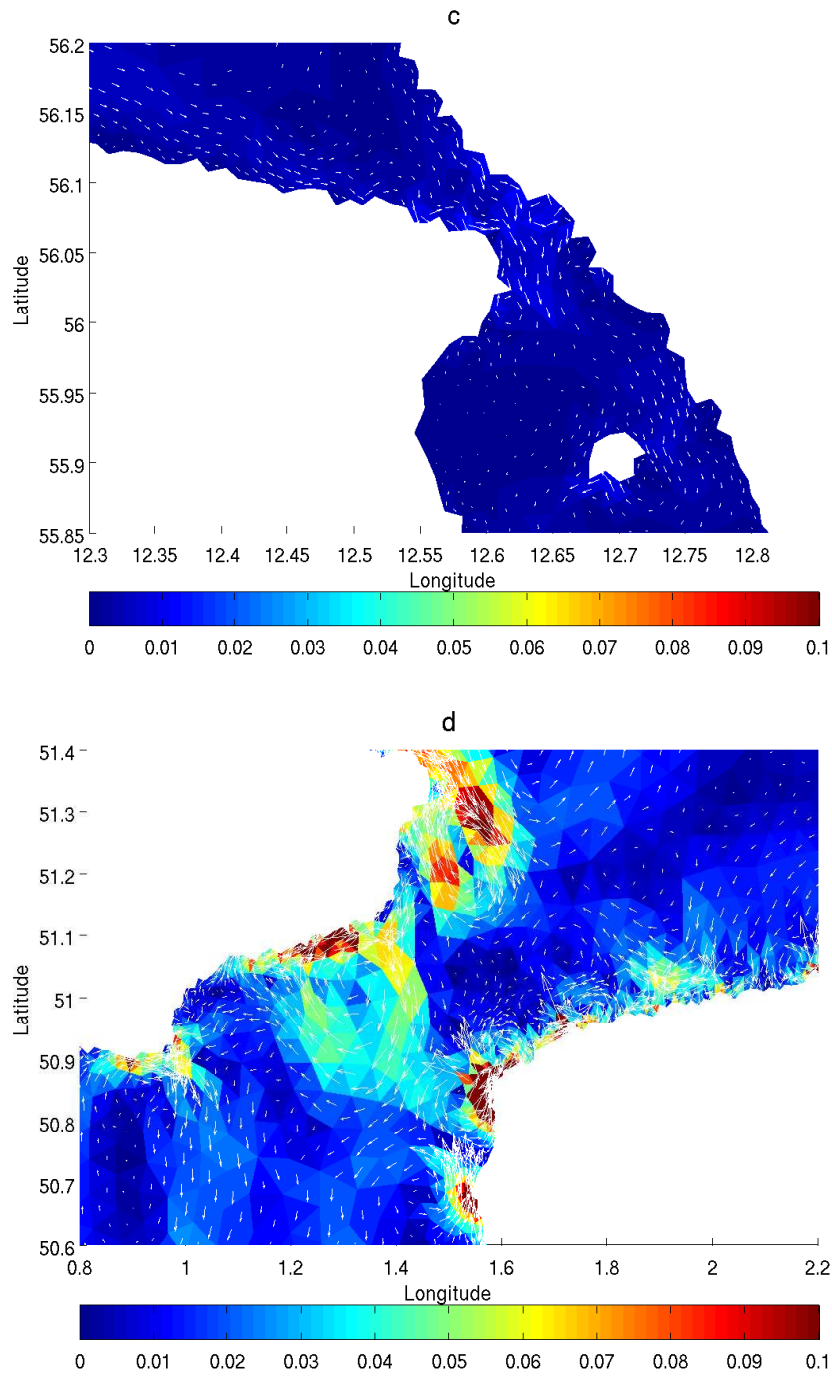


Figure 2.17:  $M_2$  tidal residual currents in m/s: c) Øresund near Helsingborg, d) Strait of Dover.

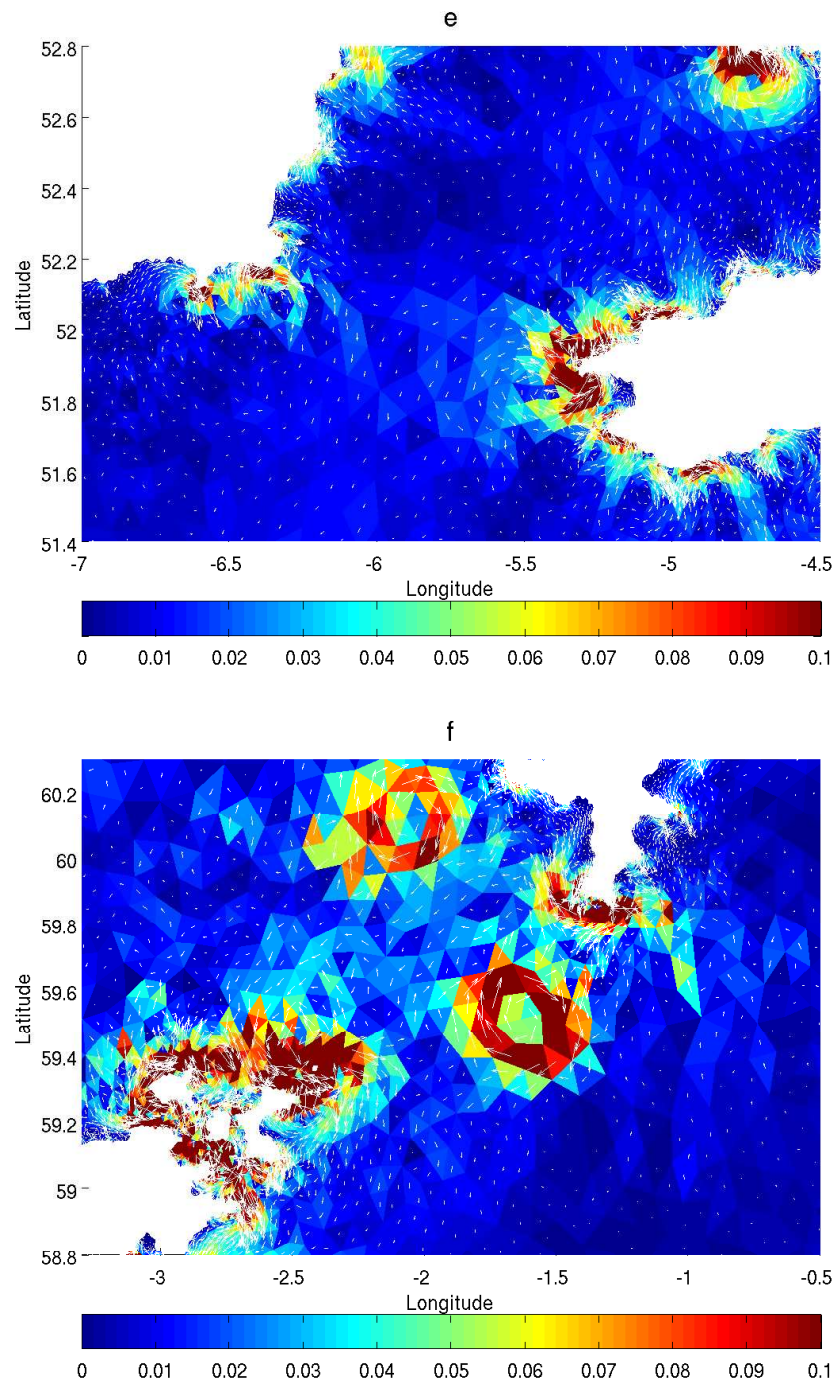


Figure 2.18:  $M_2$  tidal residual currents in m/s: e) St. George Channel, f) Shetland Islands.

ditions. Picture (d) of Fig. 2.17 show the complex tidal residual currents in the Strait of Dover. Again due to the rather coarse resolution, the complicated eddy pattern may still change when the mesh is refined in this region. With this mesh the model has strong currents along the coastline and an anticlockwise eddy at the English coast. There are strong off and on shore currents making it rather difficult to identify an in- or outflow of the North Sea into the English Channel. The eddy activity emphasizes the importance of tidal residual currents in this area.

Similar conclusions can be drawn in the Irish Sea, the Celtic Sea, the English Channel and North of Scotland, as there are even stronger residual eddies. Exemplarily picture (e) in Fig. 2.18 presents the residual currents in the St. George Channel between the Irish and the Celtic Sea, and picture (f) the ones around the Shetland Islands and Orkney Islands. Near the Shetland Islands there are strong currents along the coast. Through the North Sound north of the Orkney Islands some waters from the North Atlantic seems to pass through into the North Sea. There seems to be a two strong eddies between Orkney Islands and the Shetland Islands.

Proceeding further southwards from the Shetland Islands along the coast to Aberdeen and Edinburgh, I observe a weak southwards residual current (picture (g) and (h) of Fig. 2.19). This current turns north-eastwards at the latitude of the Norfolk Broads in England joining a residual current coming from the south (picture (i) in Fig. 2.20). As already mentioned this band precedes to Skagerrak.

### Tidal current ellipses

Tidal currents change direction and magnitude over the tidal cycle. I represent this as the major and minor axis of an ellipses in Fig. 2.21. The currents turning anticlockwise are shown in red and clockwise in blue. Along the Norwegian coast and in the north part of the North Sea the current changes clockwise, while it changes anticlockwise at the English East Coast and in the German Bight. Between England and the Netherlands there is a region, where it is again clockwise and further south close to the Strait of Dover it becomes anticlockwise again. The pattern match charts for example in Sager (1963).

Further, in the German Bight there are circular ellipses near the Danish coast and strongly elliptic ones close to the German coast and in the central German Bight. The form of the ellipses and their anticlockwise change is consistent with observations reported in Mittelstaedt *et al.* (1983).

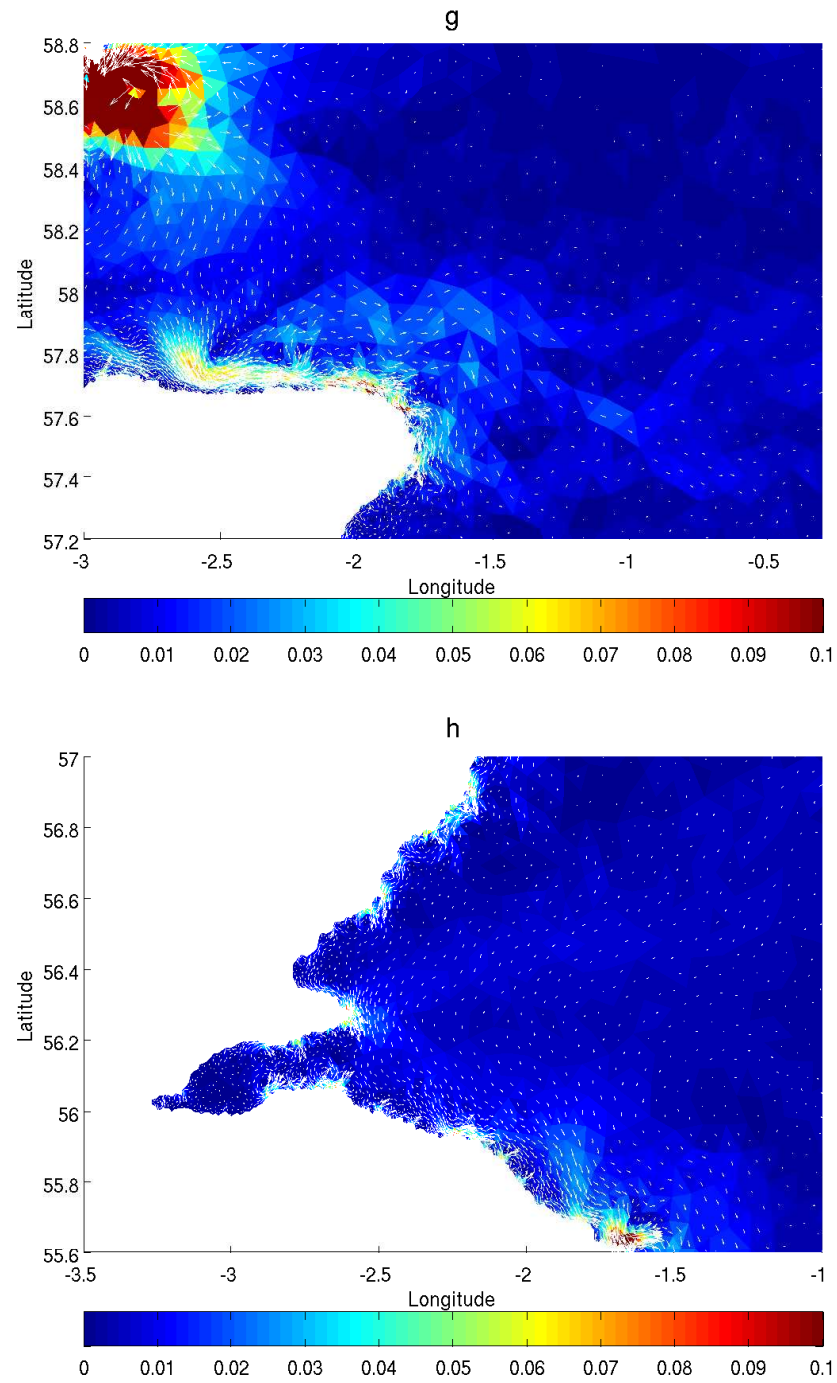


Figure 2.19:  $M_2$  tidal residual currents in m/s: Near g) Aberdeen, h) Edinburgh.

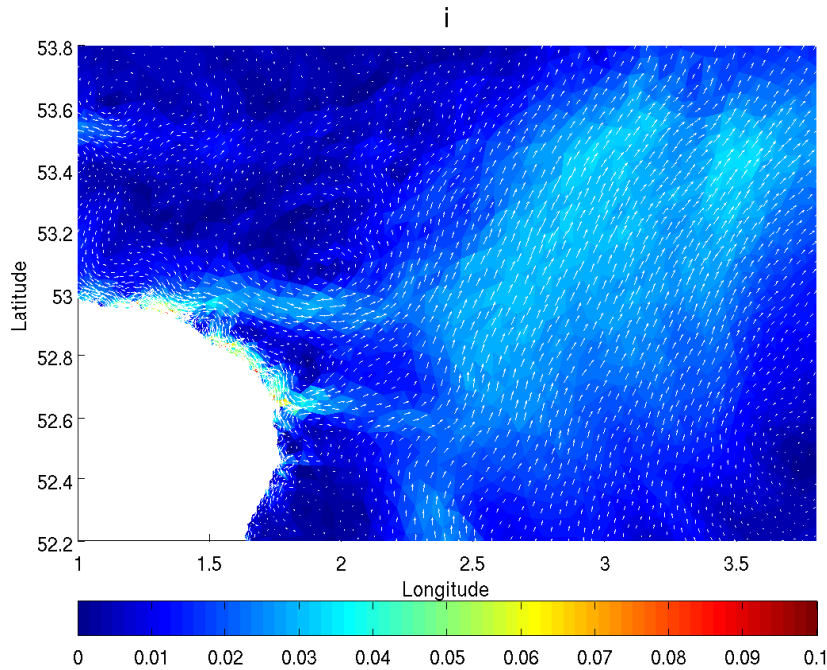


Figure 2.20:  $M_2$  tidal residual currents in m/s: i) West of the Norfolk Broads, England.

### 2.2.3 $K_1$ tidal simulations on the European Continental Shelf

As it has been shown in Section 2.2.1 and in Section 2.2.2 the  $M_2$  tidal wave dynamics are very well reproduced by the models. In this section the  $K_1$  tide will be analyzed and how it is influenced by the open boundary condition. Therefore, I take the NCSI model without potential and no wetting and drying on the European Continental Shelf mesh. Except for forcing the model with the  $K_1$  tide only, the same configurations as in the previous section are applied.

#### Clamped versus Flather

In Fig. 2.22 the amplitude and phase of the simulated  $K_1$  tide is plotted against the observed ones. The clamped boundary condition has been imposed for the plots on the left side and the Flather boundary condition for the ones on the right side. The amplitude is at most stations overestimated. In general the agreement of observed and simulated phase and amplitude is worse compared with the  $M_2$  simulations. While for the  $M_2$  tide the influence of the open boundary condition is small, it is noticeable for the

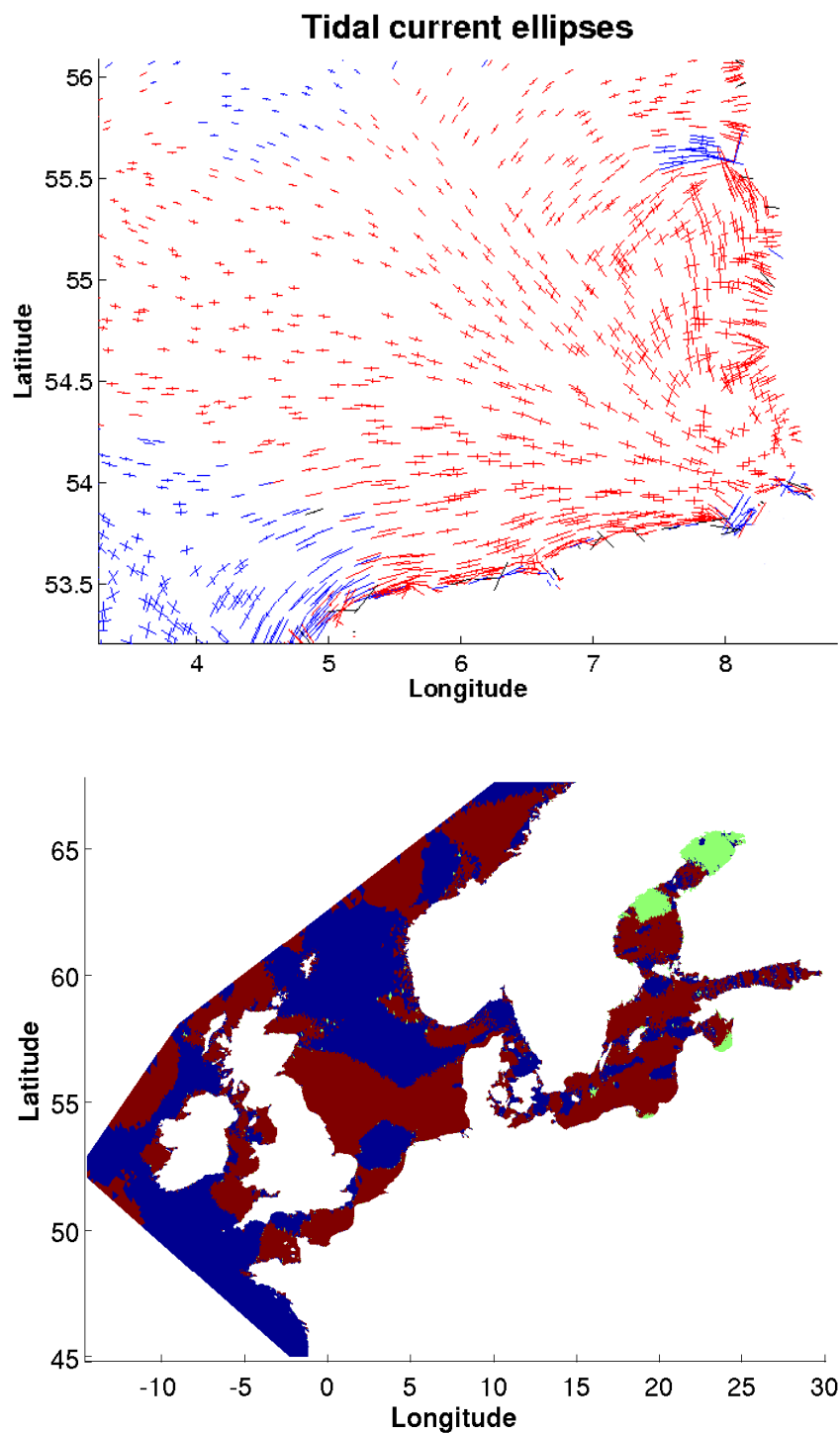


Figure 2.21:  $M_2$  tidal current ellipses: direction of the tidal current changes anticlockwise (red) or clockwise (blue) (with indefinite direction in green). Upper picture: Zoom into the German Bight.

$K_1$  tide. The phase of the  $K_1$  wave remains relatively unchanged using Flather or clamped open boundary condition, but the amplitude tends to be stronger overestimated with the Flather open boundary condition. Although the Flather condition is supposed to give a well-posed problem for the hyperbolic part of the equations, it does not give a better accuracy with this particular mesh and open boundary data.

There are two possible reasons for this behavior. First the velocities at the open boundaries could be too high. The elevation of  $K_1$  is very small compared with  $M_2$  and it may be that the velocity data contain signals from other constituents, too. Second, more energy shall be dissipated by the model for this diurnal tide. Either bottom friction is too low or some energy has to be transferred to compound tides. Probably the interaction between other constituents take an amount of energy. As I introduced only  $K_1$  at the open boundaries and the other constituents are missing in the simulation, no transfer of energy into compound tides can happen.

## 2.2.4 Conclusion

The models introduced in Section 2.1 are tested against data and intercompared with each other. I first compare the seven FE and FV models in their capability to reproduce the  $M_2$  tidal oscillations on an unstructured North and Baltic Sea mesh with clamped boundary condition. All models demonstrate reasonable skills in simulating the  $M_2$  tide in the North Sea. The amplitude and phase are well correlated with the observational data. The amplitude is underestimated by the NC and FV models and overestimated by the P1P1 model.

Further, the P1P1 model shows less realism in some vicinity of boundaries, which can be a consequence of the stabilization employed in this version. The NC models have approximately the same vector and relative errors as the FV models. Those can be mainly attributed to errors at the open boundary introduced by forcing. The FV codes are more robust to open boundary errors but have larger errors in the English Channel than the NC models.

Concerning the computational efficiency, the comparison of the CPU time gives clear preference to semi-implicit codes, as they are much faster than the explicit codes tested here. Among the explicit codes, the FV codes are the fastest. This happens because assembling the right hand sides requires much less operations for the FV discretization used here than for the FE codes. A similar situation is observed with semi-implicit codes, where FVSI was faster if the same time step size is used. In the current implementation the NCSI and P1P1 codes are more stable and, therefore, the reduction of the number of time steps make them faster than FVSI.

This thesis demonstrates quite similar performance of the selected models,

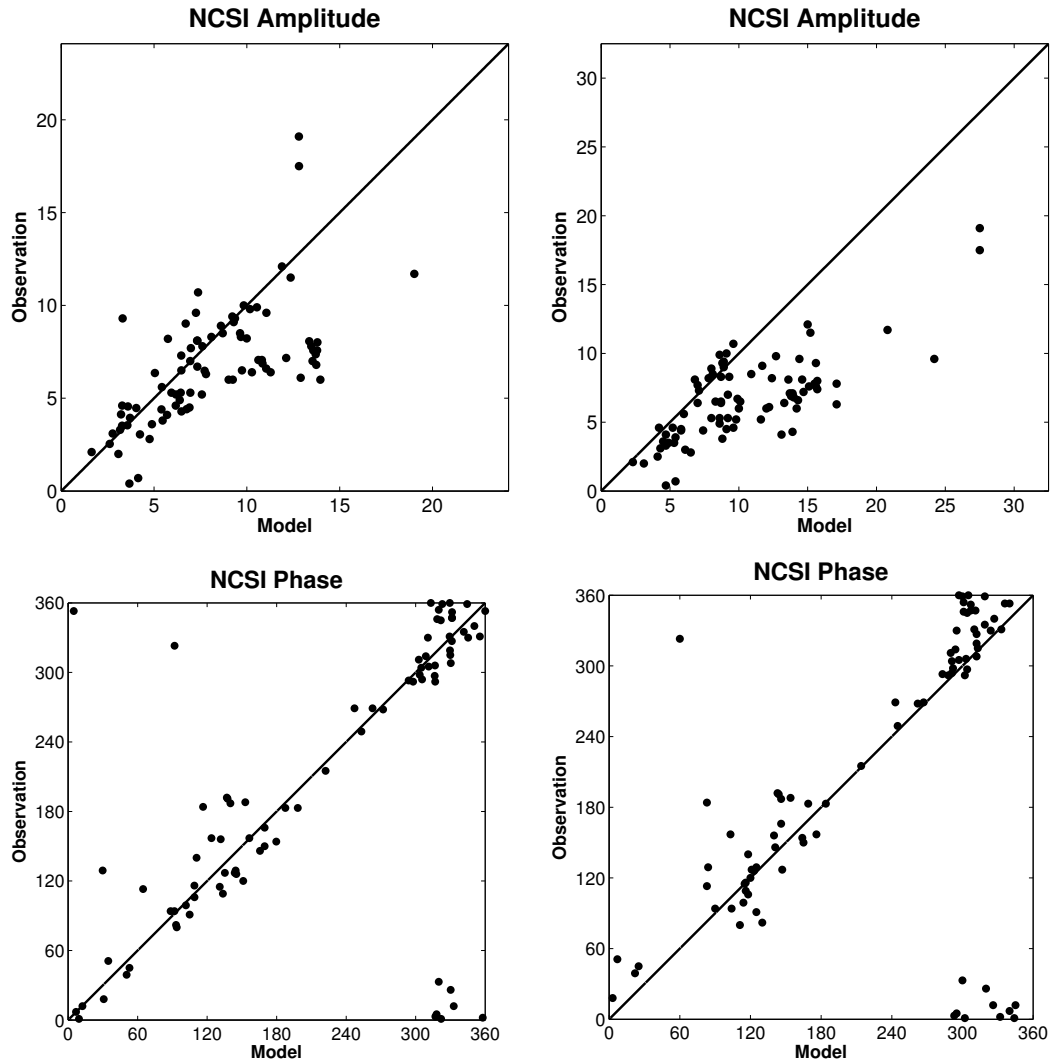


Figure 2.22: Correlation between model and observation of amplitude and phase for the  $K_1$  tide in NCSI model: Clamped boundary condition (left), Flather boundary condition (right)

as well as better numerical efficiency of the semi-implicit FV and NC implementations.

To have a better location of the open boundaries the domain is extended to the European Continental shelf. On this domain NCSI is applied to a finer resolving mesh. The tidal residual currents and the current ellipses of the  $M_2$  tidal wave match well with previous model results and observations. The tides generate a cyclonic circulation in the North Sea. In regions, where complex coastline structures are located, like, e.g., the English Channel or the Irish Sea, strong residual currents are found.

Also the analysis of the energy reveals high reliability of the model. Temporal energy change, fluxes and dissipation have reasonable magnitudes. The residual in the energy balance is of the order of the viscous dissipation. It can be attributed to the way the energy balance has been set up discretely and what kind of simplifications have been made in the implementation. But it also shows, that the energy may be sensitive to the choice of the advection scheme. Leaving errors in the implementation aside, the P1 projection advection method dissipates some energy. Especially, the transport of kinetic energy and the temporal kinetic energy change may be affected by it in this energy balance computation.

The next question is how tidal simulations are influenced by the open boundary condition. For this purpose the Flather and the clamped boundary conditions are tested by simulating the  $K_1$  tide on the fine European Continental Shelf mesh. The Flather condition gave stronger overestimation of the amplitudes than the clamped one. This could be connected to the velocity data or some insufficiently represented processes. Future simulations including all constituents may bring some insight in this issue.

## 3 Adjoint Models

This chapter introduces the general concepts later used in Section 4. First I explain the meaning of the terms “adjoint” and “adjoint model”. The development of the adjoint equations is covered in Section 3.2. Section 3.3 comments on automatic differentiation (AD). Afterwards some examples of adjoint models in oceanography are given and the advantages and disadvantages of their implementation are discussed.

### 3.1 What is an adjoint?

The word “adjoint” is used in many different contexts. For example, the “adjoint matrix” is the conjugate and transposed matrix. It is a special case of an “adjoint operator”. Every linear operator  $A$  between Hilbert spaces  $X, Y$  has an adjoint operator  $A^*$  defined by their scalar products  $(\cdot, \cdot)_x, (\cdot, \cdot)_y$ , i.e.  $(AX, Y)_y = (X, A^*Y)_x$ .

Another context, where the word “adjoint” is used, is with “adjoint equations” and “adjoint models”. An adjoint model is often used in inverse modeling for solving an inverse problem. Abstractly formulated a forward problem consists of evaluating a mapping from the cause to get the effect. Then the inverse problem is to invert the mapping and compute the cause from an effect. For linear problems the inverse mapping is just the inverse matrix, if it exists. An inverse problem is called well-posed, if there exists a unique cause for every effect and the inverse mapping is continuous.

In oceanography inverse problems are often parameter estimation problems, i.e. to fit model results to observations, which are ill-posed. For this purpose a cost function measures the misfit between model result and observation (usually the squared difference plus some penalty on the parameter range or the initial condition). This cost function has to be minimized. Iterative regularization or optimization methods can make use of the gradient of the cost function to find the optimal parameters (see, e.g., Vogel, 2002). Adjoint model calculate this gradient. By setting the gradient of the cost function to zero, one computes the so called adjoint equations with new variables - the adjoint variables - which have to be solved simultaneously with the model equations. The set of equations is called Euler Lagrange equations. The next Section 3.2 will show a detailed derivation of the adjoint equations and in Section 3.4 I give an overview over some adjoint models in oceanography. Some of them use automatic differentiation (AD) and opti-

mization algorithms, while others implement the adjoint equations and solve for adjoint variables in a backward sweep.

The word “adjoint” has also a meaning in context with AD tools. As it will be introduced later in Section 3.3, AD has a forward and a reverse mode to compute the Jacobian. The reverse mode is also called adjoint mode, as the adjoint Jacobian is calculated. During the adjoint code generation adjoint variables are defined to save intermediate results (Giering, 1999). The use of the word “adjoint model” for the source code produced in reverse mode should be avoided. In this case it is not clear, if the adjoint model gives the derivative of the cost function or the Jacobian of the discrete model equations.

## 3.2 The adjoint equations

In this section the adjoint equations are derived. I consider the model  $M : X \rightarrow Y$  as a function between input/control  $X$  and output/state variables  $Y$ .

In case of the shallow water models presented in Chapter 2 the input variables are parameters and initial conditions and the output variables are the velocities and elevations of all timestep.  $M$  is non-linear and likely neither surjective nor injective.

Analogously, the (discrete) shallow water equations may be also written as

$$\chi(x, y) = 0, \quad (3.1)$$

where  $x \in X$  and  $y \in Y$ . Replacing  $y$  with  $M(x)$  and calculating the Jacobian for later use gives,

$$\begin{aligned} \text{Jac}_x \chi(x, M(x)) &= 0 \\ \Leftrightarrow \frac{\partial}{\partial x_i} \chi(x, y) + \text{Jac}_y \chi(x, y) \frac{\partial}{\partial x_i} M(x) &= 0, \text{ for } i = 1, \dots, \dim(X). \end{aligned} \quad (3.2)$$

As there are observations for the state variables  $Y$  and the goal is to determine the corresponding input variables (so invert  $M$ , which is probably an ill-posed problem), the misfit is measured by a cost function  $J$ ,

$$\min_{x \in X} J(x, M(x)), \quad (3.3)$$

which is going to be minimized. This  $J$  is some positive function, e.g., the squared differences. Usually it becomes zero, when the observations and model results perfectly fit, but this is seldom achieved. The necessary condition for its minimum is, that the gradient of  $J$  is zero. Replacing  $M(x)$  with  $y$

and writing the gradient componentwise with respect to the control variables  $X$  gives,

$$\begin{aligned} (\nabla_x J(x, y))^T &= 0 \\ \Leftrightarrow \frac{\partial}{\partial x_i} J(x, y) + (\nabla_y J(x, y))^T \frac{\partial}{\partial x_i} M(x) &= 0, \text{ for } i = 1, \dots, \dim(X). \end{aligned} \quad (3.4)$$

Now I combine Eqn.(3.2) and Eqn.(3.4). Therefore the adjoint variable  $w$  is defined by the following equation,

$$(\text{Jac}_y \chi(x, y))^T w = -\nabla_y J(x, y) \left( = (\text{Jac}_y J(x, y))^T \right). \quad (3.5)$$

Eqn.(3.5) is the equation for the adjoint state, the so called adjoint equation. It may be derived equivalently by using Lagrange multipliers. I multiply the equations  $\chi$  by Lagrange multipliers  $\lambda$  and add them to the cost function, i.e.

$$\tilde{J} := J + \chi^T \lambda.$$

Taking the gradient of  $\tilde{J}$  with respect to the state variables  $Y$  and setting it to zero, gives the adjoint equation (Eqn.(3.5)) with  $w=\lambda$ . The adjoint equations are often derived by using the Lagrange multipliers (see, e.g., Le Dimet & Talagrand, 1986; Sidorenko, 2004). If the derivative of  $J'$  with respect to  $x$  and  $y$  is not taken in continuous but in variational sense and set to zero (see, e.g., Evensen *et al.*, 1998), then the derived equations are also referred to as Euler-Lagrange equations. They include both, the forward and the adjoint equations, which are coupled by  $\lambda$ .

Here the adjoint equations are solved simultaneously for  $w$  with the forward equations (Eqn.(3.1)). Having solved for  $w$  I replace  $\nabla_y J(x, y)$  in Eqn.(3.4) with the expression of the adjoint state (Eqn.(3.5)) and obtain

$$\frac{\partial}{\partial x_i} J(x, y) - w^T \text{Jac}_y \chi(x, y) \frac{\partial}{\partial x_i} M(x) = 0, \text{ for } i = 1, \dots, \dim(X)$$

Now the term  $\text{Jac}_y \chi(x, y) \frac{\partial}{\partial x_i} M(x)$  can be substituted by using Eqn.(3.2). I get for the total derivative of  $J$  (Eqn.(3.4)) denoted by  $J'$ :

$$J' := \nabla_x J(x, y) + (\text{Jac}_x \chi(x, y))^T w (= 0). \quad (3.6)$$

This equation is analogously derived by taking the gradient of  $\tilde{J}$  with respect to the control variables and setting  $\lambda = w$ .  $J'$  becomes zero in the case of optimality for the control and state variables. As long as  $J'$  is unequal to zero, it is used to update the parameters.

Note that the set of Eqns.(3.1), (3.5) and (3.6) is also known as a Karush-Kuhn-Tucker system (see, e.g., Tröltzsch, 2005).

As already proposed by Le Dimet & Talagrand (1986), solving the Euler-Lagrange equations can be avoided by using Eqn.(3.6) with a descent algorithm. As long as  $J$  is simple, for example in case of squared differences to

the observation ( $J = 1/2(M(X) - Y_{obs})^T(M(X) - Y_{obs})$ ), and  $\chi$  is linear or linearized using a simple time-stepping scheme, the adjoint equations are easy to implement. A forward integration in time computes the coefficients of the Jacobian of  $\chi$ . In a backward integration in time the adjoint equations are solved giving  $J'$  (Le Dimet & Talagrand, 1986; Giering & Kaminski, 1998). The adjoint model are sometimes easy to be hand-coded. In other cases, for example if non-linear terms are present, it may be advisable to use automatic differentiation (AD), which will be introduced in the next section.

### 3.3 Automatic differentiation

Automatic differentiation (AD) are computer programs that add statements into existing source codes to compute derivatives. AD tools have two different modes to calculate a differentiated code: a forward (or tangent linear) mode and a reverse (or adjoint) mode. They just differ in the way the derivative is computed and stored. I am going to illustrate both with the following example. Let

$$f : X \xrightarrow{w_1} W_1 \xrightarrow{w_2} W_2 \xrightarrow{w_3} W_3 = Y$$

$$f(x) = w_3(w_2(w_1(x))) =: y,$$

be a function representing for example a model with the operations  $w_1, w_2$  and  $w_3$ . In general  $w_1$  is the identity operation and the derivatives of the operations are trivial or given by some (intrinsic) function. The vectorial function  $f$  maps from some  $n$ -dimensional input space  $X$  (variables such as bottom topography or friction coefficient) into the  $m$ -dimensional space  $Y$  (for example velocity and elevation). Using the chain rule the corresponding derivative writes as

$$\frac{\partial f_i}{\partial x_j} = \frac{\partial f_i}{\partial w_3} \frac{\partial w_3}{\partial w_2} \frac{\partial w_2}{\partial w_1} \frac{\partial w_1}{\partial x_j}, \text{ for } i = 1, \dots, m \text{ and } j = 1, \dots, n$$

One can also express it in matrix form with the help of the Jacobian, namely

$$\text{Jac}_x(f) = \text{Jac}_{w_3}(f) \circ \text{Jac}_{w_2}(w_3) \circ \text{Jac}_{w_1}(w_2) \circ \text{Jac}_x(w_1),$$

where the Jacobians differentiate with respect to their index. Here  $\text{Jac}_x(w_1)$  resp.  $\text{Jac}_{w_3}(f)$  is the identity  $n$  by  $n$  resp.  $m$  by  $m$  matrix.

In the forward computation the derivative  $\frac{\partial f_i}{\partial x_j}$  is therefore obtained by the following lines in the code,

$$\begin{aligned} w_1' &:= \frac{\partial w_1}{\partial x_j} \\ w_2' &:= \frac{\partial w_2}{\partial w_1} \cdot w_1' \\ w_3' &:= \frac{\partial w_3}{\partial w_2} \cdot w_2' \\ w_4' &:= \frac{\partial f_i}{\partial w_3} \cdot w_3' \end{aligned} \tag{3.7}$$

with  $\frac{\partial f_i}{\partial x_j} = w_4'$ .

The reverse mode starts from the left. Having the following lines in the code,

$$\begin{aligned}\bar{w}_4' &:= \frac{\partial f_i}{\partial w_3} \\ \bar{w}_3' &:= \bar{w}_4' \cdot \frac{\partial w_3}{\partial w_2} \\ \bar{w}_2' &:= \bar{w}_3' \cdot \frac{\partial w_2}{\partial w_1} \\ \bar{w}_1' &:= \bar{w}_2' \cdot \frac{\partial w_1}{\partial x_j}\end{aligned}\tag{3.8}$$

and  $\frac{\partial f_i}{\partial x_j} = \bar{w}_1'$ , the derivative  $\frac{\partial f_i}{\partial x_j}$  is computed. The reverse mode is often also called the adjoint mode, since it computes the transposed Jacobian

$$(\text{Jac}_x(f))^T = (\text{Jac}_x(w_1))^T \circ (\text{Jac}_{w_1}(w_2))^T \circ (\text{Jac}_{w_2}(w_3))^T \circ (\text{Jac}_{w_3}(f))^T.$$

Mathematically the reverse and forward mode bring absolutely the same result, but in the reverse mode one needs, for example, to know the value of  $w_2$  to compute  $\bar{w}_3'$ . This means that first the values have to be computed and in a reverse step the derivatives are computed. This is more expensive than the forward mode, where the derivatives are computed in the forward sweep as well. So the question arises, when to use this concept of reverse derivative computation. The answer is related to the dimension of  $X$  and  $Y$  and I illustrate it with the following reformulation.

Expressing the result in Eqns.(3.7) for the forward mode in matrix formulation with the Jacobian matrix  $F_{ij} := (\text{Jac}_x(f))_{ij} = \frac{\partial f_i}{\partial x_j}$  and  $\dot{x} := \frac{\partial w_1}{\partial x_j}$  (so  $\dot{x}$  is just the  $j$ -th unit vector), the following is obtained:

$$F(x) \cdot \dot{x}\tag{3.9}$$

The  $i$ -th line contains the results from the forward steps (Eqns.(3.7)).

In the reverse mode with  $\dot{y} := \frac{\partial f_i}{\partial w_3}$ , which gives the  $i$ -th unit vector, the result from Eqns.(3.8) writes as

$$\dot{y}^T \cdot F(x),\tag{3.10}$$

where the  $j$ -th column gives the desired result here.

If the dimension of  $X$  is smaller than the dimension of  $Y$ , the matrix times vector multiplication is less expensive in Eqn.(3.9) than in Eqn.(3.10) and in this case the forward mode is more efficient. If dimension of  $Y$  is smaller, the reverse mode has less operations and is therefore faster.

Since I want to compute  $\text{Jac}_x(J(x, M(x)))$ , the dimension of  $Y$  is the dimension of the cost function, which is one. Therefore, the reverse mode should be used. If the dependency of  $J$  on  $x$  and  $y$  is simple, one may also automatically differentiate the model only and use

$$\text{Jac}_x(J(x, M(x))) = \text{Jac}_x(J(x, y)) + \text{Jac}_y(J(x, y)) \circ \text{Jac}_x(M(x)).\tag{3.11}$$

When the AD tool differentiates with respect to  $y$ , it decomposes in the same way. Therefore, the same derivatives or sensitivities will be obtained. I just mention it to show that the sensitivities of the model to the input variables are also computed in the reverse model run.

### 3.4 Adjoint models in oceanography

Inverse problems are frequent in oceanic applications. They originate from insufficient measurements for parameter determination and from the incompleteness of ocean model equations in terms of reflecting the physical reality. The result is a misfit between observation and model simulation. But information for the model configuration can be drawn from the observations (Bennett, 1992). As explained above, one way for error minimization is the implementation of an adjoint model. Other data assimilation techniques, for example statistical methods like SEEK (Pham *et al.*, 1998), are not the scope of this thesis and will not be considered, therefore.

The adjoint equations are either derived from the continuous equations and discretized afterwards or computed directly from the discretized equations. By applying the rules for analytical adjoint operators (see, e.g. Schröter, 1989) the adjoint equations can be constructed from the non-discretized model equations. One has to be careful when discretizing these equations, as the descent direction of the discretized error has to be calculated. To be precise: The discretized adjoint equations have to be the adjoints of the discretized model equations.

A common way to get discrete adjoint equations is by using Lagrangian multipliers with the discrete model equations and solving the Euler-Lagrange equations (see, e.g., Evensen *et al.*, 1998). Depending on the complexity of the model, coding these equations can be more or less expensive and cumbersome. I call it the hand-coded or manually differentiated (MD) adjoint method. It was used for example in meteorology by Courtier & Talagrand (1990) or in oceanography by Tziperman *et al.* (1992). Further examples of adjoint ocean models are Tziperman & Thacker (1989) and the citations therein. In ocean models the control variables are, for example, initial stream function, lateral friction or windstress. The misfit of the model output to satellite measurements was used by Schröter *et al.* (1993).

Hand-coded adjoint models have been implemented and used for various applications in coastal oceanography, too. Lardner *et al.* (1993) and Das & Lardner (1992) optimized bottom friction and water depth in tidal simulations with a finite difference 2D shallow water model. Ten Brummelhuis & Heemink (1993) extended the parameter estimation to wind stress coefficients and open boundary values and applied it to a finite difference model on the European continental shelf.

Furthermore, Heemink *et al.* (2002) presented results of a finite difference 3D shallow water model on curvilinear coordinates for the same region. For the gradient computation they neglect the advection and horizontal viscosity term. This affects the inverse computations in very non-linear estuarine flow and may cause slower convergence of the estimates. They state further that

the AD methods have not been successful so far, as the original model is very complex. But the fact that complex codes are not problematic has been demonstrated in the MITgcm (Marotzke *et al.*, 1999).

Taguchi (2004) showed recently that adjoint and direct methods are well suited to solve inverse problems for non-linear shallow water tidal models in coastal seas. He compared direct explicit (EDV), direct semi-implicit (IDV) and adjoint semi-implicit (IAV) methods in reducing the error in  $M_2$  overtide simulations in the Irish Sea. He further concluded that IAV has a relatively high computational burden and favored the direct methods.

Systematic calibration of tidal open boundary phase and amplitude, bottom friction and depth has also been done by Verlaan *et al.* (1996) in a European shelf model. A FD shallow water model and its hand-coded adjoint computed gradients of the cost function. The minimization was done iteratively by the BFGS method. They divided the region into 9 rectangles or triangles to reduce the number of control parameters. This was done as the number of observations was considerably smaller than the degrees of freedom in the parameters. They first tuned amplitude and phase of the open boundary forcing, then depth and finally the Chezy bottom friction coefficient  $C$  (the relationship between  $C$  and the bottom friction coefficient  $r$  is given by  $r = g/C^2$ ). The major issue was to define the rectangles or triangles according to the sensitivities and to smooth the transition of the parameters at the edges to avoid wave reflections. Penalty terms to force the control variables to stay close to some initial guess were additionally needed. The inverse estimation of boundary conditions in the context of the shallow water equations has also been studied (amongst others) by Navon (1985), Shulman *et al.* (1998), Heemink *et al.* (2002), Zhang *et al.* (2003) and Yang & Hamrick (2005).

In oceanography the generation of an adjoint model with the help of automatic differentiation (AD) became popular with the availability of AD tools such as TAMC/TAFF (Giering, 1999). Especially, as the influence of the input variables on the cost function is traceable in numerical models and, therefore, directly differentiable with AD programs. AD tools exist for many common programming languages such as Fortran or C (see the website [autodiff.org](http://autodiff.org)). With the derivative at hand optimization algorithms can change the input variables. With the new parameters the time-stepping models calculate new state values (here in this thesis for example elevation and velocity). One example for an adjoint ocean model generated by AD is the MITgcm (Marotzke *et al.*, 1999).

The creators of TAFF propose a short way to compute the gradient of the cost function, if it is the squared difference between model results and data (Giering & Kaminski, 1998). They argue that if the mapping between the input parameters and the state variables is sufficiently regular, one could use

a linear relation between the input and output variables. The gradient of the cost function is computed as the product between the linear adjoint model (the transposed Jacobian of the model) and the misfit. This is actually a special case of the more general approach in Section 3.2.

Examples of adjoint shallow water models using AD for tidal application in coastal application are rare in literature. In CFD the usage of automatic differentiation is more common.

If the differentiation of the cost function or the model is for any reason not feasible, it is possible to split the computation of model and cost function derivatives (see Eqn.(3.11) or e.g. in Errico, 1997) and only use AD for some part. For shape design and mesh optimization, Dervieux *et al.* (2005) implemented the adjoint equations by hand and used AD only for  $\frac{\partial}{\partial x_i} J(x, y)$  and  $\frac{\partial}{\partial x_i} \chi(x, y)$ . He argued that it is not guaranteed that fixed point iterations in the forward sweep converge also in the backward sweep (which computes the derivatives). If there was any fixed point iteration, it would not be recommendable to use AD to directly compute  $J'$ . Actually, the development of AD tools is steadily advancing and in some AD tools directives to treat fix-point loops are already available. Therefore, it is likely that AD will become more and more frequent to generate adjoint models if open source projects like OpenAD become mature.

One rarely addressed question is the accuracy and efficiency differences between hand-coded and AD adjoint models. Elizondo *et al.* (2002) compared the performance between manually differentiated (MD) and automatic differentiated (AD) code of a 2D non-linear, diffusion type equation model. The MD code outperforms the AD codes in terms of computational efficiency, but in accuracy AD codes are better. This demonstrates, that the choice and the version status of the AD tool is important for the success of AD adjoint models. A comparison of different AD tools (OpenAD, Tapenade, TAFF, etc) to produce adjoint ocean models is not known to the author and is certainly an issue that should be addressed in future.

### 3.5 Conclusion

The adjoint approach has been used to solve inverse problems for ages. In this section I gave the general definitions of adjoint models, adjoint equations and inverse problems. Although adjoint models are frequently used in oceanography, they are not free of shortcomings. If the gradient of the cost function is zero, it does not mean that the minimum is reached. It may also be a maximum or a saddle point or some local minima. In this respect it does not matter, whether the adjoint model solves for the adjoint variables

and uses them to compute the derivative of the cost function, or if it directly computes the derivative of the cost function with respect to the control variables. Actually, the way how the adjoint model is realized - with AD or not - does not matter, too. At best, a necessary condition for the minimum is fulfilled.

The advantage of the adjoint model is its use for sensitivity analysis. Instead of varying each parameter and determining the influence on the results, it is possible to get the sensitivity of the parameters on the cost function in one single run. If the cost function is restricted to a certain area or point, the influence of the parameters on this point can be given. Actually, what is used, is the derivative of the cost function with respect to the control variables. There are many ways to use an adjoint model for the inverse estimate of parameters. Two issues have to be of major concern. First the optimization procedure should be flexible, such that further model development can be easily incorporated into the parameter optimization. AD is one method that is very promising, as it generates the differentiated code without much user input. Second the inverse estimate of parameters should be able to handle a large number of unknowns and still be computationally fast. Adjoint models are computationally expensive, as the computational time increases at least by a factor of two to compute the derivative. AD makes use of so called checkpointing and, therefore, an optimal partition between recalculation and storage of variables is easy to include. The problem of relatively high computational cost still exists. A careful coding of the model is necessary and its practicability has to be analyzed.

Hand-coded adjoint models often use the linearized model to speed up the derivative calculations. This option may also be used with AD.

In terms of sensitivity studies the AD model code is clearly of preference compared with the hand-coded adjoint model. Arbitrary complexity of the model and, for example, non-linear terms do not pose big difficulties as long as the correct AD directives are set. The differentiation can be repeated if changes in the forward code are made and "manual" errors due to wrong derivatives are less probable.



## 4 An unstructured mesh, adjoint, tidal model

This chapter shows the results of an unstructured mesh, adjoint model generated by the AD tool TAMC. First, I give a sensitivity analysis of the misfit between observations and model results for the  $M_2$  and  $K_1$  tidal wave. Then the parameters are optimized by using the adjoint model and a Quasi-Newton method for this inverse problem.

### 4.1 Motivation and setup

In Section 2 several unstructured grid models based on the 2D shallow water equations have been introduced. It has been concluded that only some part of their errors is influenced by the spatial discretization techniques (like, e.g., FE or FV). The major part of errors has origins common to all the models. First, the equations are an approximation to the real world and use parametrization of subgrid processes. Second, the mesh spatial resolution and the approximation of bottom topography limit the accuracy of simulations. Finally, the system is defined and forced by its initial and (open) boundary conditions, which are known only approximately.

In this chapter the tuning of friction parameters, as well as bathymetry and open boundary values is addressed. I present solutions of an unstructured grid adjoint model generated by AD and applied to an European Continental Shelf mesh. The AD tool TAMC is applied to the NCLF model. Although the time-stepping of NCLF could be affected by computational modes it has been shown in Section 2.2.1 that in practice it performs almost as well as other models studied here. The advantage is its simple numerical structure, which is free of fix-point iterations and solver calls. This makes it easier to adopt it to the requirements of TAMC.

The tides in the North Sea are mainly the result of incoming waves and their reflections, so the quality of the open boundary data influences simulation results considerably. In Sections 4.4, 4.5 and 4.6 I try to answer questions like, where the model is more sensitive to open boundary values and how these values should be corrected.

Very similar questions can be raised for the model parameters such as bottom friction and bottom topography. The GEBCO one minute bathymetric data is a compilation of various data sources, so its quality does not have to be spatially homogeneous. This is especially problematic when the mesh aims to resolve features which have been smoothed in the GEBCO data set. In order to minimize the simulation error in some region, one should answer the question as to where the bathymetry has to be very accurate. As depth influences wave speed and amplitude, good results owe a lot to a correct topography.

Further, the bottom friction coefficient has to be tuned too. It is largely unconstrained by observation depending on the bottom roughness. As already pointed out by Schwiderski (1984), Taylor (1918) determined a bottom friction coefficient of  $r = 2.6 \cdot 10^{-3}$  by balancing the energy budget in the Irish Sea. But different values were found for example in Bristol ( $r = 1.4 \cdot 10^{-3}$ ) or the English Channel ( $r = 2.13 \cdot 10^{-2}$ ) by Proudman (1952). This shows that a uniform bottom friction coefficient is a poor approximation and that it has to be determined for each region.

Amongst other derivatives the adjoint model gives sensitivities of the cost function with respect to the bottom friction coefficient and, therefore, regions can be identified, in which the bottom friction coefficient needs to be changed and in which direction.

Nicolle & Karpytchev (2007) showed that a variable Chezy coefficient  $C$  for bottom friction (here  $r = g/C^2$ ) decreases the amplitude/phase misfit between model and observation for  $M_2$  and  $M_4$  tides. They used the TELEMAC2D software for solving the shallow water equations and divided their region - the Pertuis Breton - into two domains, one representing mud flats, where the bottom friction was reduced. They had to make several experiments to find the optimal value of the Chezy coefficient. Using an adjoint model to determine the bottom friction coefficient will surely simplify the tuning. I can only guess why they do not use the adjoint model of TELEMAC2D. Possibly the adjoint model only exist for specific set ups and, as it is hand coded, lag the development of the forward model.

After the sensitivity analysis a Quasi-Newton algorithm is coupled to the forward and adjoint model. The mentioned parameters are optimized by minimizing a cost function, which is the misfit between observed and simulated model fields. Note that our inverse problem is probably ill-posed and additionally possesses a large number of control variables, too. Regularization terms in the cost function are important for having a well-defined inverse.

## 4.2 Cost function

I define the cost function under consideration by

$$\begin{aligned}
 J = & \sum_{m=1}^M \left[ (B_m^{obs} - B_m^{mod})^2 + (D_m^{obs} - D_m^{mod})^2 \right] s_p \\
 & + \sum_{n=1}^N \left[ \left( \ln \left( \frac{r_n}{2.6 \cdot 10^{-3}} \right) \right)^2 s_c \right. \\
 & \left. + \left( \frac{1}{\exp(H_{0n} - A_n^{mod} - 1)} \right)^{s_e} s_h \right], \tag{4.1}
 \end{aligned}$$

where  $M$  is the number of measurement points and  $N$  is the number of nodes.  $B$  and  $D$  are the real and imaginary part of the oscillations. Here  $A$  is the amplitude,  $r$  the bottom friction coefficient,  $H_0$  the depth and  $s_p$ ,  $s_c$ , and  $s_h$  are scaling coefficients. The bottom friction coefficient is no more a constant on the whole domain anymore, but given on each grid node.

The first two terms describe the quadratic difference between the real resp. imaginary parts of the model elevation and the observation. I use real and imaginary amplitudes instead of phase and amplitude because the phase error has a discontinuity between  $-180^\circ$  and  $+180^\circ$ , which is problematic according to my experience.

Also the open boundary forcing is written in real and imaginary part of the level oscillations. Together with the depth and bottom friction coefficient these variables will be optimized.

Many adjoint tidal models use the squared difference between the simulated and observed level oscillations for the computation of the cost function. In Eqn.(4.1) I apply the difference between real and imaginary part of single constituents instead. This adds a fast Fourier transform to the forward and backward code. Using the difference between elevations avoids applying a harmonic analysis to extract the tidal constituents after a certain number of time steps and storing the elevation for this computation. If the open boundary is forced with all constituents and tide gauge level oscillations are available, the squared difference between elevations is advisable since it results in a faster performance. However, in my case the observations are given by harmonic constituents. The data from Andersen (2008) contains only  $M_2$ ,  $S_2$ ,  $K_1$  and  $O_1$ . Higher tidal harmonics like  $M_4$  or  $M_6$  are commonly known with less accuracy and on less stations. The observed elevations are then reconstructed from the harmonic constituents. If only a few tidal constituents are given, it is not feasible to compare elevations directly any more. On the continental shelves shallow water tides like  $M_4$  are generated, which have in some parts as high amplitudes as diurnal tides. Then

the misfit between simulated elevation and the one reconstructed from the observed constituents reflects the missing constituents, too, and will, therefore, contain an error.

A second advantage for directly comparing the real and imaginary amplitude of single constituents is that higher harmonics can be weighted stronger, if good measurements exist for some points. The over- and compound tides even depend stronger on the bottom friction coefficient and their amplitudes are smaller than the astronomical tides from which they originate. When the misfit between observed and simulated elevation is computed in the cost function, their influence in the summary tide may be very small and not correctly accounted for in the optimization.

The last two terms of Eqn.(4.1) are a kind of regularization functionals (Vogel, 2002). With the third term I want to ensure that the bottom friction coefficient stays in a reasonable range above zero. For the sensitivity study this term is zero, but it will be used in the optimization in Section 4.6. The last term is a regularization functional, too. It provides a penalty for the case, when the amplitude becomes close to or bigger than the depth. It is necessary since the optimization experiments does not use wetting and drying. One more penalty could be added to account for an a priori error estimate. In general the depth is known with a relatively high accuracy and one may, therefore, penalize depth adjustments, which are higher than 5% of the original depth. However, in my optimization test setup the error of the depth can be very big, since the depth is corrected to be minimally 10m, and therefore the penalty additionally needs to be spatially variable. Experiments related to this issue are left for future studies.

To find the appropriate values for the scaling coefficients  $s_p$ ,  $s_c$  and  $s_h$  requires some experimentation and values will be given within the optimization runs.

Also the shape of the penalty functionals for depth and bottom friction surely may require a deeper analysis in future. My experience is that these penalties are very important for the convergence of the Quasi-Newton method. Many different functions have been tested resulting in the one proposed in Eqn.(4.1). Once the wetting and drying is also differentiated, the depth penalty has to change, since it has to be allowed for dry falling areas. Possible candidates for a new depth penalty is some smoothness constraint or the already mentioned initial estimate constraint. The construction of regularizations is certainly of interest for future studies, but cannot be fully covered with this thesis. It may turn out that more sophisticated regularization techniques of the non-linear inverse theory improve the calculations (see Aster *et al.*, 2005, and the citations therein), but for the moment it is left for future research.

## 4.3 Mesh description

As the optimization is very expensive computationally, it is done on a rather coarse grid. This mesh, as it significantly changes the location of the coastline due to the fact that it does not resolve the dikes, is only useful for testing the algorithm. The constructed depths and friction coefficients are probably not realistic and, therefore, a finer mesh is used for a more detailed description of the sensitivities. The adjoint model is generated by TAMC using the implementation of NCLF model without wetting and drying and with clamped boundary condition. The coarse and the fine mesh of the European Continental Shelf is based on the GEBCO bathymetry and was provided by Sven Harig using the TRIANGLE grid generation software.

### 4.3.1 Coarse mesh setup

The coarse mesh covers the European Continental Shelf consisting of only 7078 nodes and 12783 elements. It is shown in Fig. 4.1, where the red dots indicate the used stations of the observation data provided by Andersen (2008). The edge length varies between 5 and 107 km and allows a time step of circa 99 sec in the NCLF model.

### 4.3.2 Fine mesh setup

The fine mesh consists of 122936 nodes and 219233 elements and it is constructed based on the same GEBCO one minute bathymetry data, that was used for the coarse grid. The minimal edge length is about 386m and the maximal is 7km long. Comparing the coarse (Fig. 4.1) and the fine mesh (Fig. 4.2) the coastline is much better represented by the fine mesh. The used time step size is approximately 7 seconds.

### 4.3.3 Model performance on the meshes

Fig. 4.3 shows the correlation between model and observation in amplitude and phase on the coarse and fine mesh for the  $M_2$  wave only. Each point represents a station shown in Fig. 4.1 for the coarse and in Fig. 4.2 for the fine mesh. A good agreement between model and observation is obtained for the fine mesh, as almost all points lie on the main diagonal. In contrast, the points are considerably shifted from the diagonal in both amplitude and phase on the coarse mesh.

The comparison of the correlation between observed and simulated  $K_1$  tide on the coarse and fine meshes is shown in Fig. 4.4. As the adjoint model has been generated based on the NCLF model, the results differ from the  $K_1$

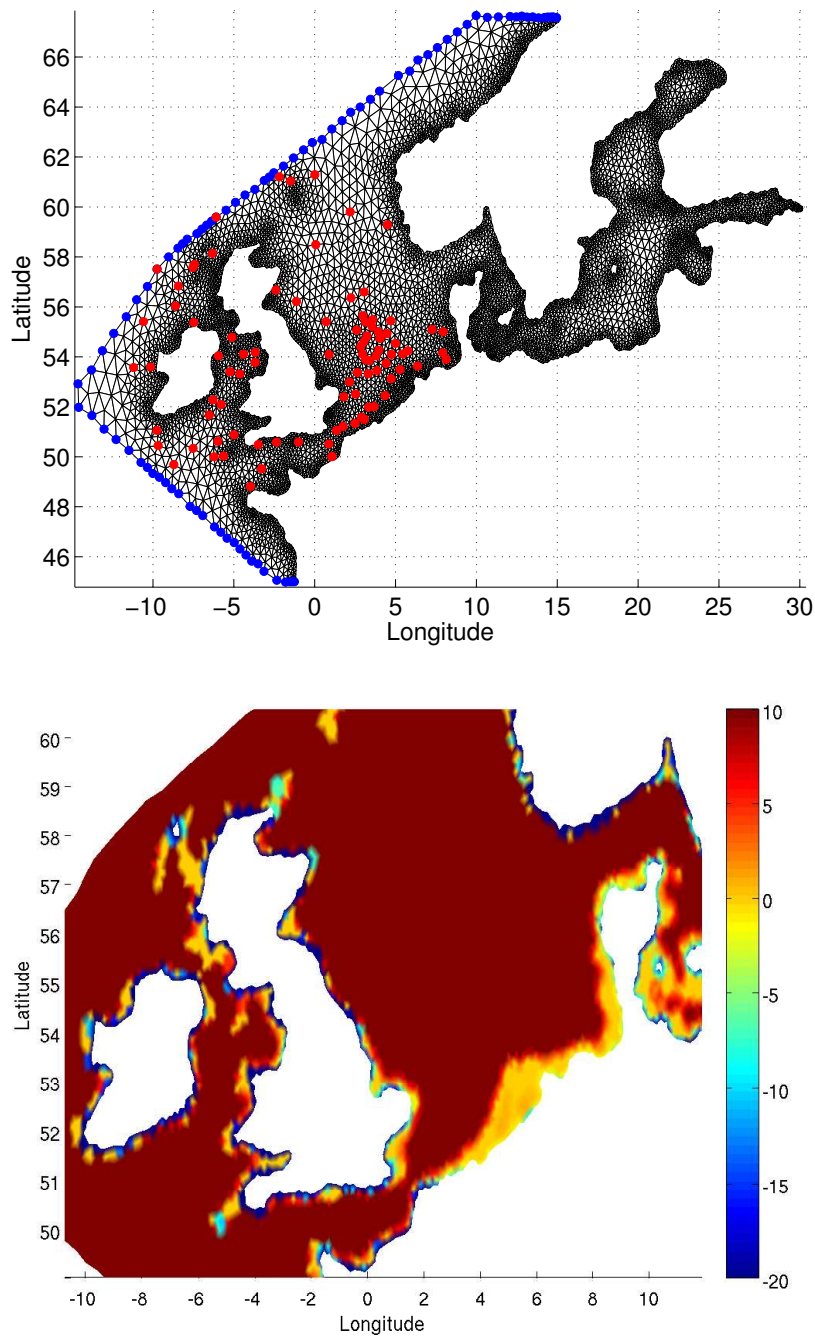


Figure 4.1: Upper plot: Coarse mesh. The red points show the location of the observation data and blue points are the open boundary nodes. Lower plot: Depth in m, no changes in the bathymetry are made in the red shaded area. The rest is corrected for 10m minimal depth.

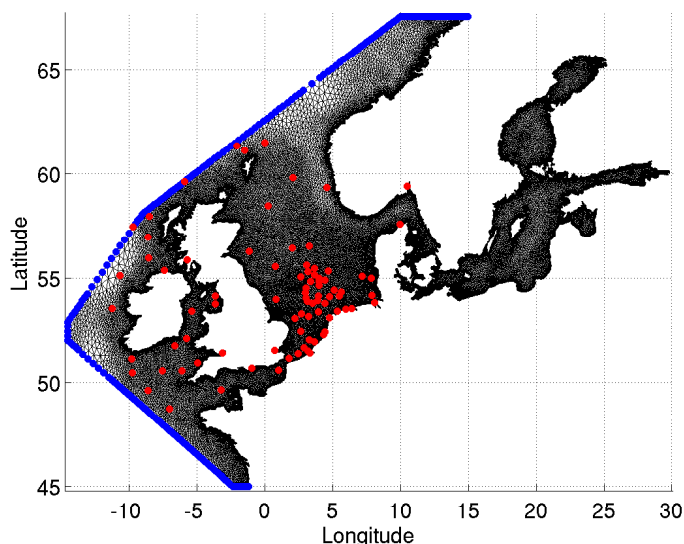


Figure 4.2: Fine mesh used for the sensitivity study. The red points show the location of the observation data and the blue points are the open boundary nodes.

simulations in Section 2.2.3, where NCSI was used (see Fig. 2.22). NCLF uses clamped boundary conditions. On the fine mesh with clamped boundary condition the NCSI model agrees slightly better to the observations than NCLF model here. This can be partly attributed to the weak filtering applied in NCLF to suppress the numerical mode.

Contrary to the  $M_2$  tide simulation with NCLF shown in Fig. 4.3 the  $K_1$  simulations on the fine mesh turns to be worse than on the coarse mesh. In Fig. 4.4 the  $K_1$  amplitudes are partly over- or underestimated on both meshes. For the fine mesh the under- and overestimation is even worse for most of the points than on the coarse mesh. As the phase is in less good agreement on the fine mesh, it is a hint that the amphidromes may have less favorable position as on the coarse mesh. One possible reason is the weak filtering, which is done on each time step. As shorter time steps are used on the fine mesh, the solution will be more affected by the weak filtering.

#### 4.4 Sensitivity studies for $M_2$

For this sensitivity study NCLF is forced by  $M_2$  only and the cost function computes the misfit for the  $M_2$  constituent.

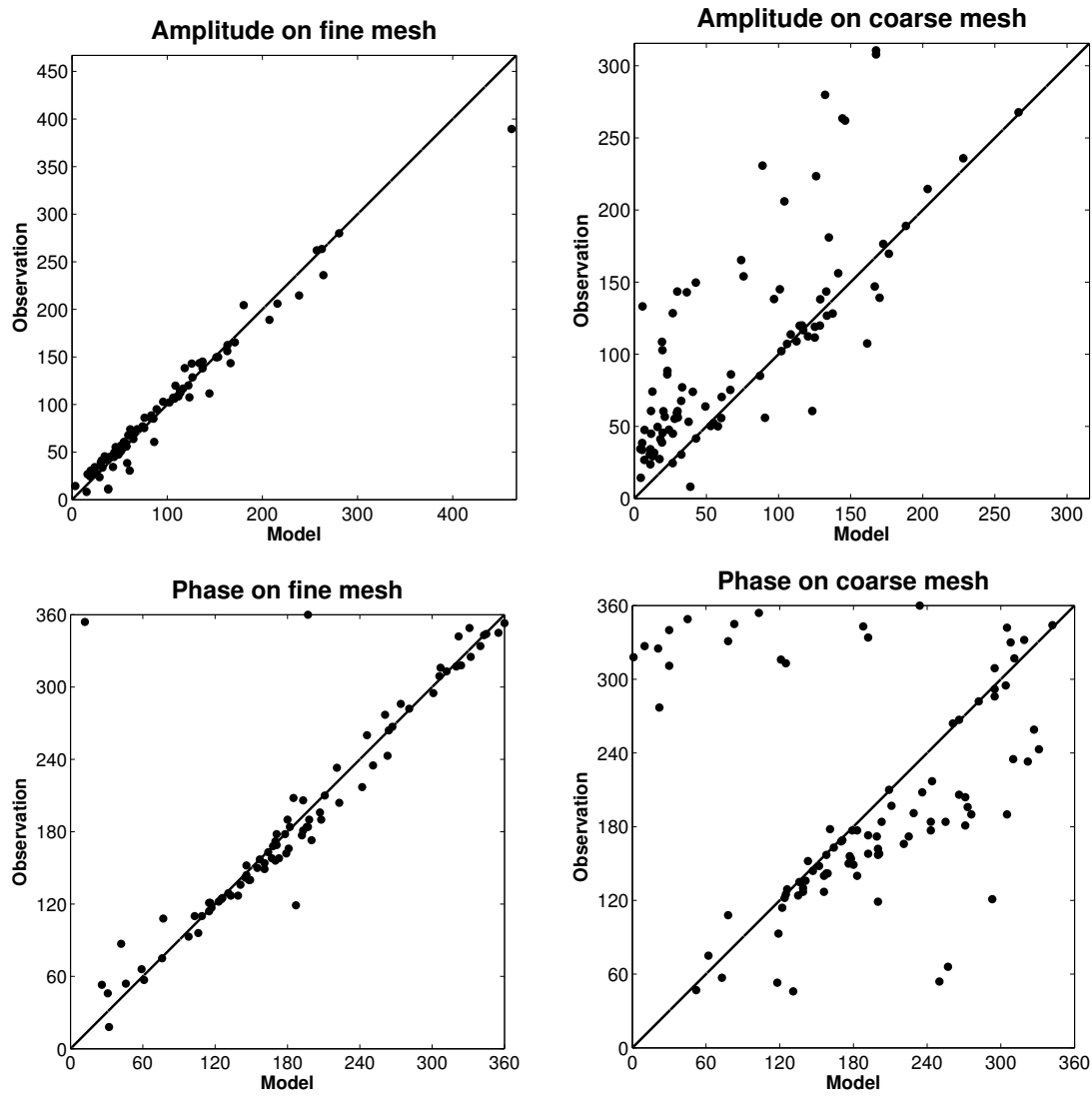


Figure 4.3:  $M_2$  tide: Left: Correlation between observed and simulated amplitude (in cm) and phase (in degree) on the fine mesh. Right: The same but on the coarse mesh.

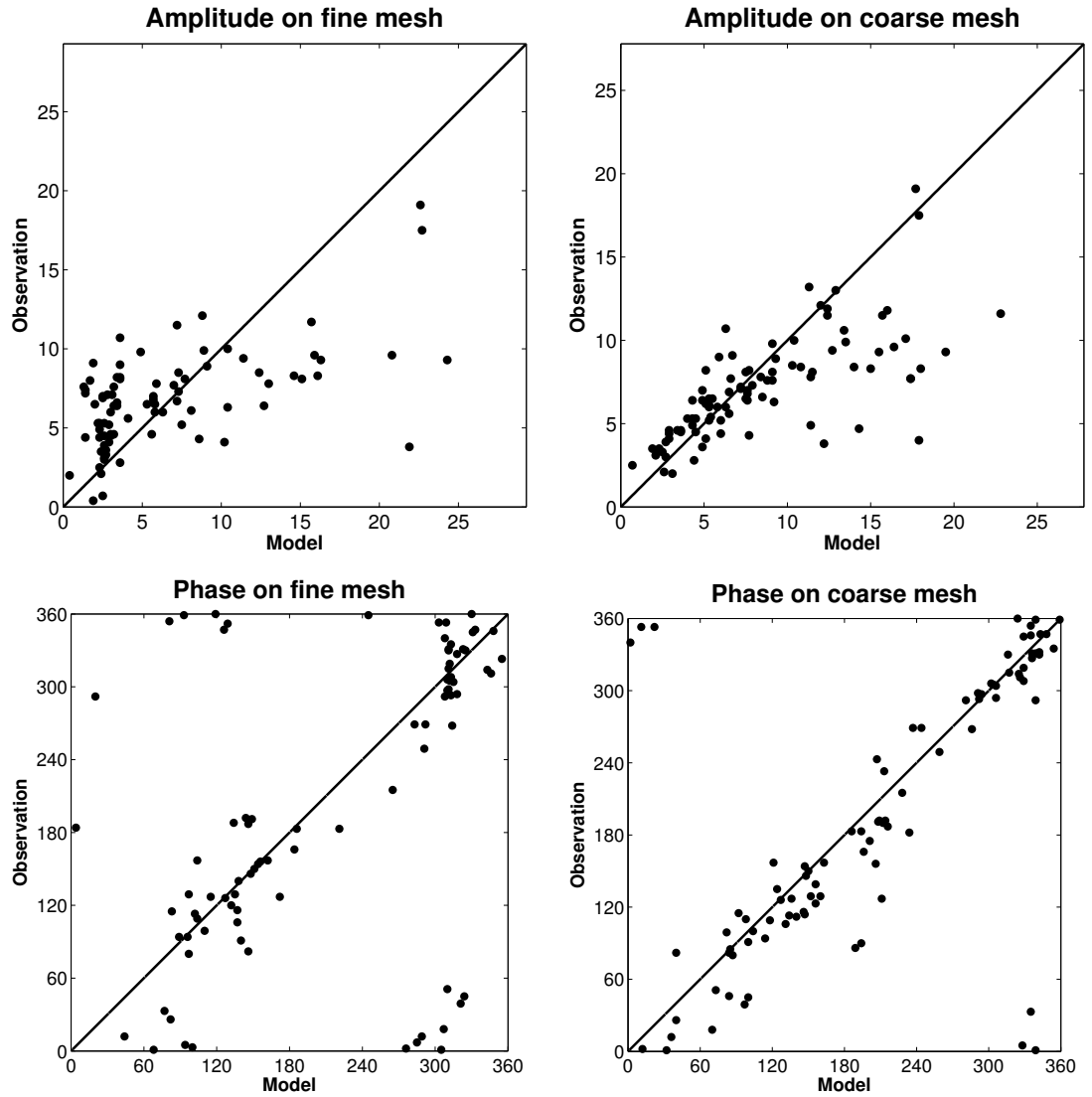


Figure 4.4:  $K_1$  tide: Left: Correlation between observed and simulated amplitude (in cm) and phase (in degree) on the fine mesh. Right: The same but on the coarse mesh.

min, max	coarse mesh	fine mesh
$\partial J/\partial H_0$	-0.0339, 0.011	-0.0021, 0.0006
$\partial J/\partial r$	-41.9707, 29.6194	-2.2571, 2.3522
$\partial J/\partial B$	-2.6857, 0.6406	-0.4842, 0.2195
$\partial J/\partial D$	-1.8519, 0.9602	-0.0588, 0.2463
scaled $\partial J/\partial H_0$	-0.0642, 0.0485	-0.0024, 0.0013
scaled $\partial J/\partial r$	-0.0055, 0.0039	$-2.9343e^{-4}$ , $3.0579e^{-4}$
scaled $\partial J/\partial B$	-0.0332, 0.0296	-0.0065, 0.0022
scaled $\partial J/\partial D$	-0.1179, 0.026	-0.0017, 0.0152

Figure 4.5: Minimal and maximal values of the sensitivities and scaled sensitivities. The units are the inverse of the variable units over which the differentiation is performed, e.g.  $m^{-1}$  or 1.

#### 4.4.1 Sensitivities on coarse mesh

Fig. 4.6 and Fig. 4.7 show the sensitivity of the cost function with respect to depth, the bottom friction coefficient and real and imaginary part of the level oscillations imposed at the open boundaries.

The magnitude of the derivatives are between  $-0.034m^{-1}$  and  $0.011m^{-1}$  for the depth, between  $-41.97$  and  $29.62$  for the bottom friction coefficient and between  $-2.69m^{-1}$  and  $0.96m^{-1}$  for the real and imaginary amplitude. Assuming that the parameters have an error of 5%, the sensitivities can be compared by multiplying the derivatives with 0.05 times the parameter value. For the real and imaginary amplitude the minimal value is  $-0.12$  and the maximal value is  $0.03$ . The bottom friction coefficient has  $-0.006$  and  $0.004$  and the depth  $-0.06$  and  $0.05$ . The values are summarised, together with the values of the fine mesh, in Fig. 4.5. It illustrates that the cost function is a bit more sensitive to the open boundary values than to depth. The sensitivity to the bottom friction coefficient is smaller than the other two.

Note that 5% error is a reasonable estimate for depth and open boundary errors (leaving aside the increased depth due to the restriction of non falling dry areas). But estimates of the bottom friction coefficient show that it can be up to ten times higher than the default value of  $2.6e^{-3}$ . This would mean a sensitivity between the maximal values of  $-1.09$  and  $0.77$ , which is much higher than the other sensitivities. Therefore, the bottom friction coefficient is often used to tune model results closer to observations. However, the resulting bottom friction coefficients may reflect the model's discretization errors, but not the true energy dissipation in the boundary layer over the rough bottom.

In Fig. 4.6 the unscaled derivatives of the cost function with respect to depth and the bottom friction coefficient are shown. Depth sensitivity is negative along the British East Coast, in the English Channel, in the Irish Sea and in

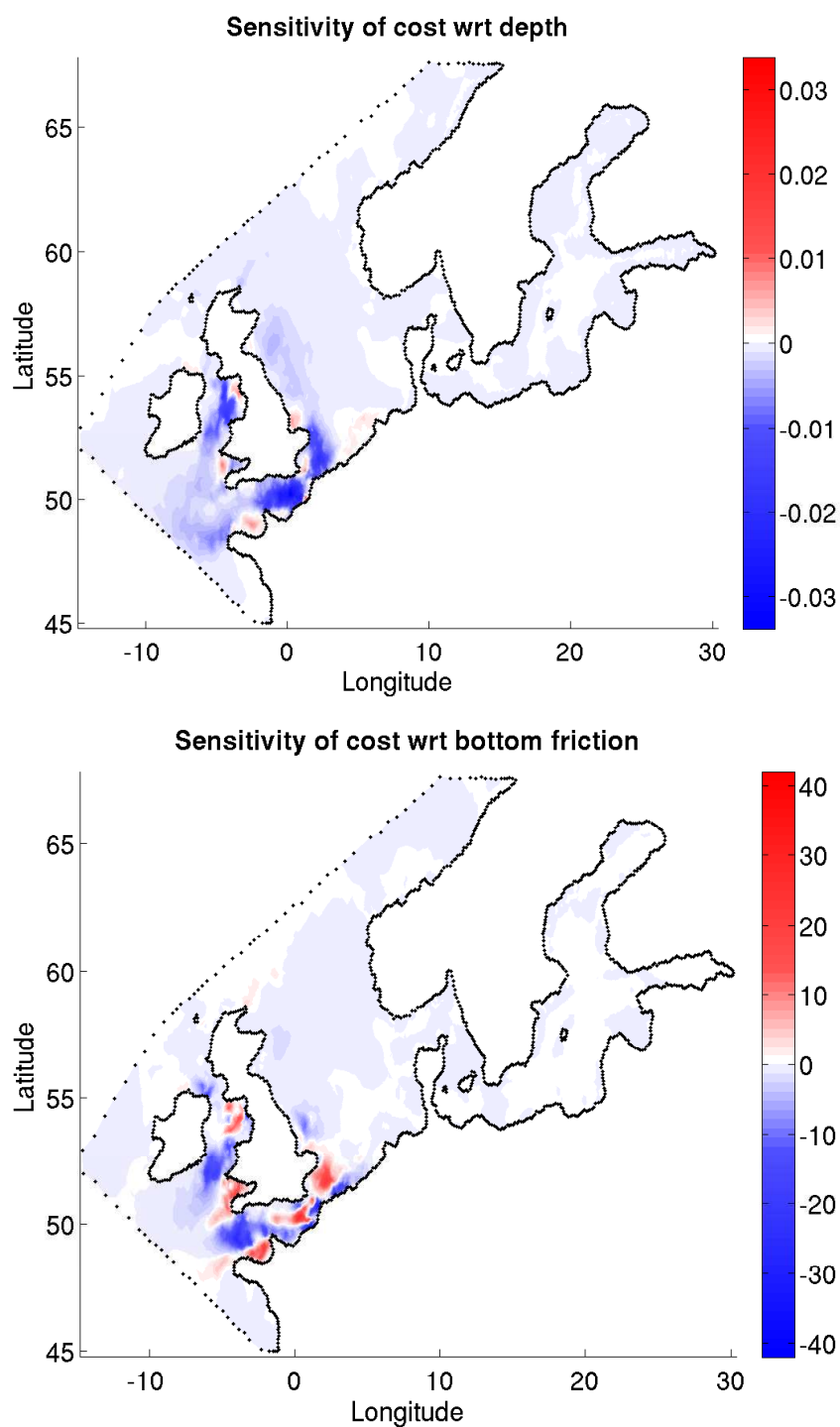


Figure 4.6:  $M_2$  wave: Sensitivities of the cost function on the coarse mesh: With respect to depth (unit is  $m^{-1}$ , upper plot) and the bottom friction coefficient (unit is 1, lower plot).

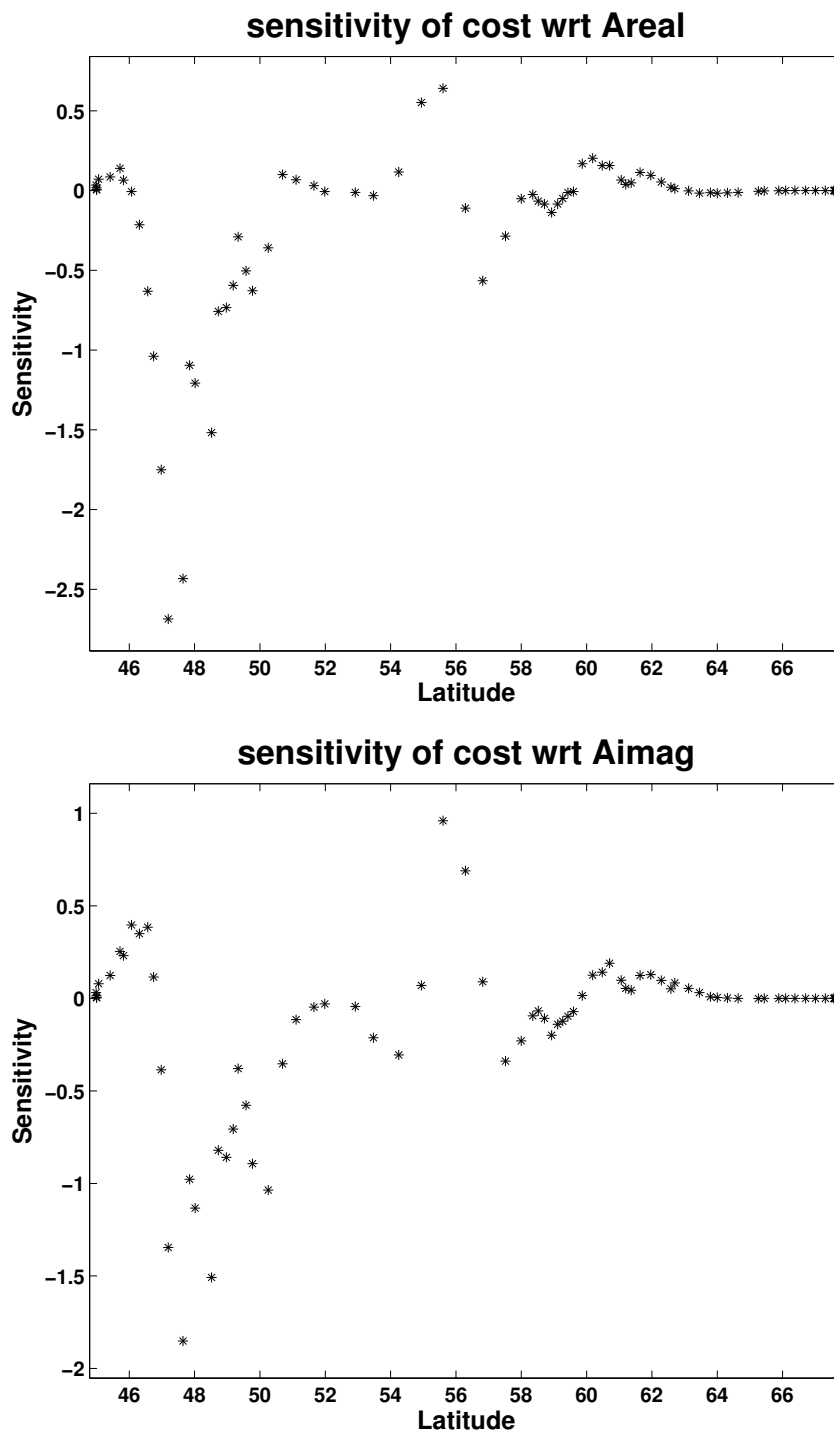


Figure 4.7:  $M_2$  wave: Sensitivities of the cost function on the coarse mesh: With respect to real (upper plot) and imaginary (lower plot) part of the oscillation imposed at the open boundaries (unit is  $m^{-1}$ ).

the Celtic Sea. Small positive spots are located in the Wash, in the Golfe de St.-Malo, in Bristol Channel and east of the Isle of Man. The pattern of the bottom friction coefficient is more diverse. The derivative has positive sign mainly in the Bristol Channel, the Golf de St.-Malo, the eastern part of the English Channel and in some region between the United Kingdom and the Netherlands.

Comparing the sensitivities of the cost function to depth and the bottom friction coefficient in Fig. 4.6, one notices that the values have the same sign in some areas while in others the signs are opposite. For example, in the region between the United Kingdom and the Netherlands the derivative suggests that the bottom friction should be reduced and the depth increased. This means that the value of the bottom friction term decreases and that less energy should be dissipated there, too. Of course, the model also depends on the depth in the continuity equation. Therefore, and since the transport and the wave speed depend on the depth, the patterns do not need to have opposite signs everywhere. In most parts of the area the derivative suggests to increase the depth. Although navigational charts tend to underestimate the depth in deep parts, it is not clear whether the proposed depth changes are closer to reality or just an adaption to mesh and model error.

The pattern of the depth and bottom friction coefficient show the sensitivity is bigger in the English Channel and in the Irish Sea. This is probably because more attention has to be paid for correct depth and mesh resolution in this area.

The derivative of the cost function with respect to the real and imaginary part of the open boundary values at the open boundary (shown in Fig. 4.7) suggest that there are two main areas of influence of the open boundary on the cost function. One is located west of the Breton coast in the Celtic Sea and probably a result of the larger error in the English Channel. The other one is north-west of Ireland with a smaller amplitude. It is located in an area, where continental shelf break is part of the domain. Thus, there is sharp change in depth and it is possible that the tidal wave is just reflected and the open boundary has therefore to be corrected.

To summarize the sensitivities identified regions, where the parameters or the model discretization are not optimal. They suggest a direction and, correctly scaled, also a magnitude in which the parameters should be changed even without applying an optimization algorithm.

#### 4.4.2 Sensitivities on fine mesh

Analogously to the results on the coarse mesh the magnitudes of the sensitivities (shown in Fig. 4.5) suggest, that the model error is more sensitive to changes at the open boundaries when all parameters vary around 5% from their initial guess. As mentioned above the bottom friction coefficient can have much bigger error and then contribute primarily to an improvement of the results.

Further, the sensitivities of the fine mesh are smaller than the ones from the coarse mesh, which can be explained by the smaller initial error in the parameters. Due to the squared difference in the cost function the derivative will always be weighted by the misfit. Consequently if the absolute error is smaller, then the sensitivities are smaller, too.

In Fig. 4.8 and Fig. 4.9 the scaled sensitivities of the cost function to depth, bottom friction coefficient and real respectively imaginary amplitude at the open boundary are shown. As already mentioned scaled means the sensitivity at a node multiplied with 5% of the parameter value (e.g. depth or bottom friction coefficient). Compared with the results on the coarse mesh in Fig. 4.6 the sensitivities have even different signs. The English Channel has positive sensitivities on depth between the Strait of Dover and Cherbourg and negative sensitivities west of Cherbourg. West of Brest is another region of high positive sensitivity. The Irish Sea, Bristol Channel and St. Georges Channel are characterized by a big negative sensitivity on the depth. In the coarse mesh the patterns were consistently negative in parts of the English Channel and the North Sea and in the Irish Sea with some minor positive sensitivities in the Golf de St. Malo, the Wash, the Bristol Channel and east of the Isle of Man. It seems that on the coarse mesh, its interpolated depths at the nodes and the too coarse coastline had a very big influence especially in the English Channel and the Irish Sea and masked real errors in bathymetry away. Similarities between the sensitivity on depth between the coarse and the fine mesh are at the British East coast in the North Sea. Both sensitivities propose that the depth should be presumably deeper than proposed by the bathymetric data.

The sensitivity of the cost to the bottom friction coefficient (see Fig. 4.8) on the fine mesh has more details than the one on the coarse grid (see Fig. 4.6). Some fine structures are observed close to the Strait of Dover in the fine mesh. West of Brest there is a negative sensitivity and combining it with the positive depth sensitivity, I can conclude that the bottom friction term has to increase. More energy is supposed to be dissipated by the bottom friction in this region and a decreasing depth indicates that the wave speed should be reduced. On the other hand this region is close to the open boundary and phase and amplitude error may also be introduced and corrected by it. As shown in Fig. 4.9 the model error is very sensitive to the open bound-

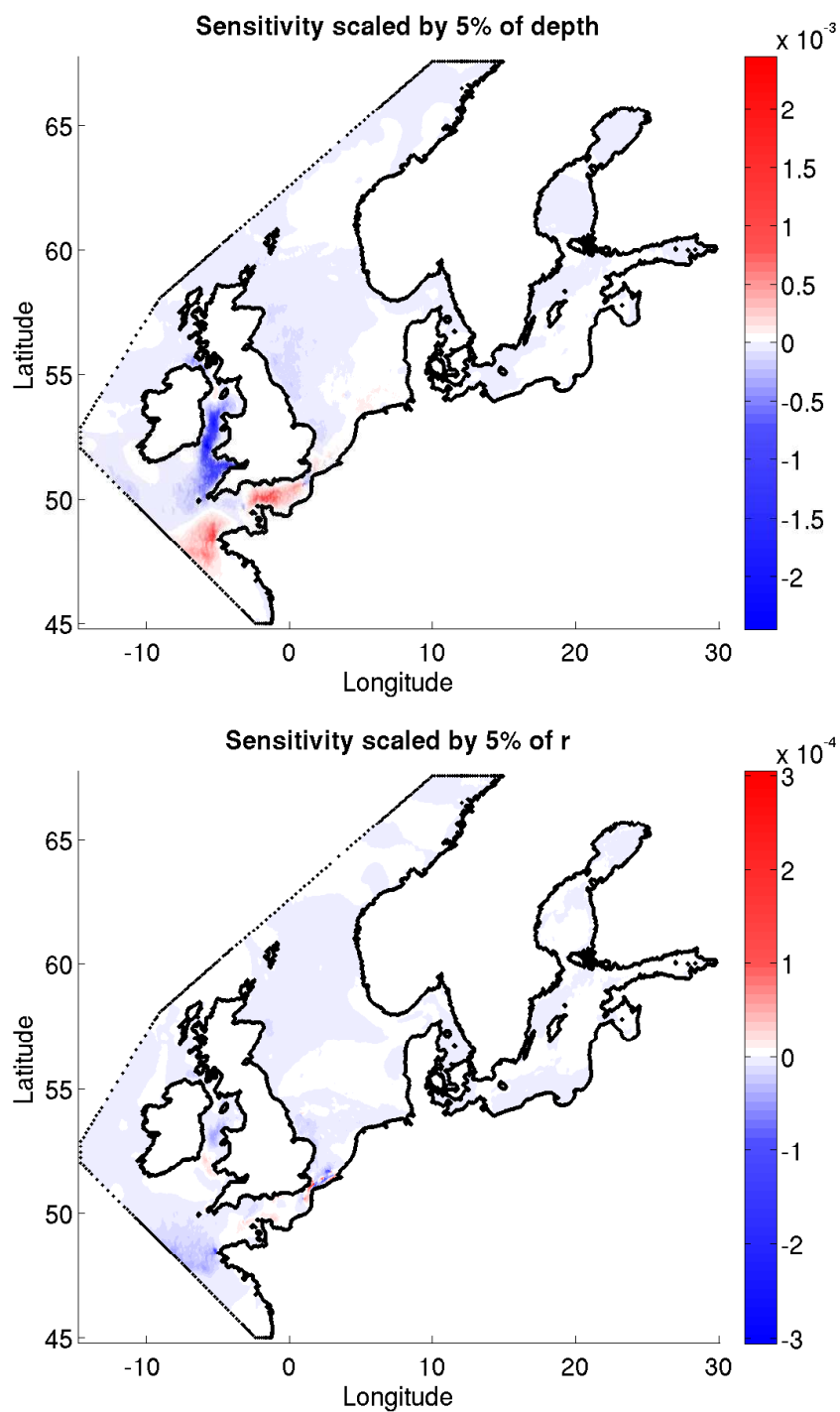


Figure 4.8:  $M_2$  wave: Scaled sensitivities of the cost function on the fine mesh: With respect to depth (unit is 1, upper plot) and the bottom friction coefficient (unit is 1, lower plot).

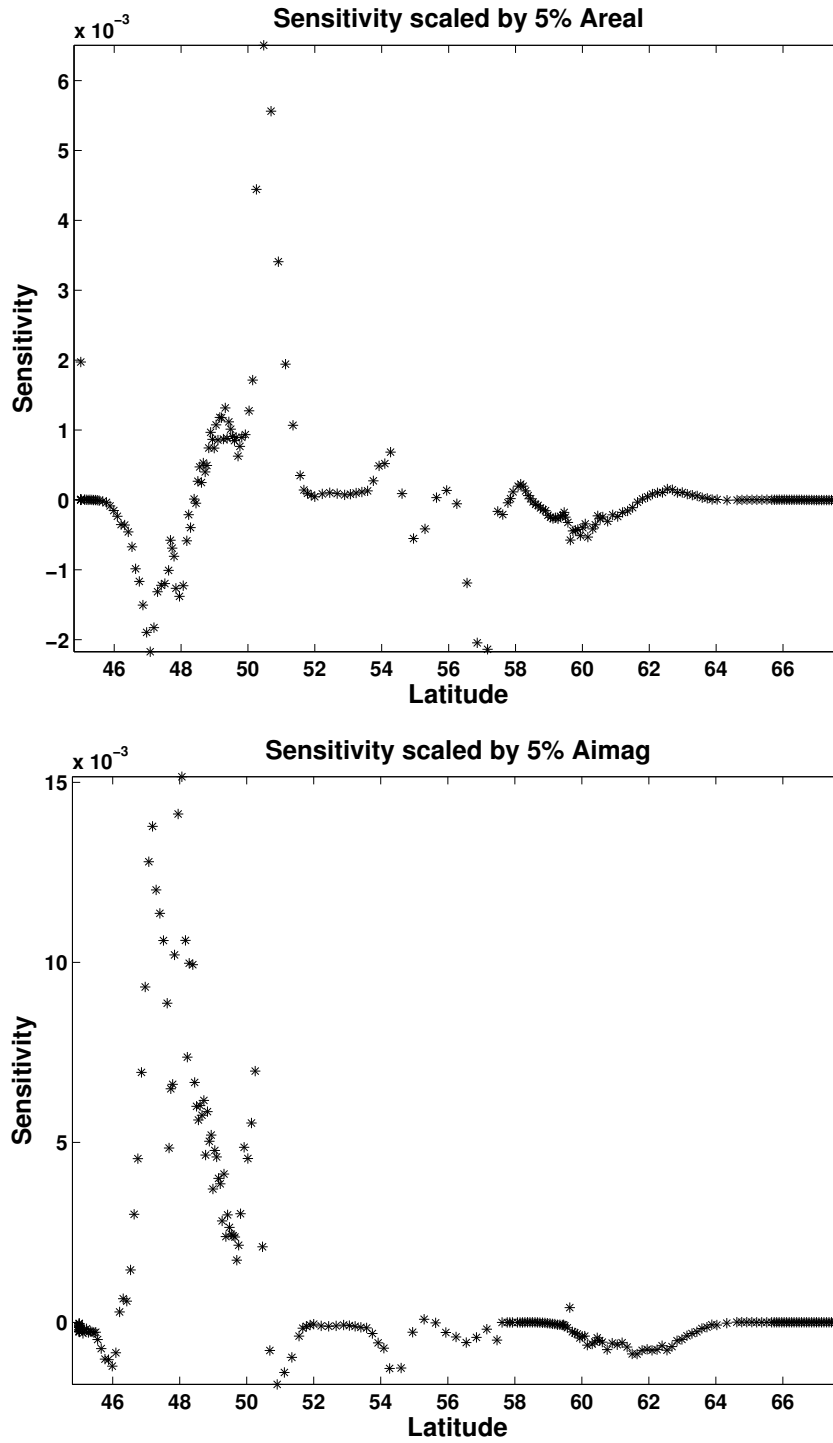


Figure 4.9:  $M_2$  wave: Scaled sensitivities of the cost function on the fine mesh: With respect to real (upper plot) and imaginary (lower plot) part of the oscillation imposed at the open boundaries (unit is 1).

ary between 46°N and 51°N. The wave entering here is the major player in the English Channel and in the Irish Sea. This result is consistent with the sensitivities on the coarse mesh, but the sign of the sensitivity is partially different. Analogously to the coarse mesh another region of sensitivity is also between 54°N and 58°N.

The Shetland and Orkney Islands are partly underwater on the coarse mesh, while they are nicely represented in the fine mesh. On both meshes the open boundary sensitivities show that the open boundary values have to be corrected because of these islands. It may be that islands impose dynamics which are not represented in the open boundary values.

## 4.5 Sensitivity study for $K_1$

The previous section showed the sensitivities of the cost function with respect to the  $M_2$  tidal wave. The question is whether diurnal waves, for example  $K_1$ , produce the same optimized parameters. The goal is to suggest parameters which do not deteriorate the results of other constituents. This may only be possible if the cost function contains the error for other constituents as well.

In the following I will discuss the sensitivities of a cost function that only contains the error to the  $K_1$  observations in a model run forced by  $K_1$  only. This tidal constituent has a very different pattern and so I expect the sensitivities to be different, too.

### 4.5.1 Sensitivity on coarse mesh

The sensitivities of the cost function with respect to depth, bottom friction and open boundary values are shown in Fig. 4.10 and in Fig. 4.11. As the stations coincide with those used for the  $M_2$  sensitivities, the sensitivities cannot differ due to changes in the location of the stations. Note that the magnitude of the cost function and its derivatives are smaller than for  $M_2$ . But not only the derivatives are by factor of 100 smaller, the patterns are different, too. There is a sensitivity signal for depth and bottom friction mainly in the Strait of Dover, near the Hebrides and in the North Channel. Obviously the wrong representation by the mesh and depth values are responsible for it. The sensitivities of  $M_2$  shown in Fig. 4.6 are insignificant near the Hebrides; they are much stronger in the Irish Sea and the English Channel.

The open boundary sensitivities of  $K_1$  (see plots in Fig. 4.11) have peaks around 47°N, 50°N and 56°N. The first and the second peak are positive and located in the Celtic Sea, where a strong negative sensitivity was found

in the  $M_2$  simulations. The third peak is more pronounced than the other two, but of comparable size to the sensitivity in the same region in the  $M_2$  simulation. Once again, the signs do not match completely.

### 4.5.2 Sensitivity on fine mesh

The  $K_1$  sensitivities on the fine mesh (shown in Fig. 4.12 and Fig. 4.13) are by a factor of ten smaller than the sensitivities on the coarse mesh. The sensitivity to depth is positive in the western part of the English Channel and in the Strait of Dover. It is negative along the eastern coast of the United Kingdom. Two positive spots (indicating that the depth should be decreased) are south-west of the Shetland Islands close to the islands The Sneug and Fair Isle which are too small to be resolved by the mesh. This coincidence is remarkable as no tide gauge station is located on the islands. The same spots are also in the sensitivities to the bottom friction coefficient, but with a negative sign implying an increase in the bottom friction. Decreasing depth and increasing the bottom friction coefficient agrees with the existence of unresolved islands.

In contrast the origin of the strong negative bottom friction sensitivity north-west of the Hebrides, as well as the positive sensitivity west of the Hebrides is rather unclear. The region is close to the open boundary, where the sensitivities show a peak, too.

Comparing the results with Fig. 4.8 the  $M_2$  tidal wave seems to be less sensitive to error near the Hebrides and the Shetland Islands than the  $K_1$  tide is.

Next to the already described sensitivities on the bottom friction coefficient near Hebrides and Shetland Islands there is only a significant negative amplitude east of Norfolk and a mixture of negative and positive ones in the Strait of Dover (see Fig. 4.12). For the  $M_2$  tidal wave the bottom friction coefficient in the strait seems also very important similar to the  $K_1$ .

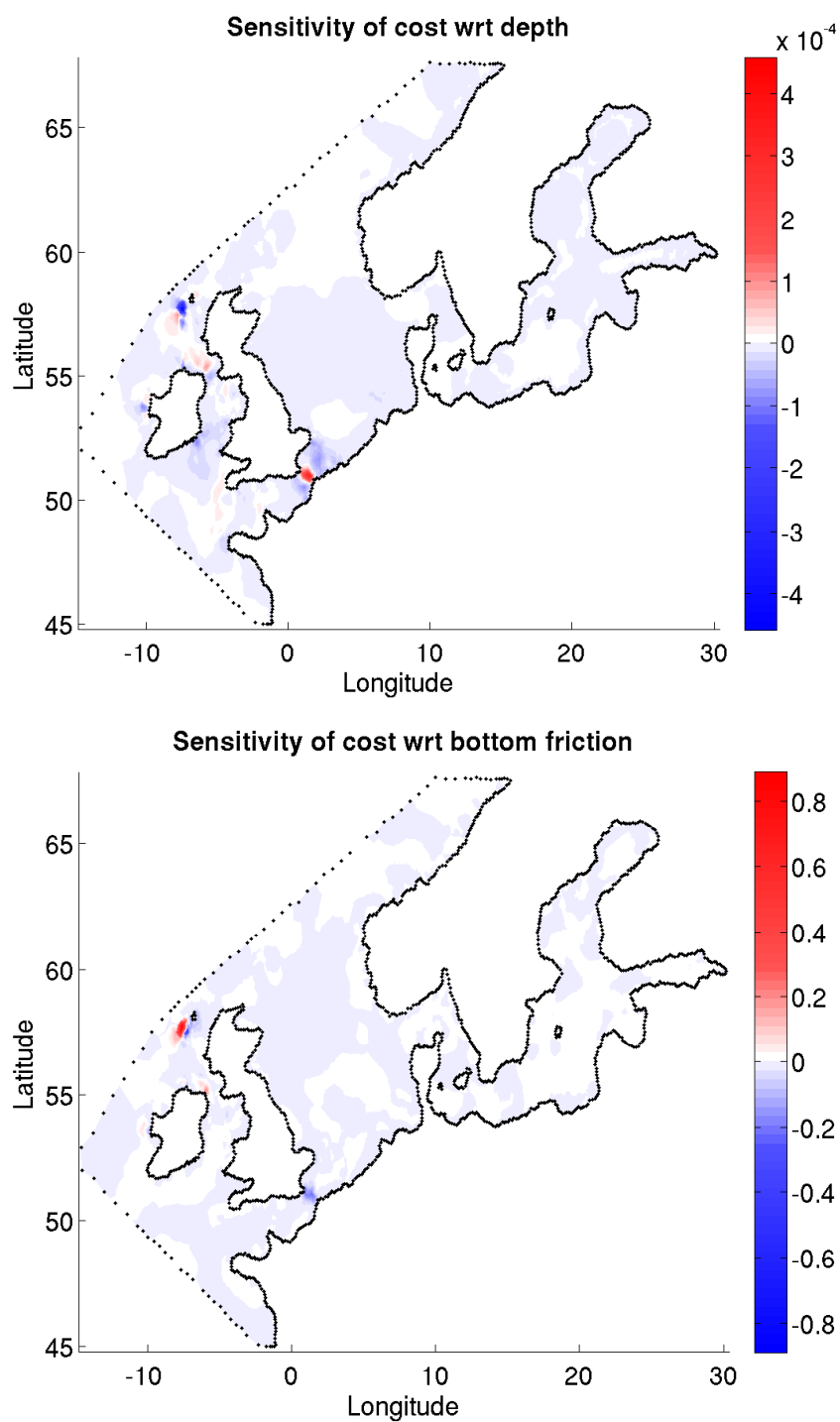


Figure 4.10:  $K_1$  wave: Sensitivities of the cost function on the coarse mesh: With respect to depth (unit is  $m^{-1}$ , upper plot) and the bottom friction coefficient (unit is 1, lower plot).

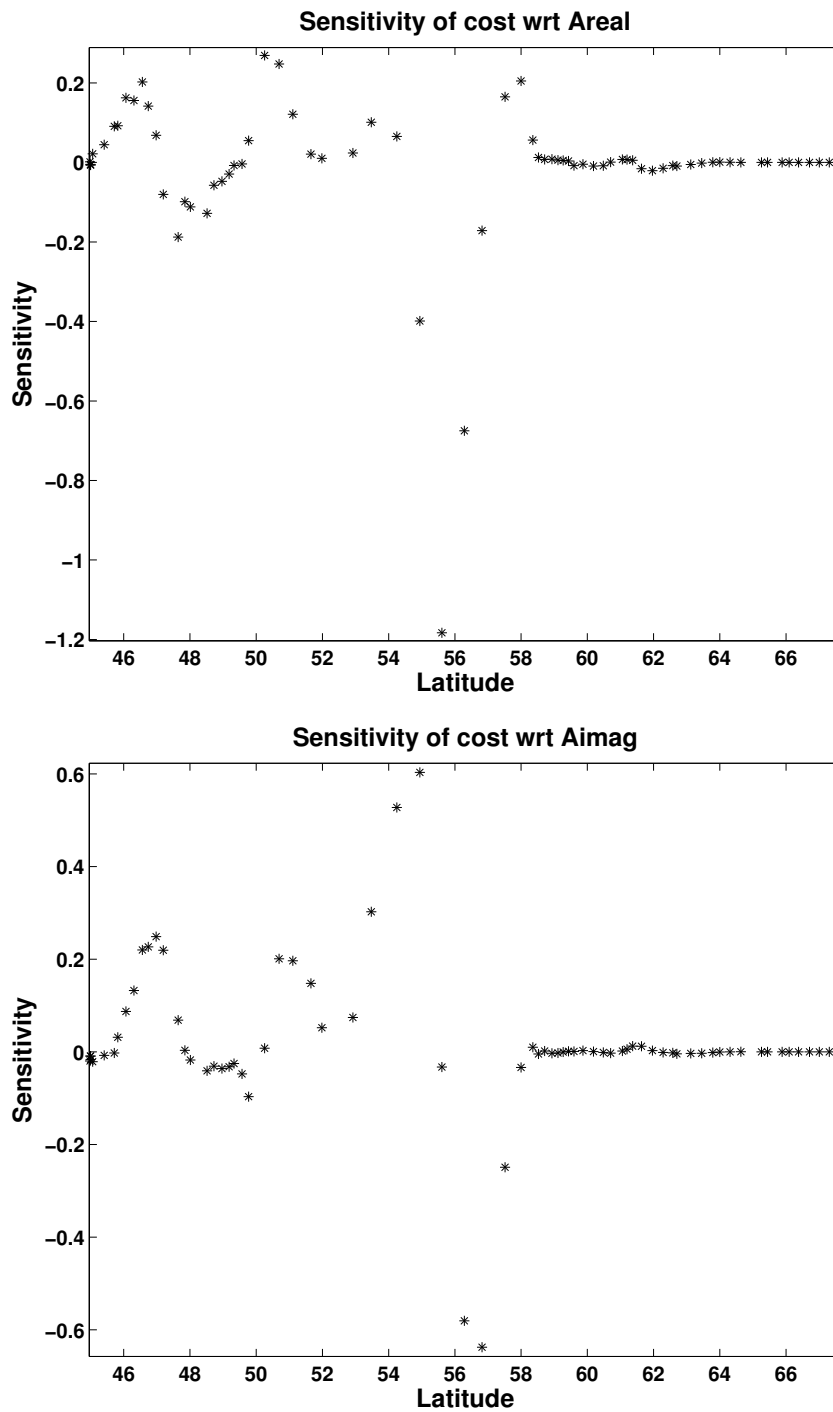


Figure 4.11:  $K_1$  wave: Sensitivities of the cost function on the coarse mesh: With respect to real (upper plot) and imaginary (lower plot) part of the oscillation imposed at the open boundaries in the lower plots (unit is  $m^{-1}$ ).

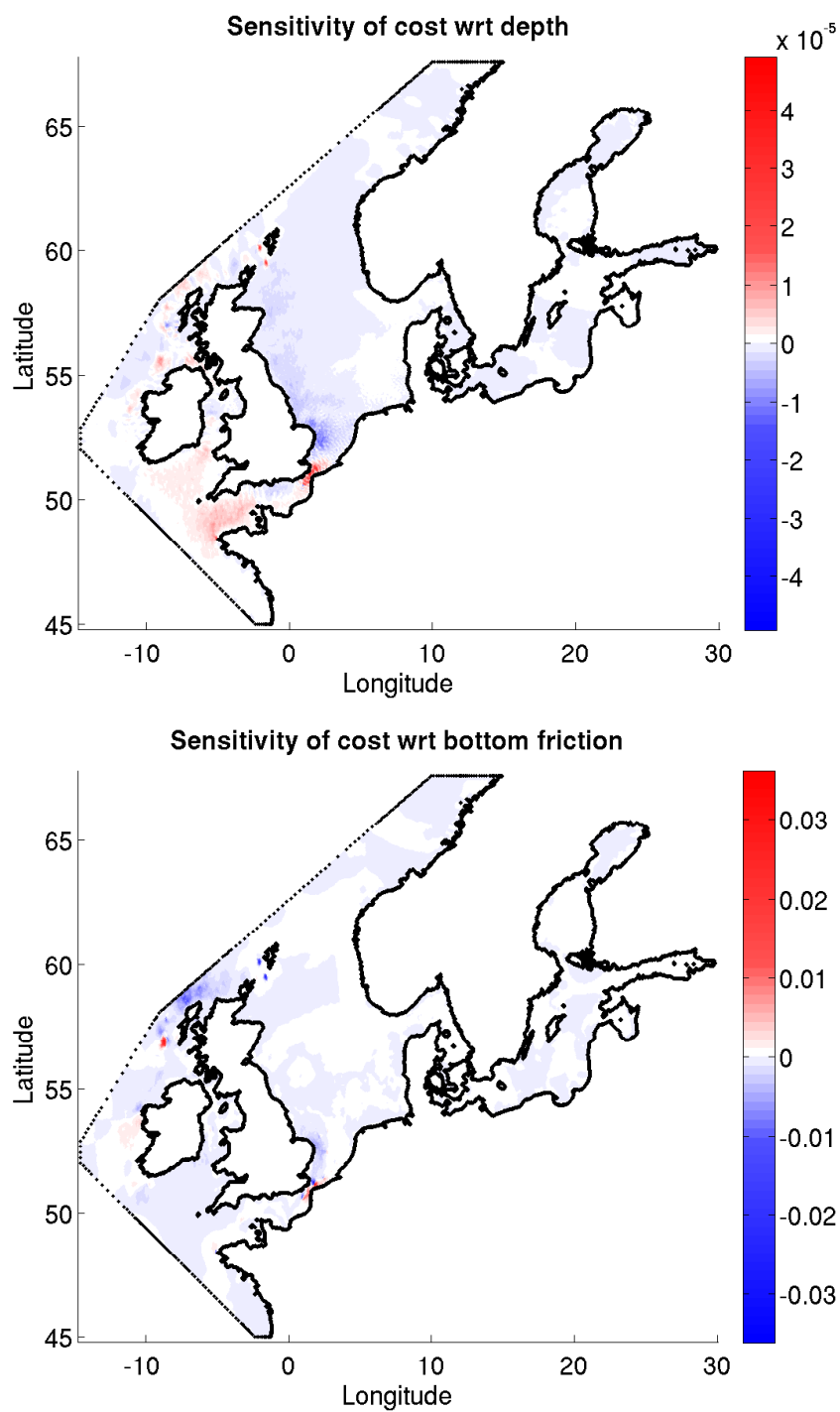


Figure 4.12:  $K_1$  wave: Sensitivities of the cost function on the fine mesh: With respect to depth (unit is  $m^{-1}$ , upper plot) and the bottom friction coefficient (unit is 1, lower plot).

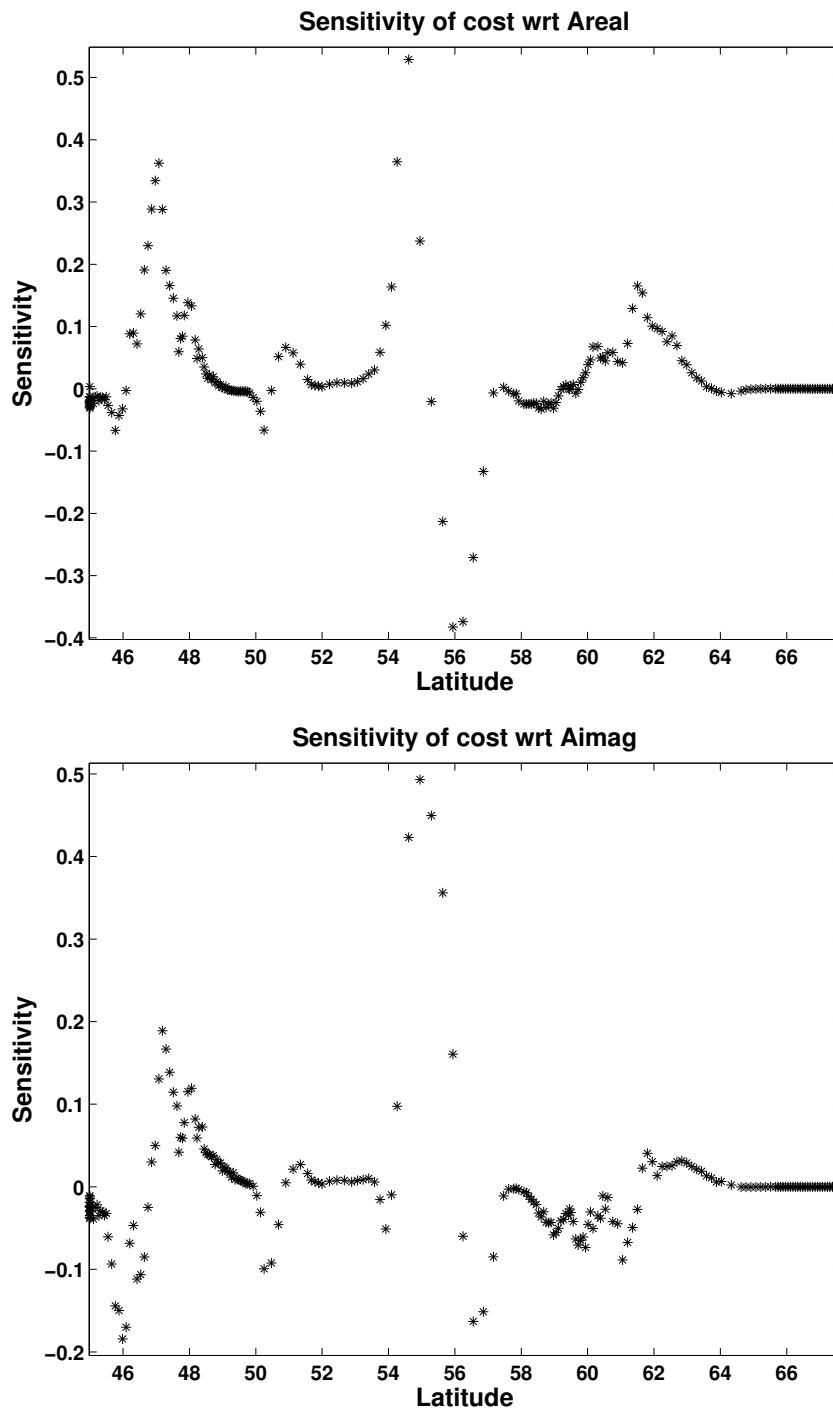


Figure 4.13:  $K_1$  wave: Sensitivities of the cost function on the fine mesh: With respect to real (upper plot) and imaginary (lower plot) part of the oscillation imposed at the open boundaries in the lower plots (unit is  $m^{-1}$ ).

## 4.6 Optimization

In this section the adjoint model and an minimization algorithm give optimal parameters on the coarse test mesh.

### 4.6.1 Setup

Optimal values of the bottom friction coefficients, depth and open boundary values are obtained by minimizing the cost function given in Eqn.(4.1). For optimality the condition  $J' = 0$  has to be satisfied. A standard choice for the minimization of  $J$  is a Quasi-Newton method (see, e.g., Gill *et al.*, 1981). Under the Quasi-Newton methods the Broyden-Fletcher-Goldfarb-Shanno (BFGS) (Broyden, 1969; Fletcher, 1970; Goldfarb, 1970; Shanno, 1970) is very famous one and has been used in various applications (for example by Sidorenko (2004)). Since the problem under consideration here consists of a large number of control variables, the BFGS method is used in a modified versions. A reconsideration by Nocedal (1980) resulted in the so called L-BFGS, which is capable to deal with large size problems. I use this algorithm in the implementation of Gilbert & Lemaréchal (1989) in the program M1QN3 (Gilbert & Lemaréchal, 2008).

The coarse mesh is taken for testing the optimization. This mesh (introduced in Section 4.3) is far from being realistic as its resolution not fine enough. Another aspect is the introduction of a minimal depth of 10m. The right plot in Fig. 4.1 shows the bathymetry with a colorbar between -20 and 10 metres, where negative values are dry land above zero depth line. Every depth that is less than 10m will be corrected to be ten metres in the model and, consequently, the coarse grid introduces a very big error in the bathymetry. For testing the optimization routine this error is quite good, as it shows whether the algorithm brings the values closer to the true depth.

The model runs 5 tidal cycles to cancel the transient waves from the initialization. Afterwards I compute the derivatives with the reverse code and pass them, together with the value of the cost function (which is computed after each tidal cycle), to the M1QN3 routine. It computes new values of the parameters and, afterwards, calls the forward and reverse code to obtain new values of the cost function, state variables and derivatives.

Since abrupt changes in depth and bottom friction generate waves, the model computes over 7 additional cycles to ensure that the solution has adjusted to the new parameters. M1QN3 then uses the values of the last adjustment cycle. With this procedure the waves are damped away and do not blur the new cost function value. Here I observe that the first and second cost function value of the adjustment cycles differ considerably from the steady value obtained after some cycles. But omitting this adjustment led to

worse results in the optimization.

M1QN3 repeats this procedure until a stopping criteria is reached. If the ratio of the norms of the current to the initial gradients falls below  $10^{-5}$ , M1QN3 stops because the minimum is attained. Another stopping criteria is the maximal number of Hessian matrix updates (between 5 and 200) and the maximal number of simulations (between 200 and 5000) (where simulations are calls to the (differentiated) model) . For the control vector update the gradient is multiplied with a step size length. If this step size length falls below the machine precision, the update may no longer be in descent direction and the routine stops, too. For further details about the stopping criteria see Gilbert & Lemaréchal (2008). Additionally M1QN3 is aborted, when the new depth or the bottom friction coefficient is less than zero.

The next questions is whether the parameters should be optimized sequentially or parallelly. The sequential mode means that the depth, bottom friction coefficient and open boundary values are optimized in separate runs and not at the same time. The magnitudes of the derivatives vary considerably (as it can be seen in Fig. 4.6 and Fig. 4.7) and need appropriate scaling. M1QN3 determines weights for each component of the control vector and should, therefore, be able to optimize depth, bottom friction and open boundary values in parallel. It has the advantage that the procedure is faster. However, it turned out that this procedure was a bit problematic, as M1QN3 did not scale properly.

Since the coarse mesh uses strongly corrected bathymetry to 10m in the shallow parts, I expect the error for the depth values to be biggest. In the parallel optimization, M1QN3 first applied the correction mainly to the bottom friction coefficient as its sensitivity is higher than for the other parameters. When the parameters were simultaneously optimized, it also happened that the open boundary tried to adjust for depth errors as well. Thus, the total the cost function value still decreased, but comparing the tide gauge error before and after the optimization only about half the stations got better the values, while the other half got worse. This was especially true in the Irish Sea, which is close to the adjusted open boundary. One may argue, that this indicates an error in the derivative, but the cost function decreased, so a descent direction was indeed found.

Consequently a sequential optimization for each parameter is recommended in the test setup, starting with the parameter, where the expected error is largest. I iteratively optimize first for depth, then for open boundary amplitudes and afterwards for the bottom friction coefficient. This procedure also has the advantage that I can vary the scaling coefficients  $s_p$ ,  $s_c$  and  $s_h$  of the cost function (see Eqn.(4.1)) to be appropriate for each parameter.

## 4.6.2 Results

Three experiments are carried out with sequential optimization of the parameters. First I only optimize the depth, as it gives the highest error reduction, when only one parameter is optimized. Second I repeat the first one, but proceed with the optimization of open boundary values and bottom friction coefficient. The number of iterations is 5 and the number simulations is 200, which is very low, but has also been used by Heemink *et al.* (2002). The optimization of depth stops with the maximal number of iterations. In the next step I prolong the optimization to stop after maximal 200 iterations and 5000 simulations. Here all parts of optimization finish with minimal step length, so some optimum has been reached.

In all experiments the scaling coefficients are  $s_p = 1$ ,  $s_c = 0$ ,  $s_h = 1000$  in the depth,  $s_p = 1$ ,  $s_c = 0$ ,  $s_h = 0$  in the open boundary and  $s_p = 100$ ,  $s_c = 20$ ,  $s_h = 0$  in the bottom friction coefficient optimization.

### Short optimization of depth

In more than two thirds of the station the value of the cost function is reduced by a factor of two approximately. Fig. 4.14 shows the amplitude and phase error change due to the optimized bathymetry. The left column shows the error change over the station number, where blue dots indicate error reduction and the red ones an increased error. The charts on the right have red (blue) points at the locations of error increase (decrease). Magenta ones indicate large error increase. At almost all stations the error in both phase and amplitude is reduced. There are only two stations with a major increase in phase error. One is in the North Channel of the Irish Sea and the other near Portsmouth in the English Channel. Both locations are probably poorly represented by the mesh. Additionally, there is an amphidromic point near Portsmouth which may introduce big phase changes due to small displacements of this amphidrome. In general there are more stations where the amplitude gets worse than so does the phase.

### Short optimization of all parameters

The next step is the optimization of all the parameters. First the value of the cost function decreases with the optimization of the depth from about 79 to 40, and then to 29 in the open boundary optimization. The optimization of the bottom friction coefficient further decreases the cost function, but only relatively small compared with the other steps. The reason is probably that the change is too small (see Fig. 4.18) and tuning of the M1QN3 settings may result in stronger decrease. Another reason may be that additional further reduction of error can only happen when the mesh is refined.

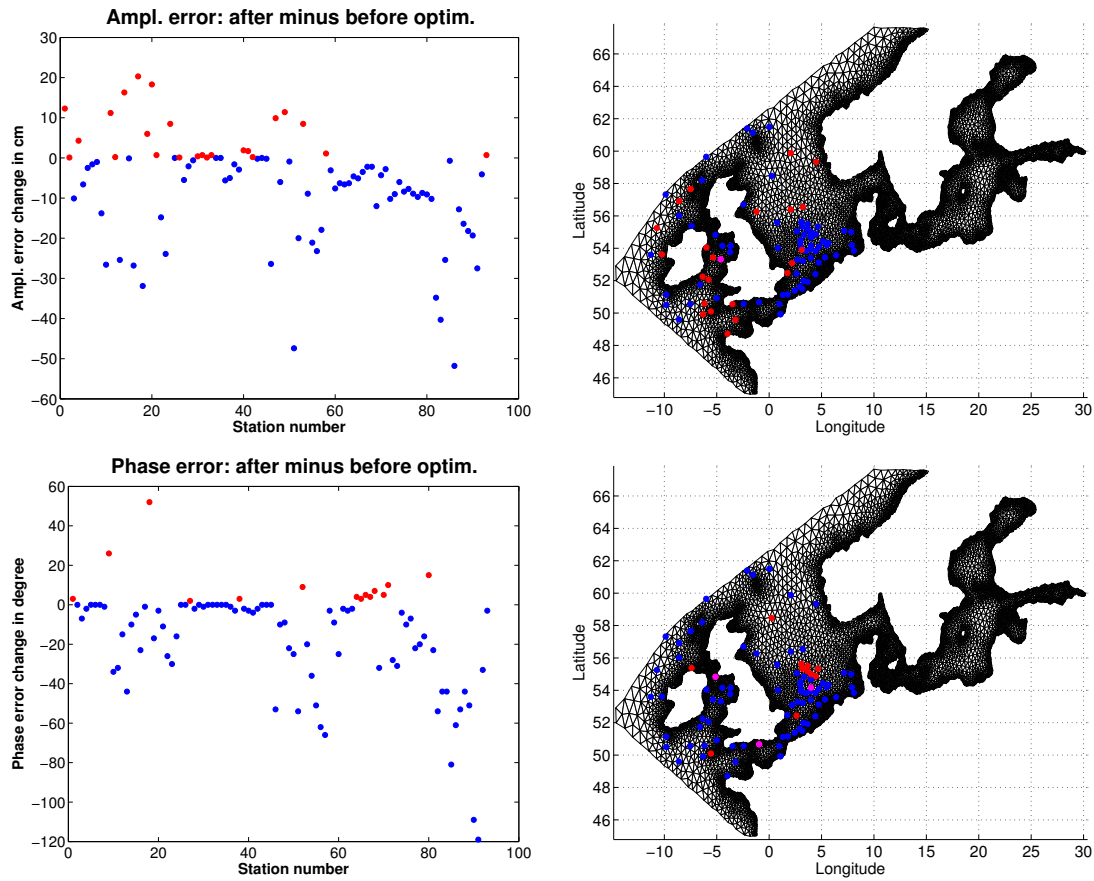


Figure 4.14: Short optimization of depth: Amplitude and phase error change. Left: Amplitude and phase error change over the station number. Right: At red dots the error increases, at blue dots the error decreases, magenta dots indicate major error increase.

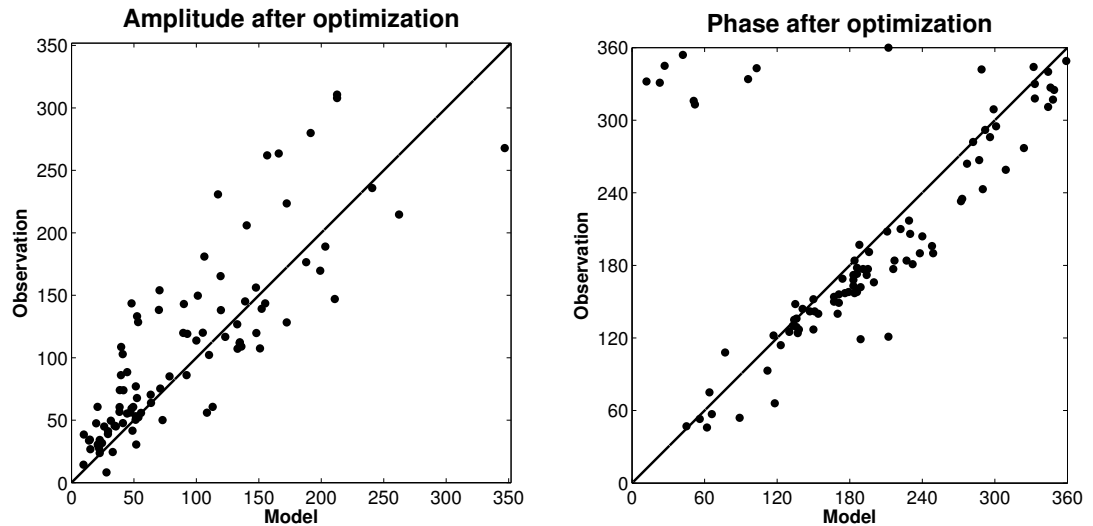


Figure 4.15: Short optimization of all parameters: Correlation of amplitude (in cm) and phase (in degree) between model and observation at the stations after the optimization.

The improvement of model results can also be assessed by the correlation of amplitude resp. phase between model and observation before and after the optimization. The correlation before is shown in Fig. 4.3 on the right side, and after in Fig. 4.15. Comparing them the optimization improves the agreement especially for the phase, while the amplitude is generally reduced. Nevertheless, the correlation on the fine mesh (see Fig. 4.3) is still much better than the one on the coarse mesh even with optimization.

The next question is whether the new parameters are realistic. The difference between optimized and initial depth is given in Fig. 4.17. The depth increases in the English Channel and between England and the Netherlands up to 20m. An increase of this size would mean a relative error of about 50%, which is not unlikely as in some places the depth was considerably changed due to the coarse mesh resolution. A zoom into the domain at the Strait of Dover and rescaling the colorbar (left plot in Fig. 4.17) shows that the algorithm tends to reduce the depth where it was set to 10m, namely in the Netherlands, at the Wash and at the south-eastern tip of England. This proves that the optimization tends to reproduce the depth correctly at least in some parts.

The new bottom friction coefficient ranges between  $2.07e^{-3}$  and  $3.27e^{-3}$ , which is a realistic range, but could vary more, too. The areas, where the value has mainly changed, are near the open boundary west of the Breton coast and in the Strait of Dover. The first one could be a reaction on the changes on the open boundaries. The second one may still be the result of the coarse mesh or may be attributed to increased frictional losses in this region, which are not given by the constant bottom friction coefficient. The

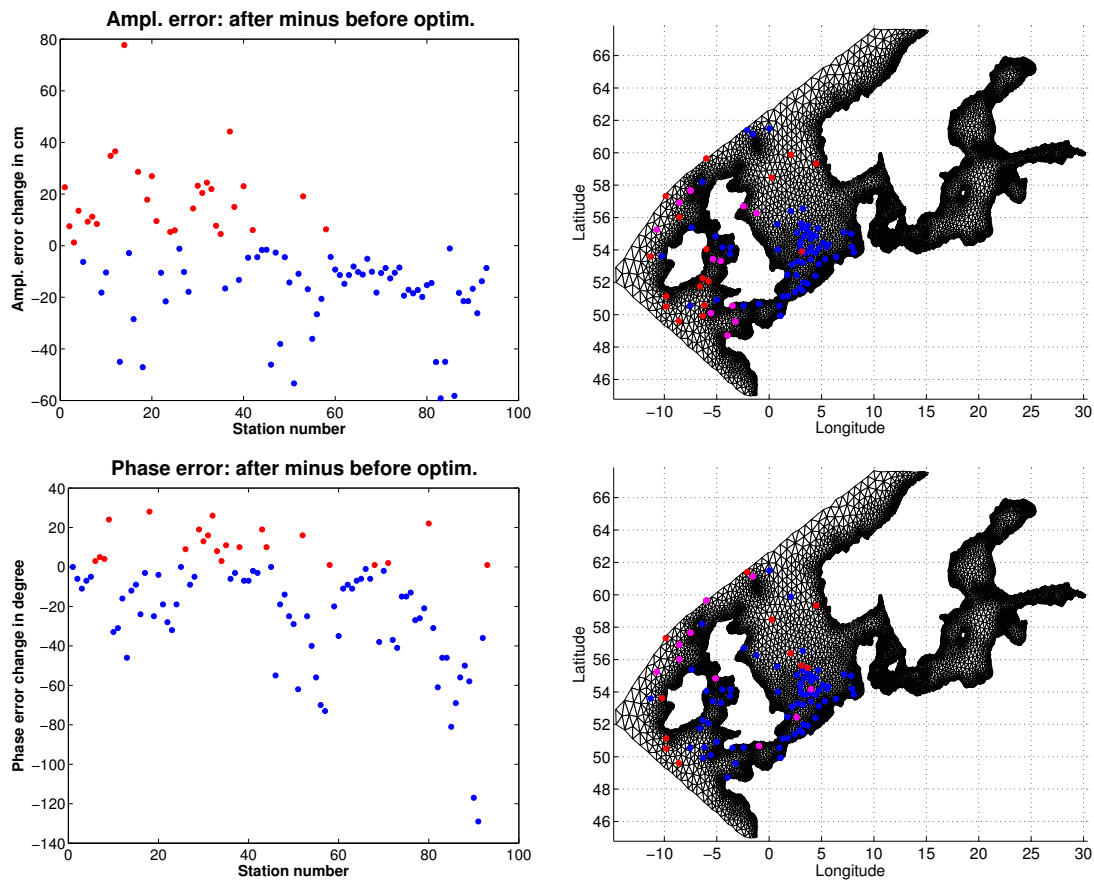


Figure 4.16: Short optimization of all parameters: Amplitude (upper plots) and phase (lower plots) error change due to optimized bathymetry, bottom friction coefficient and open boundary values. Right: At red dots the error increases, at blue dots the error decreases, magenta dots indicate major error increase.

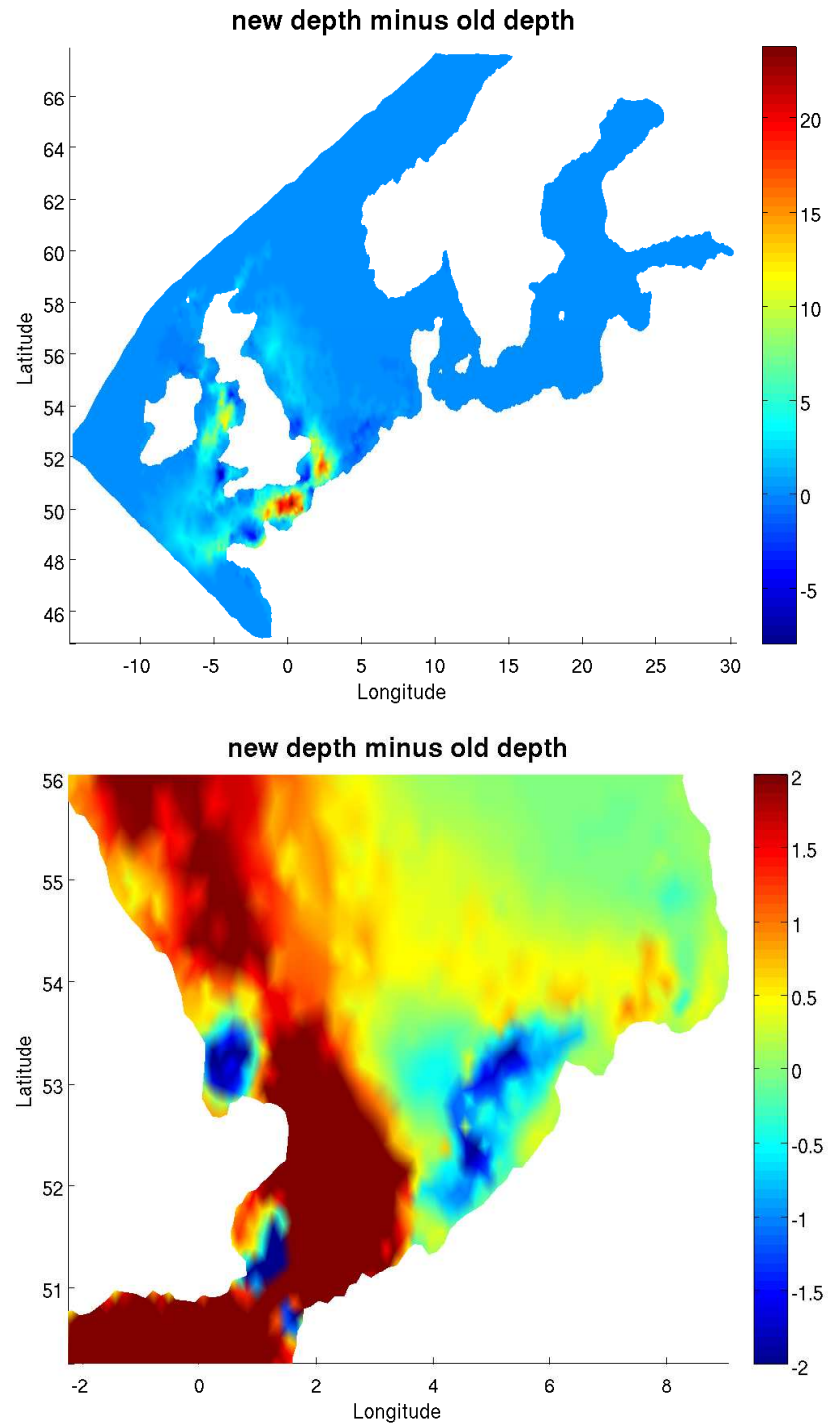


Figure 4.17: Short optimization of all parameters: Optimized depth minus initial depth in m.

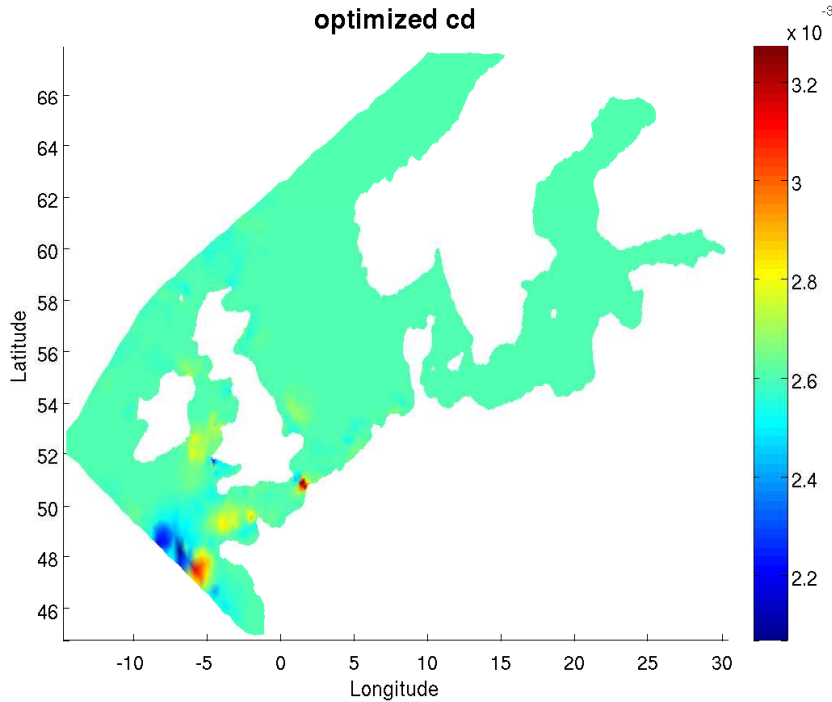


Figure 4.18: Short optimization of all parameters: Optimized bottom friction coefficient.

pattern of the optimized bottom friction coefficient in Fig. 4.18 resembles only marginally the sensitivities on the coarse mesh in Fig. 4.6. The strong changes in the Strait of Dover are at least in the same region, where the sensitivities on the fine mesh (Fig. 4.8) also showed high magnitudes.

Thus, proceeding to optimize open boundary values and bottom friction coefficients after the optimization of depth make the results worse, especially near the open boundary. This can be seen by comparing Fig. 4.14 and Fig. 4.16. More stations are marked with a red point. The cost function decreases with further optimization, so in the sum the error is reduced by optimizing the open boundary and the bottom friction coefficient. The reason why the error increases at more stations is probably that the stations with a higher amplitude are stronger weighted. I suspect that the open boundary corrects for resolution errors within the domain. Therefore it is actually getting worse. But the depth optimization has probably not yet been finished, so a longer optimization experiment is performed in the next section.

### Long optimization of all parameters

The number of maximal iterations is now set to 200, the simulations to 5000 and all parameters are optimized until the minimal step size length is

reached. In the optimization of the depth the cost function value decreases from 80 to about 10, afterwards from 10 to 8 for the open boundary values and the optimal bottom friction coefficient reduces the error slightly further. This behavior of the error reduction is similar to the experiment before.

Fig. 4.20 shows the error reduction at the stations. The error increases only at 12 stations for the phase and at 15 stations for the amplitude, while it improves considerably over the rest. Comparing these results with the former ones, where the upper limit of the number of iterations (simulations) was set to 5 (200) (shown in Fig. 4.14 for the optimization of depth and in Fig. 4.16 for all parameters), the longer computation shows much better agreement. In the former optimization for depth alone the result gets worse at 14 stations for the phase and at 24 stations for the amplitude. The short optimization for all parameters gives 22 worse stations for the phase and 29 worse stations for the amplitude. So further optimization degrades the result, when the depth is not enough adjusted.

The correlation after the long optimization is shown in Fig. 4.19. Compared to the short optimization in Fig. 4.15 the phase and amplitude is further improved. The phase correlation is as good as in the fine mesh (see Fig. 4.3), but the amplitude is worse than on the fine mesh.

More insight can be gained from tidal chart plots. The amplitude and phase of the  $M_2$  tide is shown before and after the long optimization in Fig. 4.22. The phase plot before the optimization shows that the amphidrome at the Norwegian coast (see Fig. 1.3) has been shifted towards the south. The one in the central North Sea is also distorted. The amphidromes in the North Sea should be situated more to the west. This error is probably due to the bathymetric error introduced by the coarse mesh (see Fig. 4.1). After the optimization they are correctly represented. According to the results of Flather (1976) this is even the case for the ones in the Irish Sea.

Similar to the short optimization I want to analyse the realism of the produced parameters. The depth change and the new bottom friction coefficient are shown in Fig. 4.21. In contrast to Fig. 4.17, where the depth decreased consistently with my expectation in the optimization, the depth has now dramatically increased. The new depth is now obviously less realistic, but the simulated tides are closer to observation. Heemink *et al.* (2002) already stopped the optimization after 5 iterations, although the parameters still changed, probably to avoid unrealistic parameter values.

The bottom friction is less adjusted in the long optimization than in the short optimization (see Fig. 4.18). The stopping criteria are not changed between the two experiments and in both cases the optimization stopped in both

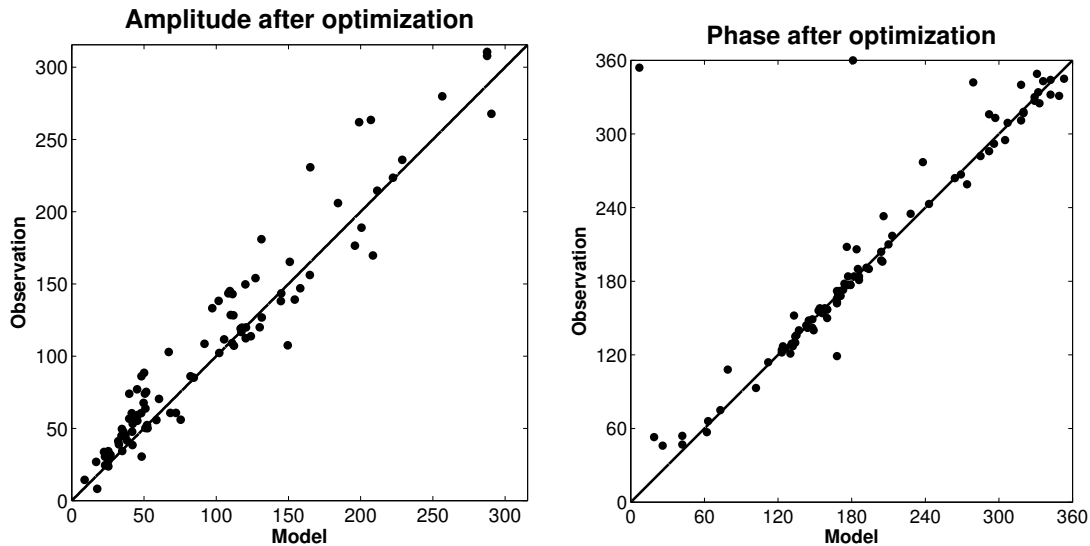


Figure 4.19: Long optimization of all parameters: Correlation of amplitude (in cm) and phase (in degree) between model and observation at the stations after the optimization.

cases because the minimal length of the descent direction was attained. I suppose that the strong adjustment of the depth in the long optimization reduced the error so much, that the descent direction became less steep and M1QN3 stopped earlier.

In the short and long optimization the bottom friction pattern in the Strait of Dover are qualitatively similar. The major difference is the change in the area near the open boundary which is present in the short, but not in the long optimization. Further, in the long optimization there is no increase of error confined to the open boundary. That means, that here the open boundary values are reasonably changed compared to the short optimization.

Several conclusions can be drawn from the results. First, the same tidal wave pattern can be reproduced by two different bathymetries and accordingly the function between surface elevation and bathymetry is not well defined. Second, the coverage of the tidal gauge stations is sufficient to represent the tidal features. The last conclusion is that the results are improved not only locally to fit the observations.

## 4.7 Conclusion

The adjoint model generated by AD is used to perform sensitivity studies. A comparison between the sensitivities of two different meshes and con-

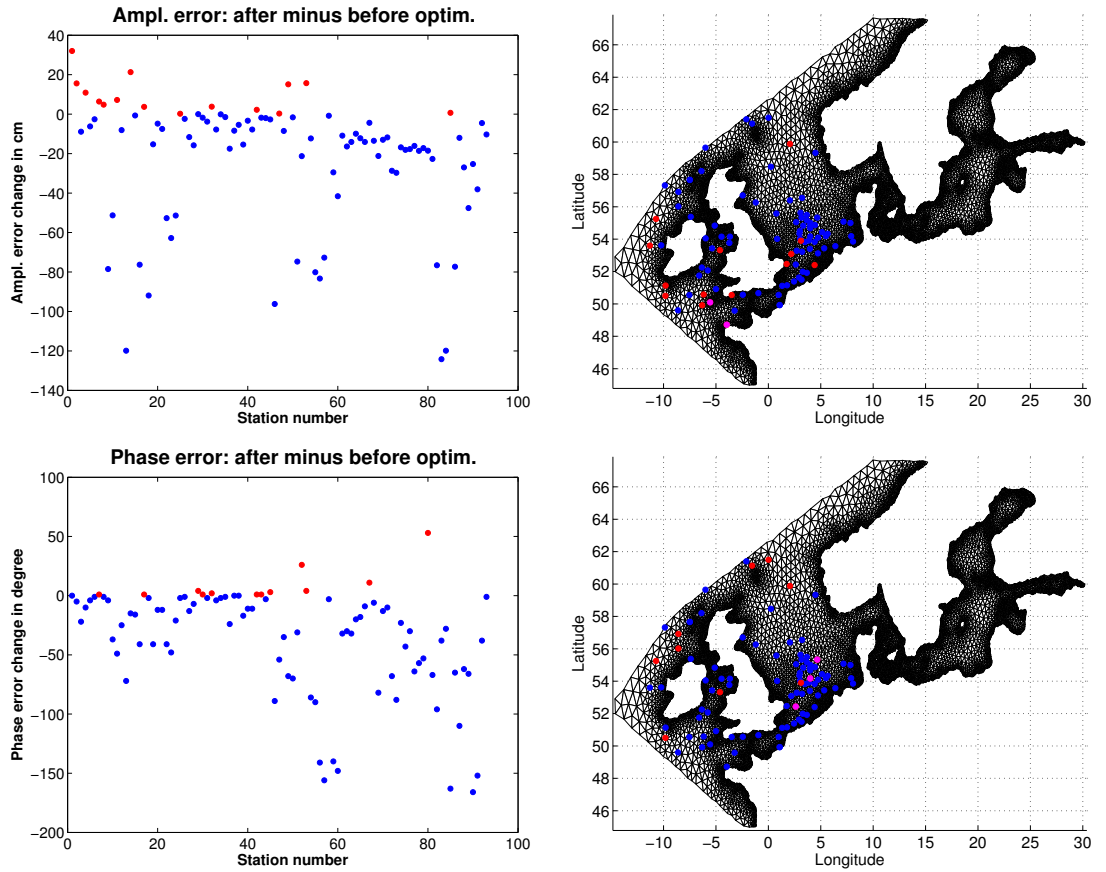


Figure 4.20: Long optimization for all parameters: Amplitude (upper plots) and phase (lower plots) error change due to optimized bathymetry, bottom friction coefficient and open boundary values. Right: At red dots the error increases, at blue dots the error decreases, magenta dots indicate major error increase.

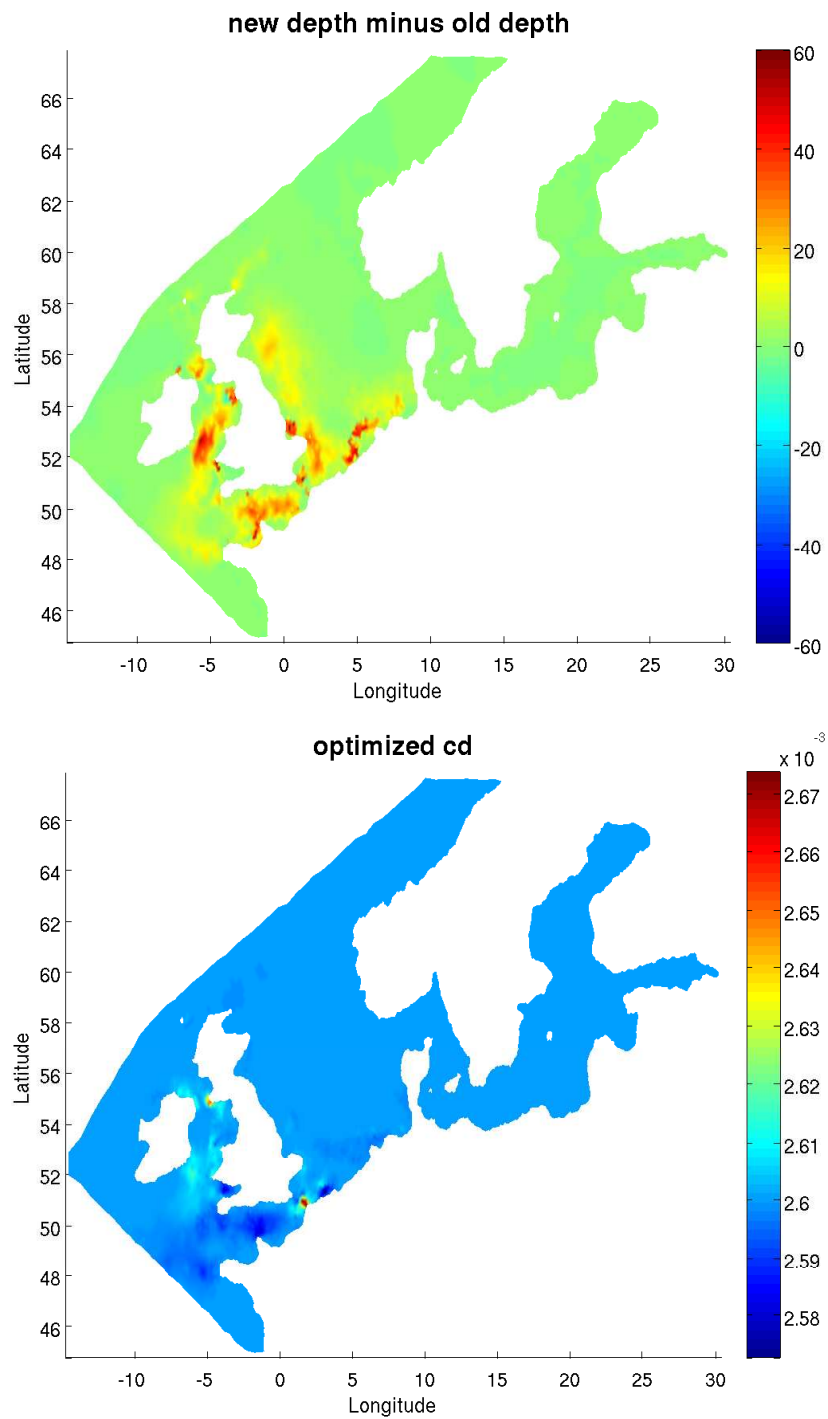


Figure 4.21: Long optimization for all parameters: Optimized depth minus initial depth in m (upper plot), new bottom friction coefficient (lower plot).

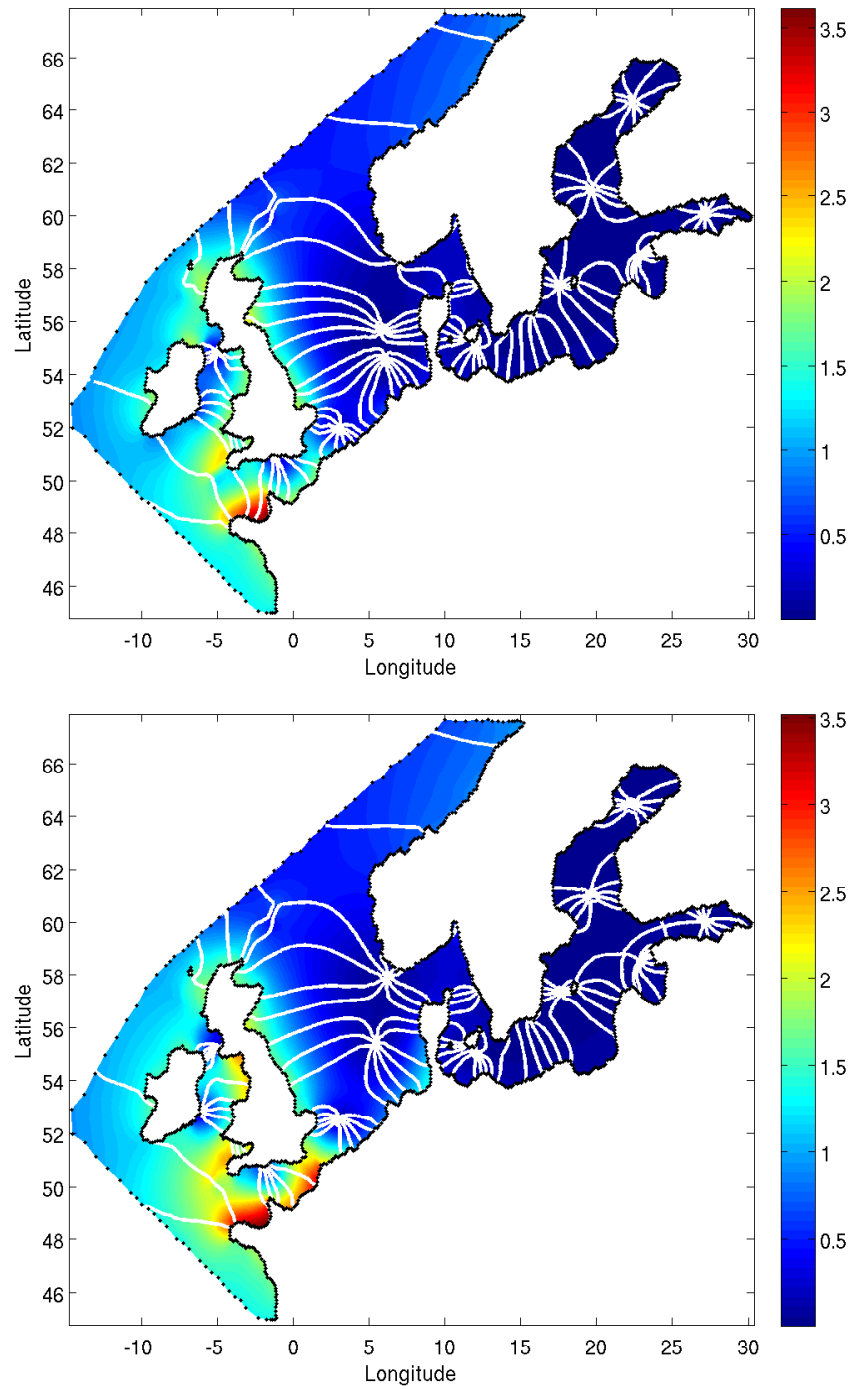


Figure 4.22:  $M_2$  tidal chart before (upper plot) and after (lower plot) the long optimization: Amplitude (in m) is shown in color, white lines connect places with equal phase (the distance between two lines is  $30^\circ$ ).

stituents is carried out. The simulations of  $M_2$  on the fine mesh show smaller errors than on the coarse mesh. The latter lead to a larger distortion of the wave due to bad representation of the coastline and the depth, although the same bathymetric data and mesh generation algorithm is used. The  $K_1$  tide acts contrary. Probably the weak-filtering in NCLF distorts the simulation on the fine mesh more than on the coarse mesh leading to better results on the coarse mesh.

This difference is also reflected in the sensitivities on the two meshes. The result shows that the sensitivities exhibit mesh errors; therefore, they can be used for mesh refinements.

The  $M_2$  tidal wave sensitivities show that its simulation can be improved by correcting its representation in the Irish Sea, Celtic Sea, English Channel and Strait of Dover. Although the largest coastline and depth errors are introduced along the Dutch coast, it does not show the strongest sensitivity on the coarse mesh. On the fine mesh the sensitivities suggest a decrease in depth in the English Channel and an increase of it in the Irish and Celtic Seas. This analysis further shows that the bottom friction coefficient should be more variable spatially (especially in the Strait of Dover). The latter is consistent with the proposed parameter areas of Heemink *et al.* (2002).

The sensitivities of the  $K_1$  tidal wave on the fine mesh suggest depth and bottom friction coefficient changes in the area of two small islands, which were too small to be represented correctly by the mesh. A depth optimization could reconstruct these islands therefore.

On the coarse mesh the  $K_1$  sensitivities show a bad representation of the tidal dynamics in the Strait of Dover and near the Hebrides. This is certainly the case. On the coarse mesh the small islands are not captured by the sensitivities.

Considering the sensitivity differences between  $K_1$  and  $M_2$  tide, the  $K_1$  tidal wave is more sensitive to the parameters north-west of the United Kingdom than the  $M_2$  tidal wave. For the fine mesh the error in the  $M_2$  simulation is influenced stronger by correcting parameters in the Irish Sea and the English Channel, than it would be the case for the  $K_1$  wave. The latter shows highest sensitivities in the Strait of Dover.

For both constituents and meshes the results of the open boundary sensitivities indicate that improvements of the tidal simulations are possible by changing their values in the region of the Celtic Sea, the English Channel and north-west of Ireland and Scotland. The influence of the open boundary west of Norwegian is less important, as the wave mainly exits the domain here.

The optimization of the parameters with the adjoint model and a BFGS algorithm is the next step. Since the sensitivity study has shown different scales of the involved parameter derivatives, appropriate scaling is needed to perform the optimization of all parameters parallelly. For the given test mesh the

parallel optimization does not lead to sufficient convergence; therefore the optimization of the depth, open boundary values and bottom friction coefficient is done sequentially in that order.

As pointed out by Lyard (2009), the constituents for the open boundary values at the European Continental Shelf are known with a very high accuracy. Nevertheless, the sensitivity study shows that there can still be inconsistencies between model and prescribed data. This is due to the different representation of topographic features close to the open boundary. Its values shall be consistent with the dynamics inside the domain; therefore, its optimization is applied after the tuning of the depth. It may be advisable to optimize them after each adjustment of the parameters to ensure consistency.

The short optimization gives a new bathymetry, reducing errors in the coastline and the introduced correction to 10m of minimum depth. The optimized open boundary values partly try to reduce the bathymetric or mesh error, which decreases the total error but increases the error in specific parts of the domain. Consequently, it has to be known in advance where the source of model error is. Then the right parameters are corrected first until some minimum is achieved.

On the other hand the long optimization results in an unrealistic bathymetry. This may have the following two reasons. First it is possible that several bathymetries give the same or similar tidal charts at observational stations. To which one the optimization converges is determined by the regularization. The second reason is, therefore, connected with the regularization. It only penalizes when the total depth tends to be smaller than the amplitude of the tidal wave. In order to have a bathymetry closer to reality, an additional term has to be added to the cost function. This term could have for example the shape of the Gaussian bell with the initial guess as mean and the parameter uncertainty determining its variance. In the test setup the depth error is variable in space due to the absence of wetting and drying. It also depends on the representation of the depth by the mesh, which may be very big in the test case as the resolution is very coarse. The depth error is, therefore, very complex and not only connected to the error in the bathymetric data. On the fine mesh with wetting and drying the depth error will be more homogeneous. Then a similar penalty as it has been used for the bottom friction coefficient can be used.

Finally, only when the optimization is able to reproduce the real depth, it may lead to realism in the bottom friction coefficient. If one is interested in estimating frictional energy loss on a continental shelf, the variable bottom friction coefficient is the relevant parameter and shall be determined correctly. But when it tunes the model closer to observation but for wrong reasons (e.g. to recover incorrect mesh representation of the bathymetry) the energy sinks may not be located at the true positions or may not agree in magnitude. Structured grid models are even more vulnerable, as they

cannot represent the coastline to the extent the unstructured mesh models are able to.

A better bathymetry reduces the error significantly, leading to less severe depth changes. It may, therefore, prove possible to first optimize for open boundary values and bottom friction coefficients or to do the optimization in parallel.

# Summary

In this thesis seven unstructured grid models based on FV and FE techniques are used to solve the 2D shallow water equations for tidal simulations on triangular meshes. Linear functions in either non-conforming ( $P_1^{NC}$ ) or continuous ( $P_1$ ) form are used to discretize velocity and elevation respectively. The non-conforming (NC) version is implemented with leapfrog explicit (NCLF), Adam-Bashforth (NCAB) and semi-implicit (NCSI) time stepping. The continuous P1P1 version is only semi-implicit because of the particular form of stabilization. The other three models use the FV spatial discretization employed in Chen *et al.* (2003) and Runge-Kutta (FVRK), Adam-Bashforth (FVAB) or semi-implicit (FVSI) time stepping.

The models compute the major lunar tidal constituent, called  $M_2$ , on a North and Baltic Sea mesh and their performance is compared with respect to tide gauge data and CPU run time. All models agree reasonably well with observation. Probably due to the specific kind of stabilization, P1P1 is worse than the other models. The latter have only minor differences with respect to vector error, correlation, relative amplitude and hours error. Especially, for the FV models the time stepping method does not affect the model result. This shows that the order of approximation is given by the spatial discretization. But the temporal schemes change the CPU run time. Due to the decrease of time steps semi-implicit codes are faster by at least a factor of two here.

Nethertheless, the results are far from the accuracy that can be achieved with unstructured meshes. The fact that errors are similar for all models with different spatial and temporal discretization methods, hints at the role of external factors, like topography, mesh, bottom friction and open boundary conditions. In particular this implies that it is not worthy employing higher order methods, but to have, for example, a better resolving mesh and tuned parameters.

To address this issue the NCSI model is further developed by including the tidal potential and the Flather open boundary condition. The latter needs additionally velocity data at the open boundaries. The Flather open boundary condition reduces the underestimation of the  $M_2$  wave on the North and Baltic Sea mesh.

Furthermore, NCSI is also tested on a finer mesh spanning over the European Continental Shelf, since the tidal elevations and velocities are more reliable in the Atlantic Ocean than in the English Channel. On this mesh the

$K_1$  tidal wave is overestimated with the Flather boundary condition and better results are obtained with the clamped boundary condition. The influence of the open boundary condition on the  $M_2$  simulations is weaker.

The question, which open boundary condition is best, cannot be fully answered by looking at its mathematical correctness. It is strongly depending on the available data and configuration of the mesh/open boundary to the depth. According to Lyard (2009) only depth gradients tangential or normal to the open boundaries bring good results. Open boundaries in shallow depths are affected by non-linear processes and in deep waters the Coriolis force is relatively strong. As in tidal shelf seas the open boundaries are the forcing term, it is not surprising that the results here depend on the appropriate open boundary conditions, values and location.

On the European shelf mesh the  $M_2$  results correlate better with the observations than on the former North and Baltic Sea mesh. It can be attributed to the finer resolution of the coastline. Both meshes are based on the same bathymetry data, but are generated by different algorithms resulting in a different nodal distribution with approximately the same number of nodes. Mesh generation is therefore an essential part of the model setup and has also big influence on the model results.

On the European shelf mesh the energy balance and the tidal residual currents of the  $M_2$  wave show that energy still increases after 25 tidal cycles. The tidal residual currents are correct in their directions and appearance, but their magnitudes tend to be too high in specific shallow regions. This might imply that some dissipation is missing. Dissipative parameters are the bottom friction and viscosity coefficient, which need not to be constant as assumed and have to be tuned.

The energy balance also shows that the bottom friction is the main sink of energy. The viscosity and the P1 projection method for advection contribute with a smaller extent. Advective processes shall not dissipate energy. Fully NC advection schemes for non-conforming elements need to penalize the discontinuous part of the velocities across the edges. These fully NC schemes have not proved to be as stable as the P1 projection method and therefore need further improvements.

As it has already been mentioned, model results can be improved by tuning parameters like the bottom friction coefficient. The adjoint approach is used to tune the model parameters such that a compromise between model results and data is achieved. The use of automatic differentiation (AD) to generate the adjoint model is especially attractive since the differentiation can easily be repeated when the forward code has changed. The NCLF model is adjusted to the requirements of the AD tool TAMC and it is used for sensitivity studies.

The sensitivities of a cost function with respect to the bathymetry, the bottom friction coefficients and the open boundary values are computed. The cost function measures the misfit between observed and simulated fields. The observations used in this thesis are the constituents of the analyzed tide gauge station data.

The sensitivity pattern suggests that the parameters needed to be optimized for the  $M_2$  wave are mainly in the Irish Sea, the Celtic Sea, the English Channel and in the Strait of Dover. The  $K_1$  tide, on the other hand, is dominantly sensitive to parameter values north-west of Ireland, near Scotland, the Shetland Islands and in the Strait of Dover. The sensitivity regions of  $M_2$  and  $K_1$  mostly do not overlap (except for the Strait of Dover).

The open boundary values are more sensitive for both waves in the Celtic Sea and north-west of the United Kingdom than west of Norway. The parts of the open boundary, where the tidal wave enters the domain, are more important than in the regions, where it leaves.

Further, the sensitivities computed by simulations on a coarse and a fine grid are compared. They are significantly different. Since the sensitivities are mesh dependent and the parameters are defined at nodes, it can be concluded that the initial error does not lie in the parameter values, but in the mesh resolution.

In some points a strong sensitivity of bottom friction and bathymetry is located, where islands are not properly resolved by the mesh. These results indicate that the sensitivities can be used for mesh refinement.

To test the adjoint model a Quasi-Newton method is used to optimize depth, bottom friction and open boundary values sequentially on a coarse grid of the European Continental Shelf. The misfit to the observation is reduced by a factor of about 10. The new tidal chart is better than before in the whole domain. The optimized model parameters are acceptable except in areas, where the features in coastline and depth are underresolved. Thus the optimization algorithm projects the discretization error on the control set. In this case the mesh resolution has to be tuned prior to the optimization process. Due to a lack of computational resources this has not been done in this thesis and is left for future studies.



# Outlook

During the preparation of this thesis many issues raised. Some were concerned with the stability of the model. I identified them to be connected with advection, wetting and drying and the underlying mesh.

For non-conforming FE methods the advection needs some flux penalty on the discontinuity of the velocity. This issue is only slightly covered in this thesis. The projection method was more stable than the fully NC advection, but introduced additional dissipation of energy. Advective processes influence model results considerably and, therefore, the advection treatment may be reconsidered with respect to the penalty on discontinuity.

Wetting and drying is straightforward to realize with explicit time stepping, but for semi-implicit models it turned out to be more difficult. During this thesis some methods have been implemented for the non-conforming FE method, but testing them led to a unsatisfactory results. A detailed analysis of this issue is planned for future studies.

Meshes are always a compromise between smoothness, mesh size and resolution. Generation of such meshes is not an easy task and requires a lot of experience. In the sensitivity studies it turned out that adjoint models are useful for identifying regions, where the mesh supposed to be refined. The next step is now to couple the adjoint model to a mesh generator and iteratively improve the simulations by generating new meshes based on the sensitivities. The issue is to find or set up a mesh generator, that gives smooth meshes with a low computational load. Possible candidates is TRIANGLE with the additional smoothing routines of Sven Harig or gmsh (see [www.geuz.org/gmsh](http://www.geuz.org/gmsh)).

With respect to the optimization of the parameters, the computations in this thesis were done on a desktop PC. The next step will be to run the optimization with the fine mesh on a more powerful computer to obtain realistic estimates of the bottom friction coefficient and with less severe initial errors in the depth.

Many difficulties also raised from the generation of the adjoint model by using automatic differentiation. First, the code has to be structured in such a way that the AD tool understands the dependencies. After the successful differentiation, the adjoint code has to be tested for the correct derivative. This was obviously done, but required some experiments until the differentiated code was correct. Furthermore, the computational performance depended

strongly on the inserted checkpoints. At checkpoints the results from the forward solution are saved to be used in the reverse sweep. An optimal balance between memory usage and recomputation exists mathematically. Many AD tools have been tried and finally TAMC was taken as it gave a code with the correct derivative and reasonably fast. The disadvantage was that the code had to be changed at many places. TAMC is a predecessor of TAFF, which is one of the most common AD tools on the market but unfortunately not freely available. Many of the freeware tools are still not mature enough to cope with the complexity of ocean models. Often the generated adjoint models are very slow. Since the speed of the derivative calculation is very important for future fine mesh applications, it will be of immediate need to compare the performance of the adjoint codes generated by different AD tools. The forward model should be altered only slightly and the adjoint code should be reliable and fast. These criteria were not met completely by TAMC and so other AD tools should be further investigated.

Optimization algorithms for a large number of control variables is also a research topic by itself. It could be of interest to try other optimization techniques such as for example one-shot or multi-level optimization (see, e.g. Nocedal & Wright, 2000; Dadone & Grossman, 2000) in further studies to speed up the optimization procedure.

This work is based on the 2D shallow water equations. In ocean modeling many processes need to be resolved in three dimensions. There are many unstructured three dimensional models (FEOM, ICOM, T-UGO, etc.); they differ in the spatial and temporal discretization among other features. An intercomparison of those models in realistic settings is needed in order to identify common demerits and stimulate further model improvement. One problem already identified is the open boundary condition. For three dimensional models it is even more difficult to find well-posed conditions. This thesis showed that the open boundary condition and open boundary values are important. They should be focus of future studies.

# Appendix

## Normalized surface harmonics

The normalized surface harmonics are defined in the following way for  $(\lambda, \theta) \in \Omega$  and  $n \in \mathbb{N}_0, m = 0, \dots, n$ ,

$$\begin{aligned} & \sqrt{\frac{4\pi}{\kappa_{nm}}} P_{nm}(\sin \theta) \cos m\lambda \\ & \sqrt{\frac{4\pi}{\kappa_{nm}}} P_{nm}(\sin \theta) \sin m\lambda \end{aligned}$$

and

$$\begin{aligned} \kappa_{nm} &= \frac{2\pi}{2n+1} \frac{(n+m)!}{(n-m)!} \quad \text{for } m \neq 0 \\ \kappa_{n0} &= \frac{4\pi}{2n+1}, \end{aligned}$$

where  $P_{nm}$  are the Legendre functions and  $\bar{P}_{nm} = \sqrt{\frac{4\pi}{\kappa_{nm}}} P_{nm}$  are the normalized Legendre functions.

## Test or basis functions

The test/basis functions for the FE method are formed with the help of shape functions. I define  $s_e$  to be the transformation from an irregular triangle  $e$  to the fundamental triangle with volume  $1/2$ . The shape functions of the fundamental triangle are defined on its nodes  $e_1, e_2, e_3$  by

$$\begin{aligned} \phi_{e_1}(p, q) &= 1 - p - q \\ \phi_{e_2}(p, q) &= p \\ \phi_{e_3}(p, q) &= q \end{aligned}$$

and on its edges  $e_1, e_2, e_3$  by

$$\begin{aligned} \psi_{e_1}(p, q) &= 1 - 2q \\ \psi_{e_2}(p, q) &= 2p + 2q - 1 \\ \psi_{e_3}(p, q) &= 1 - 2p \end{aligned}$$

Each triangle of the mesh is transformed to a fundamental triangle. On this triangle the testfunctions basing on the nodes or edges are defined. For the

continuous test/basis function of  $P_1$  the nodal value is shared by adjoining triangles. On a node  $n$  the basis/test functions is defined by

$$\Phi_n(x, y) = \begin{cases} \phi_{e_k}(s_e(x, y)) & \text{for } (x, y) \in \bar{\Omega}_e, \text{ with } k \in \{1, 2, 3\} \text{ such that } e_k = n \\ 0 & \text{else} \end{cases}$$

I define the non-conforming test/basis functions of  $P_1^{NC}$  with the help of the Heaviside function  $\Theta_e$  defined by

$$\Theta_e(x, y) = \begin{cases} 1 & \text{if } (x, y) \in \Omega_e \\ 0 & \text{if } (x, y) \notin \bar{\Omega}_e \\ 0.5 & \text{if } (x, y) \in \partial\Omega_e \end{cases}$$

On each edge  $i$  there are two (at boundaries only one) triangles  $\Omega_e$  and  $\Omega_f$  sharing the edge. The non-conforming test/basis functions of  $P_1^{NC}$  are, therefore, written as

$$\Psi_i(x, y) = \Theta_e(x, y)\psi_{e_k}(s_e(x, y)) + \Theta_f(x, y)\psi_{f_l}(s_f(x, y)) \text{ with } k, l \text{ s.t. } e_k = f_l = i$$

To simplify the writing I introduce  $\Psi_{ie}$  and  $\Psi_{if}$  i.e. the part of  $\Psi_i$  lying on triangle  $\Omega_e$  resp.  $\Omega_f$ . They are defined as

$$\begin{aligned} \Psi_{ie} &:= \Theta_e(x, y)\psi_{e_k}(s_e(x, y)), \\ \Psi_{if} &:= \Theta_f(x, y)\psi_{f_l}(s_f(x, y)), \end{aligned}$$

and, therefore, I can write

$$\Psi_i(x, y) = \Psi_{ie} + \Psi_{if}.$$

## Advection: Heaviside contribution

In the following Eqn.(2.14) is derived from Eqn.(2.13). The integral is omitted as it does not matter here.

$$\begin{aligned} & \hat{\mathbf{u}}_f \cdot (\mathbf{u}_f \cdot \mathbf{n})[\mathbf{u}] + \frac{1}{2}[\hat{\mathbf{u}}] \cdot (\mathbf{u}_f \cdot \mathbf{n})[\mathbf{u}] + \frac{1}{2}\hat{\mathbf{u}}_f \cdot [\mathbf{u} \cdot \mathbf{n}][\mathbf{u}] + \frac{1}{4}[\hat{\mathbf{u}}] \cdot [\mathbf{u} \cdot \mathbf{n}][\mathbf{u}] \\ &= \hat{\mathbf{u}}_f \cdot \langle \mathbf{u} \cdot \mathbf{n} \rangle[\mathbf{u}] + \frac{1}{2}[\hat{\mathbf{u}}] \cdot (\mathbf{u}_f \cdot \mathbf{n})[\mathbf{u}] + \frac{1}{2}\hat{\mathbf{u}}_e \cdot \langle \mathbf{u} \cdot \mathbf{n} \rangle[\mathbf{u}] \\ & \quad - \frac{1}{2}\hat{\mathbf{u}}_e \cdot \langle \mathbf{u} \cdot \mathbf{n} \rangle[\mathbf{u}] + \frac{1}{4}[\hat{\mathbf{u}}] \cdot [\mathbf{u} \cdot \mathbf{n}][\mathbf{u}] \\ &= \langle \hat{\mathbf{u}} \rangle \cdot \langle \mathbf{u} \cdot \mathbf{n} \rangle[\mathbf{u}] + \frac{1}{2}\hat{\mathbf{u}}_f \cdot \langle \mathbf{u} \cdot \mathbf{n} \rangle[\mathbf{u}] + \frac{1}{2}[\hat{\mathbf{u}}] \cdot (\mathbf{u}_f \cdot \mathbf{n})[\mathbf{u}] \\ & \quad - \frac{1}{2}\hat{\mathbf{u}}_e \cdot \langle \mathbf{u} \cdot \mathbf{n} \rangle[\mathbf{u}] + \frac{1}{4}[\hat{\mathbf{u}}] \cdot [\mathbf{u} \cdot \mathbf{n}][\mathbf{u}] \\ &= \langle \hat{\mathbf{u}} \rangle \cdot \langle \mathbf{u} \cdot \mathbf{n} \rangle[\mathbf{u}] + [\hat{\mathbf{u}}] \cdot \left( -\frac{1}{4}\mathbf{u}_e \cdot \mathbf{n} + \frac{1}{4}\mathbf{u}_f \cdot \mathbf{n} \right) [\mathbf{u}] + \frac{1}{4}[\hat{\mathbf{u}}] \cdot [\mathbf{u} \cdot \mathbf{n}][\mathbf{u}] \\ &= \langle \hat{\mathbf{u}} \rangle \cdot \langle \mathbf{u} \cdot \mathbf{n} \rangle[\mathbf{u}] \end{aligned}$$

## WCE after Lynch & Gray (1979)

The momentum and continuity equations, given in Eqn.(2.2) and Eqn.(2.3), are considered without advection and viscosity and with linear bottom friction, i.e.

$$\frac{\partial H\mathbf{u}}{\partial t} - \mathbf{u}\frac{\partial H}{\partial t} + gH\nabla\eta + Hf\mathbf{k} \times \mathbf{u} + H\tau\mathbf{u} = 0, \quad (\text{I})$$

$$\frac{\partial H}{\partial t} + \nabla \cdot (H\mathbf{u}) = 0, \quad (\text{II})$$

where  $\tau$  denotes the linear bottom friction coefficient and the other variables are defined in Section 2.1. Taking the temporal derivative of Eqn.(II) and substituting its second term with an expression of Eqn.(I) gives

$$\frac{\partial^2 H}{\partial t^2} - \nabla \cdot \left( -\mathbf{u}\frac{\partial H}{\partial t} + gH\nabla\eta + Hf\mathbf{k} \times \mathbf{u} + H\tau\mathbf{u} \right) = 0.$$

Since it holds that  $-\nabla \cdot (H\mathbf{u}\tau) = -\tau\nabla \cdot H\mathbf{u} - H\mathbf{u} \cdot \nabla\tau$  and  $\nabla \cdot (H\mathbf{u})$  can be replaced by an expression from the continuity equation, the equation writes as

$$\frac{\partial^2 H}{\partial t^2} + \tau\frac{\partial H}{\partial t} - \nabla \cdot \left( -\mathbf{u}\frac{\partial H}{\partial t} + gH\nabla\eta + Hf\mathbf{k} \times \mathbf{u} \right) - H\mathbf{u} \cdot \nabla\tau = 0.$$

This is the WCE after Lynch & Gray (1979). The last term cancels, when the bottom friction coefficient is spatially constant.

## GWCE

This approach starts from the following equation with parameter  $\tau_0$ ,

$$\partial\chi/\partial t + \tau_0^{-1}\chi = 0,$$

and replaces  $\chi$  with the left hand side of the continuity equation, i.e.  $\chi = \frac{\partial\eta}{\partial t} + \nabla \cdot ((\eta + H_0)\mathbf{u})$ . This results in

$$\frac{\partial^2\eta}{\partial t^2} + \nabla \cdot \left( \frac{\partial}{\partial t}((\eta + H_0)\mathbf{u}) \right) + \tau_0^{-1} \left( \frac{\partial\eta}{\partial t} + \nabla \cdot (\eta + H_0)\mathbf{u} \right) = 0.$$

Further, the temporal derivative of the second term is expressed by the momentum equation (Eqn.(I)) and finally gives the GWCE

$$\frac{\partial^2\eta}{\partial t^2} - \nabla \cdot \left( -\mathbf{u}\frac{\partial H}{\partial t} + gH\nabla\eta + Hf\mathbf{k} \times \mathbf{u} + H\tau\mathbf{u} \right) + \tau_0^{-1} \left( \frac{\partial\eta}{\partial t} + \nabla \cdot (\eta + H_0)\mathbf{u} \right) = 0.$$



# Bibliography

- Andersen, O. B. 1999. Shallow water tides in the northwest European shelf region from TOPEX/POSEIDON altimetry. *Journal of Geophysical Research*, **104**(C4), 7729–7741.
- Andersen, O. B. 2008. *Personal communication*.
- Anderson, J. D. 1995. *Computational Fluid Dynamics: The Basics with Applications*. McGraw-Hill.
- Androsov, A. A., Klevanny, K. A., Salusti, E. S., Voltzinger, N. E. 1995. Open boundary conditions for horizontal 2-D curvilinear-grid long-wave dynamics of a strait. *Advances in Water Resources*, **18**, 267–276.
- Aster, R. C., Borchers, B., Thurber, C. H. 2005. *Parameter Estimation and Inverse Problems*. International Geophysics Series, vol. 90. Elsevier Academic Press.
- Babuska, I. 1971. Error-Bounds for Finite Element Method. *Numerische Mathematik*, **16**, 322–333.
- Backhaus, J. O. 1979. First results of a three-dimensional model on the dynamics in the German Bight. *In: Nihoul, J. C. J. (ed), Proceedings of the 10th International Liège Colloquium on Ocean Hydrodynamics*. Elsevier Oceanography Series, vol. 25. Elsevier, Amsterdam.
- Backhaus, J. O. 1985. A three dimensional model for the simulation of shelf sea dynamics. *Ocean Dynamics*, **38**(4), 165–187.
- Bennett, A. F. 1992. *Inverse Methods in Physical Oceanography*. Cambridge University Press.
- Bennett, A. F., McIntosh, P. C. 1982. Open Ocean Modeling as an Inverse Problem: Tidal Theory. *Journal of Physical Oceanography*, **12**(10), 1004–1018.
- Bennett, A. F., McIntosh, P. C. 1984. Open Ocean Modeling as an Inverse Problem:  $M_2$  Tides in Bass Strait. *Journal of Physical Oceanography*, **14**(3), 601–614.

- Bernard, P.-E. 2008. *Discontinuous Galerkin methods for geophysical flow modeling*. Ph.D. thesis, Université Catholique de Louvain, Faculté des Sciences Appliquées, Unité de Mécanique Appliquée.
- Blain, C. A., Rogers, W. E. 1998. *Coastal Tide Prediction Using the ADCIRC-2DDI Hydrodynamic Finite Element Model: Model Validation and Sensitivity Analyses in the Southern North Sea/English Channel*. Tech. rept. Naval Research Laboratory, Stennis Space Center.
- Blanz, T., Emeis, K.-C., Siegel, H. 2005. Controls on alkenone unsaturation ratios along salinity gradient between the open ocean and the Baltic Sea. *Geochimica et Cosmochimica Acta*, **69**(14), 3589–3600.
- Blayo, E., Debreu, L. 2005. Revisiting open boundary conditions from the point of view of characteristic variables. *Ocean Modelling*, **9**, 231–252.
- Braess, D. 2007. *Finite Elemente: Theorie, schnelle Löser und Anwendungen in der Elastizitätstheorie*. Springer, Berlin.
- Brebbia, C. A., Partridge, P. W. 1976. Finite element simulation of water circulation in the North Sea. *Applied Mathematical Modelling*, **1**, 101–107.
- Brettschneider, G. 1967a. Anwendungen des hydrodynamisch-numerischen Verfahrens zur Ermittlung der M2-Mittschwingungszeit der Nordsee. *Mitteilungen des Instituts für Meereskunde der Universität Hamburg*, **7**.
- Brettschneider, G. 1967b. Modelluntersuchungen der Gezeiten der Nordsee unter Anwendung des hydrodynamisch-numerischen Verfahrens. *Mitteilungen des Instituts für Meereskunde der Universität Hamburg*, **8**.
- Brezzi, F. 1974. On the existence, uniqueness, and approximation of saddle-point problems arising from Lagrange multipliers. *Revue française, d'automatique informatique, et recherche opérationnelle: Analyse numérique*, **8**, 129–151.
- Bronstein, I. N., Semendjajew, K. A., Musiol, G., Mühlig, H. (eds). 2001. *Taschenbuch der Mathematik*. Verlag Harri Deutsch.
- Broyden, C. G. 1969. A new double-rank minimization algorithm. *Notices of the American Mathematical Society*, **16**, 670.
- Carrère, L., Lyard, F. 2003. Modeling the barotropic response of the global ocean to atmospheric wind and pressure forcing - comparisons with observations. *Geophysical Research Letters*, **30**(6), 1275.

- Casulli, V., Cattani, E. 1994. Stability, Accuracy and Efficiency of Semi-Implicit Method for Three-Dimensional Shallow Water Flow. *Computers & Mathematics with Applications*, **27**(4), 99–112.
- Casulli, V., Walters, R. A. 2000. An unstructured grid, three-dimensional model based on the shallow water equations. *International Journal for Numerical Methods in Fluids*, **32**, 331–348.
- Chassignet, E. P., Verron, J. (eds). 2006. *Ocean Weather Forecasting, An Integrated View of Oceanography*. Springer Netherlands.
- Chen, C., Liu, H., Beardsley, R. C. 2003. An Unstructured Grid, Finite-Volume, Three-Dimensional, Primitive Equations Ocean Model: Application to Coastal Ocean and Estuaries. *Journal of Atmospheric and Oceanic Technology*, **20**, 159–186.
- Cotter, C. J., Ham, D. A., Pain, C. C. 2009. A mixed discontinuous/continuous finite element pair for shallow-water ocean modelling. *Ocean Modelling*, **26**, 86–90.
- Courtier, P., Talagrand, O. 1990. Variational assimilation of meteorological observations with direct and adjoint shallow water equations. *Tellus*, **42A**, 531–549.
- Cushman-Roisin, B. 1994. *Introduction to Geophysical Fluid Dynamics*. Prentice Hall.
- Dadone, A., Grossman, B. 2000. Progressive optimization of inverse fluid dynamic design problems. *Computer & Fluids*, **29**, 1–32.
- Damm, P. E. 1997. Die saisonale Salzgehalts- und Frischwasserverteilung in der Nordsee und ihre Bilanzierung. *In: Berichte aus dem Zentrums für Meeres- und Klimaforschung*. Reihe B: Ozeanographie, no. 28. Zentrum für Meeres- und Klimaforschung des Universität Hamburg, Institut für Meereskunde.
- Danilov, S., Wang, Q., Losch, M., Sidorenko, D., Schröter, J. 2008. Modeling ocean circulation on unstructured meshes: comparison of two horizontal discretizations. *Ocean Dynamics*, **58**, 365–374.
- Das, S. K., Lardner, R. W. 1992. Variational parameter estimation for a two-dimensional numerical tidal model. *International Journal for Numerical Methods in Fluids*, **15**, 313–327.
- Davies, A. M. 1976. A Numerical Model of the North Sea and its Use in Choosing Locations for the Deployment of Off-Shore Tide Gauges in the JONSDAP '76 Oceanographic Experiment. *Deutsche Hydrographische Zeitschrift*, **29-1**, 11–24.

- Davies, A. M. 1986. A Three-Dimensional Model of the Northwest European Continental Shelf, with Application to the  $M_4$  Tide. *Journal of Physical Oceanography*, **16**, 797–813.
- Davies, A. M., Kwong, S.C.M., Flather, R. A. 1997a. Formulation of a variable-function three-dimensional model, with applications to the  $M_2$  and  $M_4$  tide on the North-West European Continental Shelf. *Continental Shelf Research*, **17**(2), 165–204.
- Davies, A. M., Kwong, S. C. M., Flather, R. A. 1997b. A Three-dimensional model of diurnal and semidiurnal tides on the European shelf. *Journal of Geophysical Research*, **102**(C4), 8625–8656.
- Davies, A.M., Furnes, G.K. 1980. Observed and Computed M2 Tidal Currents in the North Sea. *Journal of Physical Oceanography*, **10**(2), 237–257.
- Defant, A. 1961. *Physical oceanography, Volume 2*. Oxford, Pergamon Press.
- Dervieux, A., Vázquez, M., Hascoet, L., Koobus, B. 2005. Optimization loops for shape and error control. *Pages 363–373 of: Uthup, B., Koruthu, S. P., Sharma, R. K., Priyadarshi, P. (eds), Post-SAROD Indo-French Workshop: Recent Trends in Aerospace Design and Optimization*. Tata-McGraw Hill, New Delhi.
- Dick, S., Mittelstaedt, E., Müller-Navarra, S. 1992. *Der Küstennahe Gezeitenstrom in der Deutschen Bucht*. Bundesamt für Seeschifffahrt und Hydrographie, Hamburg.
- Dick, S., Kleine, E., Müller-Navarra, S. 2001. The Operational Circulation Model of BSH (BSHcmod) - Model description and validation. *Berichte des Bundesamtes für Seeschifffahrt und Hydrographie*, **29**.
- Djenidi, S., Ronday, F. 1985 (March). Tidal and residual circulation on the North-European continental shelf. *In: Proceedings "Progress in Belgian Oceanographic Research"*.
- Doodson, A. T. 1921. The harmonic development of the tide-generating potential. *Proceedings of the Royal Society of London. Series A*, **100**(704), 305–329.
- Dupont, F. 2001. *Comparison of numerical methods for modelling ocean circulation in basins with irregular coasts*. Ph.D. thesis, Department of Atmospheric and Oceanic Sciences, Mc Gill University, Montreal.
- Dziewonski, A. M., Anderson, D. L. 1981. Preliminary reference Earth model. *Physics of the Earth and Planetary Interiors*, **25**, 297–356.

- Egbert, G., Bennett, A., Foreman, M. 1994. TOPEX/Poseidon tides estimated using a global inverse model. *Journal of Geophysical Research*, **99**(C12), 24821–24852.
- Egbert, G. D., Erofeeva, S. Y. 2002. Efficient inverse modeling of barotropic ocean tides. *Journal of Atmospheric and Oceanic Technology*, **19**(2), 183–204.
- Elizondo, D., Cappelaere, B., Faure, Ch. 2002. Automatic versus manual model differentiation to compute sensitivities and solve non-linear inverse problems. *Computers & Geosciences*, **28**(3), 309–326.
- Errico, R. M. 1997. What Is an Adjoint Model? *Bulletin of the American Meteorological Society*, **78**(11), 2577–2591.
- Evensen, G., Dee, D. P., Schröter, J. 1998. Parameter estimation in dynamical models. *Pages 373–398 of: Chassignet, E.P., Verron, J. (eds), Ocean Modeling and Parametrization. Series C: Mathematical and Physical Sciences, vol. 516. Kluwer Academic Publishers.*
- Farrell, W. E. 1972. Deformation of the Earth by Surface Loads. *Reviews of Geophysics and Space Physics*, **10**(3), 761–797.
- Fernandes, E. H. L., Dyer, K. R., Moller, O. O., Niencheski, L. F. H. 2002. The Patos Lagoon hydrodynamics during El Nino event (1998). *Continental Shelf Research*, **22**, 1699–1713.
- Flather, R. A. 1976. A Tidal Model of the North-West European Continental Shelf. *Memoires Societe Royale des Sciences de Liege*, **6**(X), 141–164.
- Fletcher, R. 1970. A new approach to variable metric methods. *The Computer Journal*, **13**, 317–322.
- Freeden, W., Gervens, T., Schreiner, M. 1998. *Constructive Approximation on the Sphere With Applications to Geomathematics*. Oxford Science Publication, Clarendon.
- Giering, R. 1999. *Tangent linear and Adjoint Model Compiler, Users manual 1.4*.
- Giering, R., Kaminski, T. 1998. Recipes for Adjoint Code Construction. *ACM Transaction On Mathematical Software*, **24**(4), 437–474.
- Gilbert, J. C., Lemaréchal, C. 1989. Some numerical experiments with variable-storage quasi-Newton algorithms. *Mathematical Programming*, **45**, 407–435.
- Gilbert, J. C., Lemaréchal, C. 2008. *The module M1QN3, Version 3.2.c (December 2008)*. Tech. rept. INRIA.

- Gill, P. E., Murray, W., Wright, M. H. 1981. *Practical Optimization*. Academic Press, Inc., Harcourt Brace Jovanovich.
- Goldfarb, D. 1970. A family of variable metric methods derived by variational means. *Mathematics of Computation*, **24**, 23–26.
- Gray, W. G. 1982. Some Inadequacies of Finite Element Models as Simulators of Two-Dimensional Circulation. *Advances in Water Resources*, **5**, 171–177.
- Gray, W. G. 1989. A Finite Element Study of Tidal Flow Data for the North Sea and English Channel. *Advances in Water Resources*, **12**, 143–154.
- Gray, W. G., Kinnmark, I.P.E. 1983. QUIET: A Reduced Noise Finite Element Model for Tidal Circulation. *Advances in Engineering Software*, **5**(3), 130–136.
- Groten, E. 1984. *Landolt-Börnstein, Numerical Data and Functional Relationships in Science and Technology, New Series*. Group V: Geophysics and Space Research, Volume 2a, Geophysics of the Solid Earth, the Moon and the Planets. Springer-Verlag Berlin Heidelberg New York.
- Grotkop, G. 1973. Finite Element Analysis of Long-Period Water Waves. *Computer Methods in Applied Mechanics and Engineering*, **2**, 147–157.
- Gustafsson, B. 1997. Interaction between Baltic Sea and North Sea. *Deutsche Hydrographische Zeitschrift*, **49**(2/3).
- Gustafsson, B., Sundström, A. 1978. Incompletely Parabolic Problems in Fluid Dynamics. *SIAM Journal on Applied Mathematics*, **35**(2), 343–357.
- Hainbucher, D., Backhaus, J. O., Pohlmann, T. 1986. *Atlas of climatological and actual seasonal circulation patterns in the North Sea and adjacent regions: 1969-1981*. Tech. rept. 86-1. Institut für Meereskunde, Universität Hamburg.
- Hall, P., Davies, A. M. 2005. Comparison of finite difference and element models of internal tides on the Malin-Hebrides shelf. *Ocean Dynamics*, **55**(3-4), 272–293.
- Halpern, L. 1991. Artificial boundary conditions for incompletely parabolic perturbations of hyperbolic systems. *SIAM Journal on Mathematical Analysis*, **22**(5), 1256–1283.
- Ham, D. A. 2006. *On techniques for modelling coastal and ocean flow with unstructured meshes*. Ph.D. thesis, Technische Universiteit Delft.

- Ham, D. A., Kramer, S. C., Stelling, G. S., Pietrzak, J. D. 2007. The symmetry and stability of unstructured mesh C-grid shallow water models under the influence of Coriolis. *Ocean Modelling*, **16**, 47–60.
- Hanert, E., Legat, V., Deleersnijder, E. 2003. A comparison of three finite elements to solve the linear shallow water equations. *Ocean Modelling*, **5**(1), 17–35.
- Hanert, E., Le Roux, D.Y., Legat, V., Deleersnijder, E. 2004. Advection schemes for unstructured grid ocean modelling. *Ocean Modelling*, **7**(1-2), 39–58.
- Hanert, E., Le Roux, D.Y., Legat, V., Deleersnijder, E. 2005. An efficient Eulerian finite element method for the shallow water equations. *Ocean Modelling*, **10**(1-2), 115–136.
- Hanert, E., Walters, R. A., Le Roux, D. Y., Pietrzak, J. D. 2009. A tale of two elements:  $P_1^{NC}$  and  $RT_0$ . *Ocean Modelling*, **28**, 24–33.
- Hansen, W. 1952. Gezeiten und Gezeitenströme der halbtägigen Hauptmond tide M2 in der Nordsee. *Deutsche hydrographische Zeitschrift Ergänzungsheft*, **1**.
- Hartmann, T., Wenzel, H.-G. 1994. The harmonic development of the Earth tide generating potential due to the direct effect of the planets. *Geophysical Research Letters*, **21**(18), 1991–1993.
- Hartmann, T., Wenzel, H.-G. 1995a. The HW95 tidal potential catalogue. *Geophysical Research Letters*, **22**(24), 3553–3556.
- Hartmann, T., Wenzel, H.-G. 1995b. The HW95 tidal potential catalogue. *Bulletin d'Informations Marées Terrestres*, **123**, 9278–9301.
- Heaps, N. S., Jones, J. E. 1981. Three-dimensional model for tides and surges with vertical eddy viscosity prescribed in two layers - II. Irish Sea with bed friction layer. *Geophysical Journal of the Royal Astronomical Society*, **64**(1), 303–320.
- Heaps, N.S. 1969. A Two-Dimensional Numerical Sea Model. *Philosophical Transactions of the Royal Society of London. Series A, Mathematical and Physical Sciences*, **265**(1160), 93–137.
- Heemink, A. W., Mouthaan, E. E. A., Roest, M. R. T., Vollebregt, E. A. H., Robaczewska, K. B., Verlaan, M. 2002. Inverse 3D shallow water flow modelling of the continental shelf. *Continental Shelf Research*, **22**, 465–484.

- Hervouet, J.-M. 2007. *Hydrodynamics of Free Surface Flows*. John Wiley & Sons, Ltd.
- Hervouet, J.-M., Van Haren, L. 1994. *TELEMAC-2d Version 3.0 Principal Note*. Tech. rept. EDF Électricité de France, Département Laboratoire National d'Hydraulique.
- Howarth, M. J., Pugh, D. T. 1983. *Physical oceanography of coastal and shelf seas*. Elsevier oceanography series, Amsterdam. Chap. 4, Observations of tides over the continental shelf of north-west Europe, pages 135–185.
- Hua, B., Thomasset, F. 1984. A noise free finite element scheme for the two layer shallow equations. *Tellus*, **36A**, 157–165.
- Hughes, T. J. R. 2000. *The Finite Element Method: Linear Static and Dynamic Finite Element Analysis*. Dover Publications.
- Kantha, L. H., Clayson, C. A. 2000. *Numerical models of oceans and oceanic processes*. Academic Press, San Diego, California.
- Kinnmark, I. P. E. 1986. *The Shallow Water Wave Equations: Formulation, Analysis and Application*. Springer, Berlin.
- Kinnmark, I. P. E., Gray, W. G. 1984. An implicit wave equation model for the shallow water equations. *Advances in Water Resources*, **7**, 168–171.
- Kinnmark, I. P. E., Gray, W. G. 1985. Stability and Accuracy of Spatial Approximations for Wave Equation Tidal Models. *Journal of Computational Physics*, **60**, 447–466.
- Kleptsova, O., Pietrzak, J. D., Stelling, G. S. 2009. On the accurate and stable reconstruction of tangential velocities in C-grid ocean models. *Ocean Modelling*, **28**(1-3), 118–126.
- Kliem, N., Huess, V., Nielsen, J.W. 2006. Evaluation of a shallow water irregular mesh model for the North Sea - Baltic Sea. *Ocean Modelling*, **15**(1-2), 124–136.
- Kubatko, E. J., Westerink, J. J., Dawson, C. 2006. An unstructured grid morphodynamic model with a discontinuous Galerkin method for bed evolution. *Ocean Modelling*, **15**(1-2), 71 – 89. The Third International Workshop on Unstructured Mesh Numerical Modelling of Coastal, Shelf and Ocean Flows.
- Kubatko, E. J., Westerink, J. J., Dawson, C. 2007. Semi discrete discontinuous Galerkin methods and stage-exceeding-order, strong-stability-preserving Runge-Kutta time discretization. *Journal of Computational Physics*, **222**(2), 832–848.

- Ladyzhenskaya, O. 1969. *The Mathematical Theory of Viscous Incompressible Flow*. Gordon and Breach, New York.
- Lardner, R. W., Al-Rabeh, A. H., Gunay, N. 1993. Optimal Estimation of Parameters for a Two-Dimensional Hydrodynamical Model of the Arabian Gulf. *Journal of Geophysical Research*, **98**(C10), 18,229–18,242.
- Le Dimet, F.-X., Talagrand, O. 1986. Variational algorithms for analysis and assimilation of meteorological observations: theoretical aspects. *Tellus*, **38A**, 97–110.
- Le Roux, D. Y. 2005. Dispersion Relation Analysis of the  $P^{NC} - P^1$  Finite-Element Pair in Shallow-Water Models. *SIAM Journal on Scientific Computing*, **27**(2), 394–411.
- Le Roux, D. Y., Lin, C., Staniforth, A. 1998. Finite elements for shallow-water equation ocean models. *Monthly Weather Review*, **126**(7), 1931–1951.
- Le Roux, D. Y., Rostand, V., Pouliot, B. 2007. Analysis of Numerically Induced Oscillations in 2D Finite-Element Shallow-Water Models Part I: Inertia-Gravity Waves. *SIAM Journal on Scientific Computing*, **29**(1), 331–360.
- Le Roux, D. Y., Hanert, E., Rostand, V., Pouliot, B. 2009. Impact of mass lumping on gravity and Rossby waves in 2D finite-element shallow-water models. *International Journal for Numerical Methods in Fluids*, **59**, 767–790.
- Le Roux, D.Y., Sene, A., Rostand, V., Hanert, E. 2005. On some spurious mode issues in shallow-water models using a linear algebra approach. *Ocean Modelling*, **10**, 83–94.
- Lenhart, H.-J., Pohlmann, T. 1997. The ICES-boxes approach in relation to results of a North Sea circulation model. *Tellus*, **49A**, 139–160.
- Loewe, P. (ed). 2009. *System Nordsee, Zustand 2005 im Kontext langzeitlicher Entwicklung*. Berichte des BSH, vol. 44. Bundesamt für Seeschifffahrt und Hydrographie.
- Losch, M., Adcroft, A., Campin, J. M. 2004. How sensitive are coarse general circulation models to fundamental approximations in the equations of motion? *Journal of Physical Oceanography*, **34**, 306–319.
- Love, A. E. H. 1909. The yielding of the Earth to disturbing forces. *Proceedings of the Royal Society of London, Series A*, **82**, 73–88.
- Lu, X., Zhang, J. 2006. Numerical study on spatially varying bottom friction coefficient of a 2D tidal model with adjoint method. *Continental Shelf Research*, **26**, 1905–1923.

- Luettich, R., Westerink, J. 2004. *Formulation and Numerical Implementation of the 2D/3D ADCIRC Finite Element Model Version 44.XX*. Tech. rept. University of North Carolina at Chapel Hill, University of Notre Dame.
- Luettich, R. A., Westerink, J. J., Scheffner, N. W. 1992. *ADCIRC: An Advanced Three-Dimensional Circulation Model for Shelves, Coasts and Estuaries, Report 1: Theory and Methodology of ADCIRD-2DDI and ADCIRC-3DL*. Technical Report DRP-92-6. U.S. Army Corps of Engineers Waterways Experiment Station, Vicksburg, MS.
- Lyard, F. 2009. *Personal communication*.
- Lyard, F., Lefevre, F., Letellier, T., Francis, O. 2006. Modelling the global ocean tides: modern insights from FES2004. *Ocean Dynamics*, **56**, 394–415.
- Lynch, D. R., Gray, W. G. 1979. A wave equation model for finite element tidal computations. *Computers and Fluids*, **7**(3), 207–228.
- Lynch, D. R., Ip, J. T. C., Naimie, C. E., Werner, F. E. 1996. Comprehensive coastal circulation model with application to the Gulf of Maine. *Continental Shelf Research*, **16**(7), 875–906.
- Lynch, D. R., Holbroke, M. J., Naimie, C. E. 1997. The Maine coastal current: spring climatological circulation. *Continental Shelf Research*, **17**(6), 605–634.
- Maier-Reimer, E. 1977. Residual circulation in the North Sea due to the  $M_2$ -tide and mean annual wind stress. *Deutsche hydrographische Zeitschrift*, **30**, 69–80.
- Marchesiello, P., McWilliams, J.C., Shchepetkin, A. 2001. Open boundary conditions for long-term integration of regional oceanic models. *Ocean Modelling*, **3**(1-2), 1–20.
- Marchuk, G. I., Gordeev, R. G., Rivkind, V. Ya., Kagan, B. A. 1973. A numerical method for the solution of tidal dynamics equations and the results of its application. *Journal of Computational Physics*, **13**(1), 15–34.
- Marotzke, J., Giering, R., Zhang, K. Q., Stammer, D., Hill, C., Lee, T. 1999. Construction of the adjoint MIT ocean general circulation model and application to Atlantic heat transport sensitivity. *Journal of Geophysical Research*, **104**(C12), 29,529–29,547.
- Massey, T. C., Blain, C. A. 2006. In search of a consistent and conservative mass flux for the GWCE. *Computer Methods in Applied Mechanics and Engineering*, **195**, 571–587.

- Meier, H. E. M., Feistel, R., Piechura, J., Arneborg, L., Burchard, H., Fiekas, V., Golenko, N., Kuzmina, N., Mohrholz, V., Nohr, C., Paka, V. T., J.Sellschopp, Stips, A., Zhurbas, V. 2006. Ventilation of the Baltic Sea deep water: A brief review of present knowledge from observations and models. *Oceanologia*, **48**(S), 133–164.
- Mittelstaedt, E., Lange, W., Brockmann, C., Soetje, K. C. 1983. *Die Strömungen in der Deutschen Bucht*. Deutsches Hydrographisches Institut, Hamburg.
- Moritz, H. 1980. *Advanced Physical Geodesy*. Sammlung Wichmann Neue Folge, Band 13. Herbert Wichmann Verlag Karlsruhe.
- Müller, L. 2008. *Sauerstoffdynamik der Nordsee, Untersuchungen mit einem dreidimensionalen Ökosystemmodell*. Berichte des BSH, vol. 43. Bundesamt für Seeschifffahrt und Hydrographie.
- Munk, W., Wunsch, C. 1998. Abyssal recipes II: energetics of tidal and wind mixing. *Deep-Sea Research I*, **45**, 1977–2010.
- Navon, I. M. 1985 (October 15-17). A review of variational and optimization methods in meteorology. *Pages 29–34 of: Sasaki, Y. K. (ed), Proceedings of the International Symposium on Variational Methods in Geosciences, Developments in Geomathematics*, vol. 5. University of Oklahoma, Norman, Oklahoma.
- Newton, I. 1687. *Philosophiae Naturalis Principia Mathematica*. In: Deacon, M. B. (ed), *Oceanography Concepts and History*. Dowden, Hutchinson & Ross, Stroudsboung, PA, 1978.
- Nicolle, A., Karpytchev, M. 2007. Evidence for spatially variable friction from tidal amplification and asymmetry in the Pertuis Breton (France). *Continental Shelf Research*, **27**(18), 2346–2356.
- Nocedal, J. 1980. Updating quasi-Newton matrices with limited storage. *Mathematics of Computation*, **35**, 773–782.
- Nocedal, J., Wright, S. 2000. *Numerical Optimization*. Springer, Series in Operations Research.
- Nordström, J. 1995. The use of characteristic boundary conditions for the Navier-Stokes equations. *Computers & Fluids*, **24**(5), 609–623.
- Oliger, J., Sundström, A. 1978. Theoretical and Practical Aspects of Some Initial Boundary Value Problems in Fluid Dynamics. *SIAM Journal on Applied Mathematics*, **35**(3), 419–446.

- Pandoe, W. W., Edge, B. L. 2003. Three-dimensional hydrodynamic model, study cases for quarter annular and idealized ship channel problems. *Ocean Engineering*, **30**, 1117–1135.
- Parker, B. B. (ed). 1991. *Tidal Hydrodynamics*. John Wiley & Sons, Inc.
- Pedlosky, J. 1987. *Geophysical Fluid Dynamics*. second edn. Springer-Verlag.
- Perot, B. 2000. Conservation Properties of Unstructured Staggered Mesh Schemes. *Journal of Computational Physics*, **159**, 58–89.
- Pham, D. T., Verron, J., Roubaud, M. C. 1998. A singular evolutive extended Kalman filter for data assimilation in oceanography. *Journal of Marine Systems*, **16**, 323–340.
- Pingree, R. D., Griffiths, D. K. 1978. Tidal Fronts on the Shelf Seas Around the British Isles. *Journal of Geophysical Research*, **83**(C9), 4615–4622.
- Plüß, A. 2002. *Das Nordseemodell der BAW zur Simulation der Tide in der Deutschen Bucht*. Bundesanstalt für Wasserbau (BAW), Dienststelle Hamburg.
- Pohlmann, T. 1996. Simulating the heat storage in the North Sea with a three-dimensional circulation model. *Continental Shelf Research*, **16**(2), 195–213.
- Pohlmann, T. 2003. Eine Bewertung der hydro-thermodynamischen Nordseemodellierung. In: *Berichte aus dem Zentrum für Meeres- und Klimaforschung*. Reihe B: Ozeanographie, no. 46. Zentrum für Meeres- und Klimaforschung des Universität Hamburg, Institut für Meereskunde.
- Prandle, D. 1978. Residual flows and elevations in the southern North Sea. *Proceedings of the Royal Society A, Mathematical, Physical & Engineering Science*, **359**, 189–228.
- Proudman, J. 1952. *Dynamical Oceanography*. Dover, New York.
- Ronday, F. C. 1973. Modèle mathématique pour l'étude de la circulation due a la marée en mer du Nord. *Marine Science Branch, Manuscript Report Series*, **29**, 51 pp.
- Ronday, F. C. 1975. *Modèles de circulation hydrodynamique en mer du Nord*. Ph.D. thesis, Liege University.
- Sager, G. 1963. *Atlas der Elemente des Tidenhubs und der Gezeitenströme für die Nordsee, den Kanal und die Irische See*. Deutsche Akademie der Wissenschaften zu Berlin, Institut für Meereskunde, Rostock.

- Sager, G., Sammler, R. 1968. *Atlas der Gezeitenströme für die Nordsee, den Kanal und die Irische See*. Zweite, verbesserte Auflage. Seehydrographischer Dienst der Deutschen Demokratischen Republik, Rostock.
- Savcenko, R., Bosch, W. 2008. *DGFI Report No.81, EOT08a - empirical ocean tide model from multi-mission satellite altimetry*. Tech. rept. Deutsches Geodätisches Forschungsinstitut.
- Schröter, J. 1989. *Ocean Circulation Models: Combining Data and Dynamics*. Kluwer Academic Publishers. Chap. Driving of non-linear time dependent ocean models by observations of transient tracer - a problem of constrained optimization, pages 257–285.
- Schröter, J., Seiler, U., Wenzel, M. 1993. Variational Assimilation of Geosat Data into an Eddy-resolving Model of the Gulf Stream Extension Area. *Journal of Physical Oceanography*, **23**, 925–953.
- Schwiderski, E. W. 1980. On Charting Global Ocean Tides. *Reviews of Geophysics and Space Physics*, **18**(1), 243–268.
- Schwiderski, E. W. 1984. Combined hydrodynamical and empirical modeling of ocean tides. *Marine Geophysical Researches*, **7**, 215–229.
- Shanno, D. F. 1970. Conditioning of quasi-Newton methods for function minimization. *Mathematics of Computation*, **24**, 145–160.
- Shchepetkin, A. F., McWilliams, J. C. 2005. The Regional Oceanic Modeling System (ROMS): a Split-Explicit, Free-Surface, Topography-Following-Coordinate Oceanic Model. *Ocean Modelling*, **9**, 347–404.
- Shulman, I., Lewis, J. K., Blumberg, A. F., Kim, B. N. 1998. Optimized Boundary Conditions and Data Assimilation with Application to the  $M_2$  Tide in the Yellow Sea. *Journal of Atmospheric and Oceanic Technology*, **15**(4), 1066–1071.
- Sidorenko, D. 2004. *The North Atlantic circulation derived from inverse models*. Ph.D. thesis, Fachbereich Physik, Universität Bremen.
- Simon, J. L., Bretagnon, P., Chapront, J., Chapront-Touzé, M., Francou, G., Laskar, J. 1994. Numerical expression for precession formulae and mean elements for the Moon and the planets. *Astronomy & Astrophysics*, **282**, 663–683.
- Sinha, B., Pingree, R. D. 1997. The principal lunar semidiurnal tide and its harmonics: baseline solutions for  $M_2$  and  $M_4$  constituents on the North-West European Continental Shelf. *Continental Shelf Research*, **17**(11), 1321–1365.

- Smirnow, W. I. 1982. *Lehrgang der höheren Mathematik, Teil III,2*. Hochschulbücher für Mathematik, Band 4. VEB Deutscher Verlag der Wissenschaften. Page 425 pp.
- Strikwerda, J. C. 1977. Initial boundary value problems for incompletely parabolic systems. *Communications on Pure and Applied Mathematics*, **30**(6), 797–822.
- Taguchi, E. 2004. Inverse Modellierung nichtlinearer Flachwassergezeiten und ihre Anwendungen auf ein Randmeer. In: *Berichte aus dem Zentrum für Meeres- und Klimaforschung*. Reihe B: Ozeanographie, no. 47. Zentrum für Meeres- und Klimaforschung des Universität Hamburg, Institut für Meereskunde.
- Taylor, G. I. 1918. Tidal Friction in the Irish Sea. *Philosophical Transactions of the Royal Society of London, Series A*, **220**, 1 pp.
- Ten Brummelhuis, P. G. J., Heemink, A. W. 1993. Identification of shallow sea models. *International Journal for Numerical Methods in Fluids*, **17**, 637–665.
- Torge, W. 2003. *Geodäsie*. Walter de Gruyter, Berlin - New York.
- Tröltzsch, F. 2005. *Optimale Steuerung partieller Differentialgleichungen: Theorie, Verfahren und Anwendungen*. Vieweg+Teubner.
- Tziperman, E., Thacker, W. C. 1989. An optimal-control/adjoint-equations approach to studying the oceanic general circulation. *Journal of Physical Oceanography*, **19**(10), 1471–1485.
- Tziperman, E., Tacher, W. C., Long, R. B. 1992. Oceanic data analysis using a general circulation model, part II: A north Atlantic model. *Journal of Physical Oceanography*, **22**(12), 1458–1485.
- Uncles, R. J., Stephens, J. A. 1989. Distribution of suspended sediment at high water in a macrotidal estuary. *Journal of Geophysical Research*, **94**(C10), 14,395–14,405.
- Verlaan, M., Mouthaan, E. E. A., Kuijper, E. V. L., Philippart, M. E. 1996. *Hydroinformatics'96: Proceedings of the Second International Conference on Hydroinformatics, Zürich, Switzerland, 9-13 September, 1996*. A A Balkema, Rotterdam. Chap. Parameter estimation tools for shallow water flow models, pages 341–348.
- Vogel, C. R. 2002. *Computational Methods for Inverse Problems*. Frontiers in applied mathematics. SIAM.

- Vreugdenhil, C. B. 1994. *Numerical methods for shallow-water flow*. Kluwer Academic Publishers, Dordrecht.
- Wahr, J. M. 1981. Body tides on an elliptical, rotating, elastic and oceanless earth. *Geophysical Journal of Royal Astronomical Society*, **64**(3), 677–703.
- Walters, R. A. 1987. A Model For Tides and Currents in the English Channel and Southern North Sea. *Advances in Water Resources*, **10**, 138–148.
- Walters, R. A., Carey, G. F. 1983. Analysis of spurious oscillation modes for the shallow water and Navies-Stokes equations. *Computers & Fluids*, **11**(1), 51–68.
- Walters, R. A., Casulli, V. 1998. A robust, finite element model for hydrostatic surface water flows. *Communications in Numerical Methods in Engineering*, **14**(10), 931–940.
- Walters, R. A., Hanert, E., Pietrzak, J., Le Roux, D. Y. 2009. Comparison of unstructured, staggered grid methods for the shallow water equations. *Ocean Modelling*, **28**(1-3), 106–117.
- Wang, Q., Danilov, S., Schröter, J. 2008a. Comparison of overflow simulations on different vertical grids using the Finite Element Ocean circulation Model. *Ocean Modelling*, **20**(4), 313–335.
- Wang, Q., Danilov, S., Schröter, J. 2008b. Finite element ocean circulation model based on triangular prismatic elements, with application in studying the effects of topography representation. *Journal of Geophysical Research*, **113**, C05015.
- Wenzel, H.-G. 1997. Tide-Generating Potential for the Earth. *In*: Wilhelm, H., Zürn, W., Wenzel, H.-G. (eds), *Tidal Phenomena*. Lecture notes in earth sciences, vol. 66. Springer-Verlag Berlin Heidelberg New York.
- Werner, F. E. 1995. A field test case for tidally forced flows: A review of the Tidal Flow Forum. *In*: Lynch, D. R., Davies, A. M. (eds), *Quantitative Skill Assessment for Coastal Ocean Models*. Coastal Estuarine Series AGU.
- Werner, F. E., Lynch, D. R. 1989. Harmonic Structure of English Channel/Southern Bight Tides from a Wave Equation Simulation. *Advances in Water Resources*, **12**, 121–142.
- Westerink, J. J., Gray, W. G. 1991. Progress in Surface Water Modeling. *Reviews of Geophysics*, **29**, 210–217.

- Westerink, J. J., Luettich, R. A., Blain, C. A., Scheffner, N. W. 1992. *ADCIRC: an advanced three-dimensional circulation model for shelves, coast and estuaries, Report 2: user's manual for ADCIRC-2DDI*. Contractors Report to the US Army Corps of Engineers DPR-92. Washington, DC.
- Yanagi, T., Yoshikawa, K. 1983. Generation Mechanisms of Tidal Residual Circulation. *Journal of Oceanographical Society of Japan*, **39**, 156–166.
- Yang, Z., Hamrick, J. H. 2005. Optimal control of salinity boundary condition in a tidal model using a variational inverse method. *Estuarine, Coastal and Shelf Science*, **62**, 13–24.
- Zahel, W. 1978. The Influence of Solid Earth Deformations on Semidiurnal and Diurnal Oceanic Tides. *Pages 98–124 of: Brosche, P., Sündermann, J. (eds), Tidal Friction and the Earth's Rotation*. Springer-Verlag Berlin Heidelberg New York.
- Zahel, W. 1995. Assimilating ocean tide determined data into global tidal models. *Journal of Marine Systems*, **6**, 3–13.
- Zhang, A., Wei, E., Parker, B. B. 2003. Optimal estimation of tidal open boundary conditions using predicted tides and adjoint data assimilation technique. *Continental Shelf Research*, **23**, 1055–1070.

# Acknowledgements

First of all I would like to thank my supervisors and the members of my PhD committee, who provided me with ideas and constructive advises for this thesis: Prof. Dr. Dirk Olbers, Prof. Dr. Jörn Behrens, Dr. Alexey Androsov, Dr. Sergey Danilov and Dr. Jens Schröter.

Theory and coding of the unstructured grid models would not have been possible without Dr. Sergey Danilov, who spend some considerable time with me in explaining and correcting. Dr. Alexey Androsov introduced me into tidal modeling, which was indispensable for the success of the thesis. I would like thank them for the collaborative work we did for writing my first paper together.

Next to them also many colleagues, especially Sven Harig and Dmitry Sidorenko, supported me by answering questions or providing me with useful source code templates and meshes. Special thanks also goes to Martin Losch for his help with TAMC and the adjoint model. It was always nice to hear his honest opinion.

I also want to thank the proof readers of my thesis and many friends, colleges, collaborators and relatives for ideas and support in many ways.

Further, I am grateful for the PhD position, which was financed by the Alfred-Wegener-Institute. Special thanks goes to the computational service for the technical support and to the organizers and participants of the expedition ANTXXIV/2 for the great time on board of Polarstern.

Many friends accompanied me during the last three years in Bremerhaven and I am thankful for gaining personal growth in many aspects of life.